University of Dayton

“ELLIPTICAL VORTEX BEAMS THROUGH TURBULENT ATMOSPHERE”

Dual Program

Master of Science (Optics) from **Centro de Investigaciones en Óptica, A.C. (CIO)**

Master of Science in Electro-Optics from **University of Dayton (UD)**

Thesis presented by:

Emmanuel Narváez Castañeda

Advisor at CIO: Dr. Roberto Ramírez Alarcón

Advisor at UD: Dr. Qiwen Zhan

January 2021

León · Guanajuato · México

Abstract

In this work, simulations of propagation of helical Ince-Gauss beams, elliptical solutions of the paraxial wave equation that carry orbital angular momentum, were performed in order to investigate how the nature of these modes affect their performance as information carrying beams in free space optical communication systems. Special attention was given to the effects that the order p, degree m and ellipticity ε parameters, and their evolution, have on the robustness of the beam. We find that for a given mode, the chose of basis in which it is projected (ellipticity value) does not strongly affect the light spatial mode performance as information carrier. However, for a chosen helical Ince-Gauss mode, it is rather more strongly affected by the combination of p and m and their difference $p - m$. These results were obtained by varying propagation parameters such as the refractive index structure parameter C_n^2 or propagation distances and using different beam structure parameters as the mentioned p, m and ε. From the simulations, both intensity and phase transverse profiles were calculated as well as propagation measurements such as the fidelity of the modes, and specially defined scintillation index and strehl ratio. Additionally, the generation of these vortex beams using spatial light modulators was demonstrated, showing the evolution of the transverse intensity profile of the modes with the ellipticity ε parameter. From this, a detection scheme of these modes is proposed using their near-field intensity profile.

Acknowledgments

I would like to express my gratitude to my advisor at CIO, Roberto Ramírez Alarcón, for allowing me to be part of his research group and for the help and confidence he gave me, related and unrelated to this work. Also to my advisor at UD, Qiwen Zhan for receiving me in his group, always being patient and open minded, but still guiding and pushing me to do the best work possible. I would also like to acknowledge Dr. William Plick and Dr. Imad Agha, as well as M.S César Guerra with who the development of this work was done, always giving meaningful insights and perspectives as well as their support. I am thankful to M.S Zeferino Ibarra, M.S. Carlos Sevilla and Dr. Sichao Zhou for their help with important details regarding experimental and simulation procedures.

I am very grateful to CONACYT for granting me a scholarship during my Master studies, along with an additional scholarship for my studies abroad. Moreover their additional support given to CIO for the realization of: Dual Master and Doctorate Programs between University of Dayton and Centro de Investigaciones en Optica, A.C (CIO).

Finally, thanks a lot to the faculties at both institutions and the people I met along the way. Thanks to my family and friends, who were always supporting me and making me feel at home no matter the distance.

Contents

List of Figures

List of Tables

Chapter 1

Introduction

1.1 Motivation

In recent years, optical communications have had great impact in our everyday lives, steadily replacing electronic communication systems, due mainly to their bigger capacity of information carrying. Today's state of the art of optical communications consists mainly of fiber optics based systems. While fiber optics based systems are very mature in development, they represent a really high cost if they are to be considered to fully replace legacy wire communication networks. This is why they are not, in some cases, a viable solution for last mile connectivity or for the building of networks in really remote places [1]. Especially for these reasons and among others, the possibility to use different basis like polarization and optical angular momentum of light to encode information that is resistant to eavesdropping, free space optical communications have gained special attention in the last couple of years [2–6].

Propagation of laser beams through the atmosphere has important applications not only in communications systems, but also in fields such as Laser Radar (LADAR) technologies [7], Light Detection and Ranging (LIDAR) [8], remote sensing [9], imaging [10], etc. This is a reason why the characterization of the effects of atmospheric turbulence in beam propagation is of big importance for their implementation and optimization in these kind of systems.

Plenty of studies have been made on propagation of laser beams through the atmosphere, focusing mainly on the properties of fundamental Gaussian beams, as they are the most common kind of transverse beam profiles for these applications. However, in recent years other kinds of modified Gaussian beams have been studied, as it has been found that initial beam properties such as shape, phase, size, coherence, etc. strongly affect the performance of these beams [11]. Because of this, one of the hot topics regarding selection and optimization of free space propagation of beams resides on the so-called structured light beams, that are a

result of the manipulation of the spatial degree of freedom of light, i.e., spatial modes of light. Of special interest are structured light beams that carry orbital angular momentum [3,12,13], which began to be broadly studied following the work by Allen et al. [14].

The orbital angular momentum is an intrinsic property of light that resides in a theoretically infinite-dimension space, which translates to an infinite-dimension basis of orthogonal modes, each with the capacity of being an independent channel of information. Comparing this to the capacity of another usually used degree of freedom such as polarization, which resides in an only 2-dimensional space, the usage of orbital angular momentum as information carrier results in a massive advantage due the raw number of communication channels [15]. The mathematical treatment of beams carrying OAM, also known as optical vortexes, has great resemblance to the physics lying in vortexes in fluids as well as giving a connection between macroscopic optics and quantum effects [16, 17]. Thus, the importance of these OAM carrying beams not only resides in the realm of optical communications, as they are used in a broad field of applications and studies such as those regarding: optical tweezers, imaging and microscopy, biomedicine, metrology, astronomy, fluids mechanics [18–24] and even in tests and applications of quantum mechanics, such as quantum entanglement and high dimensional quantum key distribution [25, 26].

While the use of optical vortex beams for free space applications has been studied in free space quantum key distribution and satellite communications systems [27, 28], most of the work has been done using Laguerre-Gaussian beam profiles, natural solutions of the paraxial wave equation in cylindrical coordinates that carry orbital angular momentum. However, limited study has been done using a more general beam profile family of modes that also contains orbital angular momentum: The Ince-Gaussian modes, elliptical solutions of the paraxial wave equation that have an additional degree of freedom in their ellipticity parameter [29]. This characteristic makes them as potential candidates for usage in applications involving optical vortex beams, particularly those regarding free space propagation.

In this thesis, we investigate properties of these Ince-Gaussian beam profile by presenting a procedure on how these modes can be created and then simulating their propagation through atmospheric turbulence. A quantitative and qualitative analysis on the performance and behavior of these beams is made with special attention to their usage in free space communication systems.

1.2 Objectives

The main objective of this thesis is to study, in a theoretical way through mathematical simulations, how different transverse beam profiles behave and change while propagating through turbulent atmosphere. In particular, how a family of solutions of the Paraxial Wave Equation, the Helical Ince-Gauss modes, is affected

by these turbulence effects. These modes display the meaningful trait of carrying orbital angular momentum, which makes them candidate for carrying big quantities of information in optical communications systems with the advantage of having an additional degree of freedom compared to other orbital angular momentum modes: the ellipticity. Special attention is given on how the order, degree and ellipticity parameters of these beams influence the way and degree in which their transverse profiles are modified, in order to obtain general guidelines on which kind of transverse beam profiles exhibit better behavior through atmosphere, and thus, are more suited for their eventual use in free space optical communication systems.

As such, in this work several aspect regarding Ince-Gauss modes are touched upon, such as their mathematical descriptions, the processes in which they can be generated, and of particular importance, their performance while propagating through atmospheric turbulence.

1.3 Thesis structure

The content of this thesis will be distributed in four main chapters besides the introduction one: In the first of these chapters, a theoretical background necessary to understand the different procedures and their respective results carried out in this text is given. Several topics are explored, such as the different solutions of the paraxial wave equations, how these can be used to build light modes with a certain topological charge, and thus orbital angular momentum and finally how the propagation of these beams through atmosphere can be modeled. In the second chapter, a description and demonstration on how this kind of orbital angular momentum carrying modes can be created using a spatial light modulators is presented. In the third chapter, several simulations of orbital angular momentum carrying modes propagated through atmosphere are detailed, by varying some parameters of the light modes and the atmospheric turbulence model. Finally, a conclusion on the overall results of the work is given and the perspective of the project and possible future research work is revised.

Chapter 2

Theoretical framework

In this chapter, the different considerations to take into account for the origin, generation and propagation of Laguerre, Hermite and Ince-Gauss modes are presented. First, the mathematical expressions for these modes are constructed from the Maxwell equations and the nature of these modes as ortho-normal families of solutions of the paraxial wave equation is discussed. Then, helical beams, superpositions of these modes that carry Orbital Angular Momentum are presented and discussed upon. Finally, the different considerations for models of propagation of light beams through the atmosphere are discussed.

2.1 Maxwell Equations and the paraxial wave equation

The description of classical electromagnetic phenomena is enclosed in Maxwell's equations, which for no free charges or currents in SI units and in their differential form are given by [30]:

$$\vec{\nabla} \times \vec{E} = -\frac{\partial}{\partial t}(\mu \vec{H}), \tag{2.1}$$

$$\vec{\nabla} \times \vec{H} = \frac{\partial}{\partial t}(\varepsilon \vec{E}), \tag{2.2}$$

$$\vec{\nabla} \cdot \varepsilon \vec{E} = 0, \tag{2.3}$$

$$\vec{\nabla} \cdot \mu \vec{H} = 0, \tag{2.4}$$

where $\vec{E}$ and $\vec{H}$ represent the electric and magnetic fields, and ε and μ are the electrical permittivity and magnetical permeability of a medium. Through some mathematical manipulations of these equations, a wave equation for the electric field can be derived:

$$\nabla^2 \vec{E} - \mu\varepsilon \frac{\partial}{\partial t^2} \vec{E} = 0, \tag{2.5}$$

were the term $\frac{1}{\sqrt{\mu\varepsilon}}$ gives the speed of the electromagnetic wave. An analogous expression for the wave equation of the magnetic field with the same wave speed can be obtained as well.

The permittivity and permeability, have the information of the propagation medium and are related to the electric and magnetic susceptibilities of said medium (χ_e and χ_m) as:

$$\varepsilon = \varepsilon_0\varepsilon_r = \varepsilon(1+\chi_e), \tag{2.6}$$

$$\mu = \mu_0\mu_r = \mu(1+\chi_m), \tag{2.7}$$

with ε_0 and μ_0 the permittivity and permeability of vacuum, while ε_r and μ_r correspond to the relative permittivity and permeability respectively. Both susceptibilities are in general, spatial and frequency dependent.

From the aforementioned quantities, a parameter of the medium called the *refractive index* can be defined, for a paramagnetic medium ($\mu_r = 1$):

$$n = \sqrt{\varepsilon_r} = \sqrt{1+\chi_e}. \tag{2.8}$$

Because the speed of the electomagnetic wave is given by $\frac{1}{\sqrt{\varepsilon\mu}}$ and ε is dependent on ε_r, then the speed of the electromagnetic wave is n dependent. If the media is vacuum, ($\varepsilon_r = \mu_r = 1$) the speed of the electromagnetic wave is c, the speed of light and the refractive index is $n = 1$. For higher values of ε_r and μ_r, the speed of the wave reduces while n increases. Thus, the real part of n is a measure of how much slower light travels through a medium with respect to vacuum or how *"dense"* the medium is to light. Both susceptibilities can be complex quantities and thus n is in general a complex quantity.

Assuming that the electric field has only components in one direction, the electric field can be written as:

$$\vec{E} = E_n\vec{e}_n, \tag{2.9}$$

having $\vec{e}_n$ as a unitary direction vector. Assuming that the amplitude of the field can be decomposed into temporal and spatial parts:

$$E_n = T(t)E_r(\vec{r}). \tag{2.10}$$

It is well known that the the temporal dependence of the electric field is of the form:

$$T(t) = e^{i\omega t}, \tag{2.11}$$

with ω the radial frequency, while the spatial dependence of the electric field $E_r(\vec{r})$) gives place to the wave equation in (2.5) is transformed into the *Scalar Helmholtz Equation*:

$$\nabla^2 E_r(\vec{r}) + k^2 E_r(\vec{r}) = 0, \tag{2.12}$$

where k is the wave number, magnitude of the propagation vector $\vec{k}$ and defined as:

$$k = \frac{n\omega}{c}. \tag{2.13}$$

Now assuming that the propagation of the wave is predominantly along the optical axis of the beam, which is chosen to be the z-axis, the following expression holds:

$$E_r(\vec{r}) = \Phi(\vec{r})e^{ikz}, \tag{2.14}$$

and by saying that the amplitude of the electric field $\Phi(\vec{r})$ is a slow-varying function with respect to z, that is to say:

$$\left|\frac{\partial^2\Phi(\vec{r})}{\partial z^2}\right| << k\left|\frac{\partial\Phi(\vec{r})}{\partial z}\right|. \tag{2.15}$$

Equation (2.12) becomes:

$$\nabla_t\Phi(\vec{r}) + 2ik\frac{\partial\Phi(\vec{r})}{\partial z}, \tag{2.16}$$

were ∇_t is the Laplacian for the x and y directions. Equation (2.16) is known as the *Paraxial Helmholtz Equation or Paraxial Wave Equation (**PWE**)* [31].

2.2 Solutions of the paraxial wave equation

The lowest-order solution of the *PWE* is the fundamental Gaussian beam, whose expression is [32]:

$$\Phi_G(\vec{r}) = \frac{w_0}{w(z)}\exp\left[\frac{r^2}{w^2(z)} + i\frac{kr^2}{2R(z)} - i\phi_g(z)\right], \tag{2.17}$$

where r is the radial distance from the center axis of the beam, w_0 corresponds to the beam width at $z = 0$, $w^2(z)$ describes the width of the beam, $R(z)$ is the radius of curvature of the phase front and $\phi_g(z)$ is the Gouy phase shift. The referred z_R quantity is known as the Rayleigh range, which gives the distance z_R at which $w(z) = \sqrt{2}w_0$. The introduced parameters are defined as [32]:

$$w^2(z) = w_0^2\left(1 + \frac{z^2}{z_R^2}\right), \tag{2.18}$$

$$R(z) = z + \frac{z_R^2}{z}, \tag{2.19}$$

$$\phi_g(z) = arctan\left(\frac{z}{z_R}\right), \tag{2.20}$$

$$z_R = \frac{kw_0^2}{2}. \tag{2.21}$$

Even though equation (2.17) is the most straight forward solution to the *PWE*, other very important solutions can be derived if one assumes that the beam profile is the aforementioned gaussian beam solution *modulated* by some other kind of transverse profile, meaning:

$$\Phi(\vec{r}) = A_t(\vec{r_t})[iZ(z)]\Phi_G(\vec{r}), \tag{2.22}$$

where $A_t(\vec{r_t})$ is a function that depends only on the transverse coordinates of the beam contained within the transverse position vector $\vec{r_t}$. The solutions of the *PWE* given by this construction strongly depend on the coordinate system in which it is solved, as when inserting (2.22) into (2.16) the transverse Laplacian operator changes with the coordinate system, giving place to differential equations with solutions that involve recursion polynomials which depend on the coordinate system.

For a polar coordinate system on the transverse plane, the solutions are given by the ***Laguerre-Gaussian* (LG)** modes $LG^{e,o}_{n,l}$ [33]:

$$LG^{e,o}_{n,l}(r,\theta,z) = \left[\frac{4n!}{(1+\delta_{0,l})\pi(n+l)!}\right]^{\frac{1}{2}} \frac{1}{w(z)} \begin{pmatrix}\cos(l\theta)\\ \sin(l\theta)\end{pmatrix} \left[\frac{\sqrt{2}r}{w(z)}\right]^{|l|} L_n^{|l|}\left(\frac{2r^2}{w^2(z)}\right) \exp\left[\frac{r^2}{w^2(z)}\right] \exp\left[i\left(kz + \frac{kr^2}{2R(z)} - (2n+|l|+1)\phi_g(z)\right)\right], \tag{2.23}$$

here r is the radial coordinate, θ the azimuthal coordinate, n and l the radial and azimuthal *numbers* and e, o represents the parity of the mode, either even or odd, choosing the cosine term for even and the sine one for odd parity. L_n^l are the associated Laguerre polynomia [33]. Examples of different LG modes can be seen in Figure 2.1, where examples of odd and even modes are shown. All of these modes have azimuthal symmetry and characteristic concentric-ring shapes, with the number of rings is given by the radial parameter n.

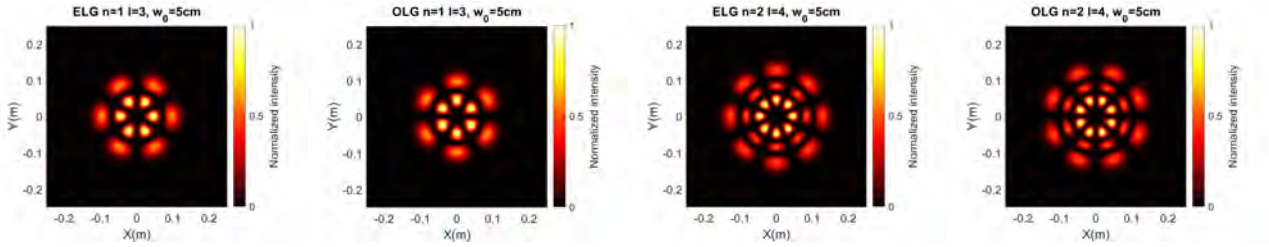

(a) $LG^e_{1,3}$ (b) $LG^o_{1,3}$ (c) $LG^e_{2,4}$ (d) $LG^o_{2,4}$

Figure 2.1: Intensity pattern of different LG modes. Here we consider different values of n and l for even and odd parity. A beam waist $w_0 = 5cm$ was used.

Another solution of the *PWE* can be derived for Cartesian coordinates, yielding the known ***Hermite-Gaussian* (HG)** modes HG_{n_x,n_y} which in normalized form are:

$$HG_{n_x,n_y}(x,y,z) = \left(\frac{1}{2^{n_x,n_y-1}\pi n_x! n_y!}\right)^{1/2} \frac{1}{w(z)} H_{n_x}\left(\frac{\sqrt{2}x}{w(z)}\right) H_{n_y}\left(\frac{\sqrt{2}y}{w(z)}\right) exp\left[\frac{-r^2}{w^2(z)}\right] \exp\left[i\left(kz + \frac{kr^2}{2R(z)} - (n_x+n_y+1)\phi_g(z)\right)\right], \quad (2.24)$$

where x and y are the Cartesian coordinates, $r^2 = x^2 + y^2$ and H_{n_i} is the Hermite polynomial of order n_i [33]. Again, examples of these beams are given in Figure 2.2. As can be seen from the figure, The main difference between the parity is the orientation of the beam, so a $HG^e_{2,3}$ mode would be a $HG^o_{3,2}$.

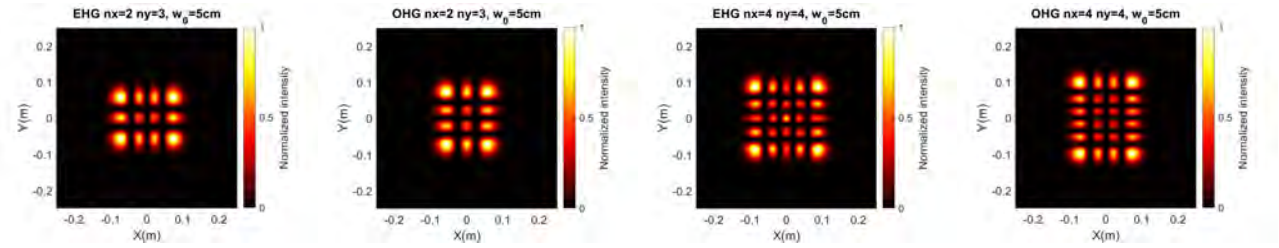

(a) $HG^e_{2,3}$ (b) $HG^o_{2,3}$ (c) $HG^e_{4,4}$ (d) $HG^o_{4,4}$

Figure 2.2: Examples of even and odd HG modes. Odd and even parity are considered, with varying n_x and n_y. The shown modes have a beam waist $w_0 = 5cm$.

Other solutions for the PWE can be derived depending on the coordinate system. For instance, one could propose the solution for the PWE in elliptical coordinates:

$$IG(\vec{r}) = E(\xi)N(\eta)e^{iZ(z)}\Phi_G(\vec{r}). \quad (2.25)$$

Here, $z = z$ and the elliptical coordinates ξ and η are defined as $x = f(z)cosh(\xi)cos(\eta)$ and $y = f(z)sinh(\xi)sin(\eta)$, with $\xi \in [0,\infty)$ and $\eta \in [0,2\pi)$, being ξ and η the radial and angular elliptic variables. $f(z) = f_0 w(z)/w_0$ is the semi focal separation with f_0 the initial semi focal separation. By inserting Equation (2.25) into Equation (2.16) three separate differential equations are obtained:

$$\frac{d^2E}{d\xi^2} - \varepsilon\sinh(2\xi)\frac{dE}{d\xi} - [a - p\varepsilon\cosh(2\xi)]\,E = 0, \quad (2.26)$$

$$\frac{d^2N}{d\eta^2} - \varepsilon\sin(2\eta)\frac{dN}{d\eta} - [a - p\varepsilon\cos(2\eta)]\,N = 0, \quad (2.27)$$

$$-\left(\frac{4z^2 + k^2w^4(0)}{2kw^2(0)}\right)\frac{dZ}{dz}, \quad (2.28)$$

where a and p are separation constants and $\varepsilon = 2f_0^2/w_0^2$ parameter is known as the *ellipticity parameter*.

Equation (2.27) is known as the Ince equation and was studied and solved first by Edward Lunsay Ince [34]. By taking $z = 0$, the solutions of these differential equations are the Ince-Gauss beams [29, 35]:

$$IG^{e,\varepsilon}_{p,m} = \frac{Cw_0}{w(z)} C^m_p(i\xi,\varepsilon) C^m_p(\eta,\varepsilon) \exp\left[\frac{-r^2}{w^2(z)}\right] \exp\left[i\left(kz + \frac{kr^2}{2R(z)} - (p+1)\phi_g(z)\right)\right], \tag{2.29}$$

$$IG^{o,\varepsilon}_{p,m} = \frac{Sw_0}{w(z)} S^m_p(i\xi,\varepsilon) S^m_p(\eta,\varepsilon) \exp\left[\frac{-r^2}{w^2(z)}\right] \exp\left[i\left(kz + \frac{kr^2}{2R(z)} - (p+1)\phi_g(z)\right)\right], \tag{2.30}$$

with e, o referring to *even* or *odd*. The ε parameters adjust the ellipticity of the transverse structure, while the parameters w_0 and f_0 scale the physical size of the mode.

The suffix p corresponds the order and m to the degree of the modes, both having the same parity integer numbers and with the condition $p \geq m \geq 0$ for even numbers and $p \geq m \geq 1$ for odd numbers. C^p_m and S^p_m are the even and odd Ince-Polynomials of order p and degree m and C and S are normalization constants [35]. The Ince-Polynomials can be found by assuming a harmonic expansion [29, 36]:

$$C_{2K,2n\eta}(\eta,\xi) = \sum_{r=0}^{n} A_r(\varepsilon)\cos(2r\eta), \tag{2.31}$$

$$C_{2K+1,2n+1\eta}(\eta,\xi) = \sum_{r=0}^{n} A_r(\varepsilon)\cos((2r+1)\eta), \tag{2.32}$$

$$S_{2K,2n\eta}(\eta,\xi) = \sum_{r=0}^{n} B_r(\varepsilon)\sin(2r\eta), \tag{2.33}$$

$$S_{2K+1,2n+1\eta}(\eta,\xi) = \sum_{r=0}^{n} B_r(\varepsilon)\sin((2r+1)\eta), \tag{2.34}$$

with K having values from 0 to n. By using these expansions and applying them to the differential equations, a series of recurrence relations appear for the weight constants A_r and B_r, which can be expresed as the kernel of the characteristic equation of some matrix, defined by the recurrence relations, having then a taking the role of the eigenvalues of the matrix, whit an associated eigenvector which defines the values of the constants [35].

For the transverse profile of an IG mode, m gives the number of hyperobolic nodal lines, and $(p-m)/2$ is the number of elliptic nodal lines. Higher indices modes have larger physical size as it occurs with LG and HG modes. Examples of IG intensity profiles are given in Figure 2.3. In said figure, even and odd IG modes are shown, with values of ellipticity $\varepsilon = 2$ and $\varepsilon = 3.42$, showing that the value of ε is not necessarily and integer number. It is important to notice that ε heavily affects the shape of the intensity profiles, which have symmetry axis given by this value.

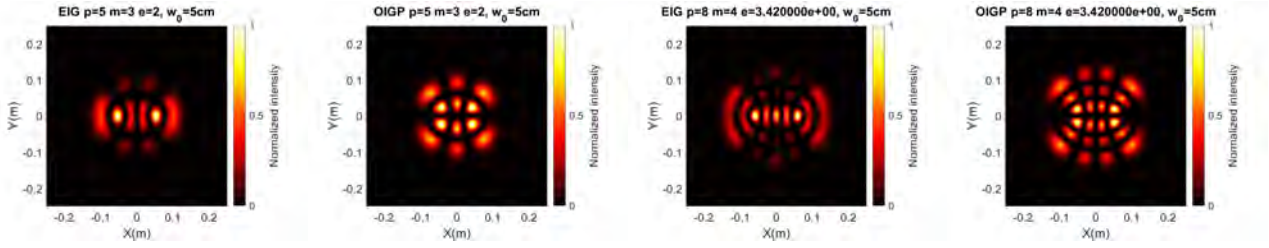

(a) $IG^{e,2}_{5,3}$ (b) $IG^{o,2}_{5,3}$ (c) $IG^{e,3.42}_{8,4}$ (d) $IG^{o,3.42}_{8,4}$

Figure 2.3: Intensity profiles for IG modes. Even and odd intensity profiles are shown for, even and odd parity of p and m, as well as integer and non-integer values of ε. A beam waist $w_0 = 5cm$ was used.

Due to the fact that all of these solutions contain within themselves the mathematical expression of a Gaussian beam, but modulated with a certain function depending on the transverse coordinates, all of these solutions represent a beam of non-Gaussian intensity distribution but with the same wavefronts and angular divergence as a Gaussian beam. As such, regardless of the intensity as can be seen from equations (2.23)-(2.30), the beam width of all modes depends on the factor $w_0/w(z)$ but is shape-invariant, as is the radiature $R(z)$ of the beams. This also means that the ABCD matrix treatment for the propagation of Gaussian Beams applies for the different solutions of the PWE.

Each family of solutions of the PWE constitutes an ortho-normal basis, that is to say that the inner product of the modes (assuming them to be normalized) is of the form:

$$\int_{-\infty}^{\infty}\int_{-\infty}^{\infty} A^{k}_{u}\bar{A^{k'}_{u'}}dS = \delta_{uu'}\delta_{kk'}, \tag{2.35}$$

where A would be a generic mode function, u and k are generic names for the index or indices of the modes, dS is a differential surface element and δ is the Kronecker delta functional. In the particular case of Ince-Gaussian modes, the orthogonality of the modes is written as:

$$\int\int_{-\infty}^{\infty} IG^{\sigma}_{p,m}\bar{IG^{\sigma'}_{p',m'}}dS = \delta\sigma\sigma'\delta_{pp'}\delta_{mm'}. \tag{2.36}$$

All of Laguerre, Hermite and Ince-Gaussian modes create on their own an orthonormal family of solutions of the *PWE*, and thus, each solution on a certain basis can be transformed into another one. In particular, we can look at the Ince-Gaussian modes, as their particular solutions depend on the f_0 parameter, and thus the ellipticity of the used coordinate system. The transition of a IG mode into a LG mode occurs when $\varepsilon = 0$ (circular cylindrical coordinates), while the transition into HG when $\varepsilon = \infty$ (Cartesian coordinates). Similar to how $\varepsilon = 0$ and $\varepsilon = \infty$ define a complete orthogonal basis of modes, **any value of the ellipticity**

parameter describes an individual orthogonal basis [35]. As for the transition of the indices, for LG modes these are related as: $m = l$ and $p = 2n + l$, while for HG these relations depend on the parity of the IG mode: For even ones $n_x = m$ and $n_y = p - m$, while for odd ones $n_x = m - 1$ and $n_y = p - m + 1$. These relations of the indices come from the fact that the Gouy shifts of the beams should match and these are modulated by the indices as can be seen in from (2.23)-(2.30). The transition of orthogonal basis of a mode due to the ellipticity parameter is depicted in Figure 2.4., where the evolution of a $IG^{o,\varepsilon}_{5,3}$ with the value of ε is shown, transforming the original $LG^{o}_{1,3}$ mode into a $HG_{2,3}$ mode for extreme values of ε. As expected, the symmetry of the beam is transformed due to the coordinate system used in each beam, going from azimuthal to rectangular.

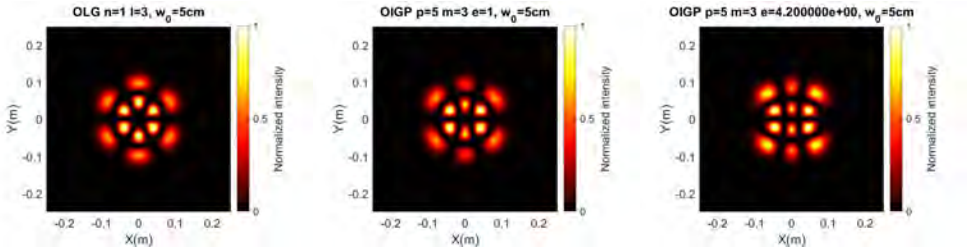

(a) $LG^{o}_{1,3} = IG^{o,0}_{5,3}$ (b) $IG^{o,1}_{5,3}$ (c) $IG^{o,4.2}_{5,3}$

(d) $IG^{o,10}_{5,3}$ (e) $HG^{o}_{2,3} = IG^{o,\infty}_{5,3}$

Figure 2.4: Evolution of a $IG^{o}_{5,3}$ beam, $w_0 = 5cm$, by varying the ellipticity parameter from $\varepsilon = 0$ to $\varepsilon = \infty$.

In general, a transformation matrix method can be used in order to convert IG⇒LG, IG⇒HG or LG⇒HG modes (or vice versa) considering the subset of degenerate modes that in both families have the same Gouy shifts. This is because, in order to construct a structurally stable beam in a family of modes from another basis, they need to remain in the same phase as they propagate. This is a very important result, as it also means that the mode decomposition in any of the transformations is finite.

With this in mind, for any basis one could consider all the modes with a Gouy Phase of $\phi_p(z) = (p+1)\phi_g(z)$ for any basis and note that the number of degenerate modes N_p that form a complete subbasis of orthogonal

modes is given by:

$$N_p = \begin{cases} (p + 2\delta_{\sigma,e}) & \text{for even p,} \\ (p+1)/2 & \text{for odd p.} \end{cases} \tag{2.37}$$

And thus, any IG_p^σ mode with a certain p order and σ parity can be constructed by N_p weighted modes of the other subsets LG_p^σ or HG_p^σ. This transformation of basis can be written as a matrix transformation of the form:

$$\vec{S_p^\sigma} = \left[_{R\Rightarrow S}\mathbf{T}_p^\sigma\right] \vec{R_p^\sigma}, \tag{2.38}$$

where $\vec{R_p^\sigma}$ is the subset of weighted orthogonal modes in a sub-basis to be transformed into the subset $\vec{S_p^\sigma}$ of another sub-basis by the N_pxN_p $\left[_{R\Rightarrow S}\mathbf{T}_p^\sigma\right]$ transformation matrix. These transformation matrices have the property: $\left[_{R\Rightarrow S}\mathbf{T}_p^\sigma\right]^{-1} = \left[_{R\Rightarrow S}\mathbf{T}_p^\sigma\right]^T = \left[_{S\Rightarrow R}\mathbf{T}_p^\sigma\right]$ and each of their columns and rows form a basis of an space of dimensionality N_p.

Finally, the elements of the transformation matrix for a certain p subset of modes from one basis to another can be determined by doing the inner products of each mode of one basis with each of the other one. These are well known expressions [37], however in this work the particular interest is focused on the one that considers IG and LG modes:

$$\int\int_{-\infty}^{\infty} LG_{n,l}^\sigma \bar{IG}_{p,m}^{\sigma'} dS = \delta_{\sigma\sigma'}\delta_{p,2n+l}(-1)^{n+l+(p+m)/2}\sqrt{(1+\delta_{0,l})\Gamma(n+l+1)n!}A_{(l+\delta_{o,\sigma})/2}^\sigma(a_p^m), \tag{2.39}$$

where the term $A_{(l+\delta_{o,\sigma})/2}^\sigma(a_p^m)$ is the $(l+\delta_{o,\sigma})/2$th Fourier coefficient of the Ince polynomial. From this expression, the $D_{l,n}$ coefficients of the LG modes that are an expansion of a certain IG mode are:

$$IG_{p,m}^\sigma(\xi,\eta,\varepsilon) = \sum_{n,l} D_{n,l} LG_{n,l}^\sigma(r,\theta), \tag{2.40}$$

and thus the elements of the transformation matrix can also be determined for the N_p dimensional case.

It is noteworthy to state that these coefficients strongly depend on the ellipticity of the modes. Thus, it is only necessary to know two transformation matrices in order to be able to build a complete transformation scheme. An example of decomposition of an IG mode into the LG basis is shown in Figure 2.2, where a $IG_{5,3}^{e,5}$ is decomposed into the LG basis with a superposition of modes $LG_{2,1}^e$, $LG_{1,3}^e$ and $LG_{0,5}^e$. It is important to notice that the parity of the modes is kept and the sign of the modes can be either positive or negative.

We want to note that, there are four special modes that, due to the relations of these families of modes, have exactly the same transverse distribution independently of the basis chosen to build or describe them.

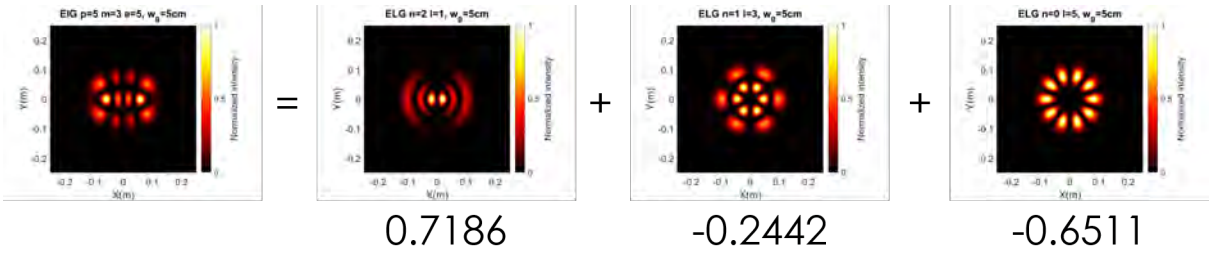

Figure 2.5: Decomposition of $IG^{e,5}_{5,3}$ into the LG basis with a superposition of modes $LG^{e}_{2,1}$, $LG^{e}_{1,3}$ and $LG^{e}_{0,5}$.

Figure 2.2 shows these four fundamental modes which all have phase discontinuities (besides the pure Gaussian mode). The fact that these modes are exactly the same, even when described by different families of modes reveals the underlying symmetries and connections between the exact families of solutions of the PWE. [35].

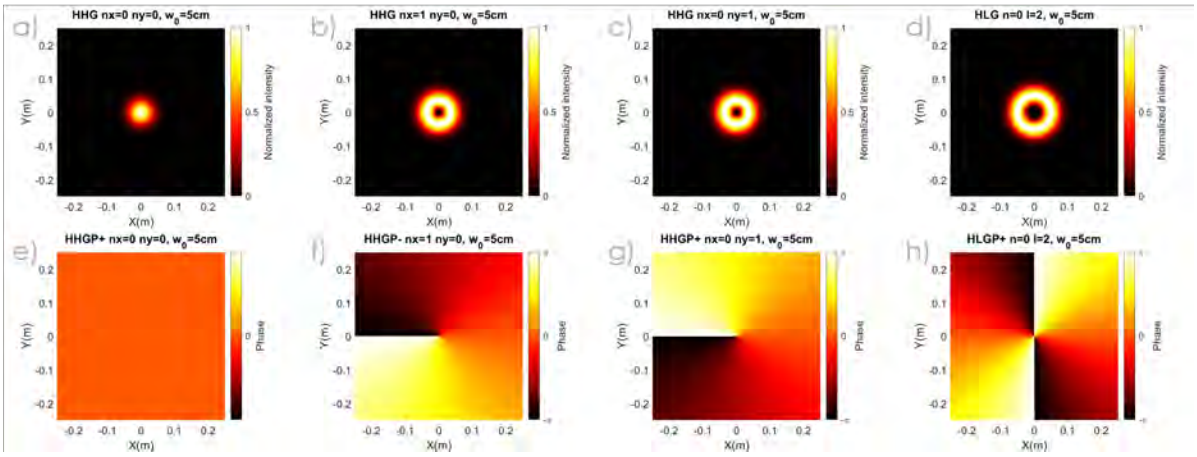

Figure 2.6: Four fundamental modes of the paraxial wave equation, corresponding to from a) to d) $IG_{0,0}$, $IG_{1,1}$, $IG_{1,1}$ and $IG_{2,2}$ for IG modes, $LG_{0,0}$, $LG_{0,1}$, $LG_{0,1}$ and $LG_{0,2}$ for LG modes and $HG_{0,0}$, $HG_{1,0}$, $HG_{0,1}$ and $HG_{1,1}$ for the HG modes. Besides the pure Gaussian mode, all of these modes have phase discontinuities, showcased on the phase profiles for each beam (e) to h)), depicted in the same order as before.

Finally, the different families of solutions of the PWE equations have very interesting properties, since they are exact and orthogonal solutions. They have structurally stable transverse profiles, this means they do not change shape during propagation and they are also transverse eigenmodes of stable resonators [38]. A final and very distinctive feature of them is that, by constructing a certain superposition of these modes, it is possible to obtain helical beams, Orbital Angular Momentum (OAM) carrying beams which will be touched upon in the next subsection.

2.3 Orbital angular momentum of light and helical modes

It is well known that a beam of light carries optical angular momentum. This angular momentum on light, considering a beam traveling in the paraxial regime, can be divided into its spin and orbital components [39].

The spin orbital angular momentum (SAM) is related to the circular polarization of the beam, having a value of $\pm\hbar$ per photon, depending if the beam is right circularly polarized (+ sign) or left circularly polarized (− sign).The manifestation of this orbital momentum has been observed when a SAM-carrying beam is absorbed by a particle, as the particle is made to spin about and axis defined by its own center of mass. [36]

On the other hand, the OAM of a light field comes from its overall transverse phase structure and has a value per photon of $\pm l\hbar$, where l can take any integer value. A particle absorbing a certain quantity of OAM is instead made to rotate about the central axis of the beam itself with the direction of rotation being determined by the sign of OAM. It is also important to notice that, because it is an *external* (from the beam or photon) form of angular momentum, the value of OAM is coordinate system dependent. This behavior is schematically shown in Figure 2.7 [40].

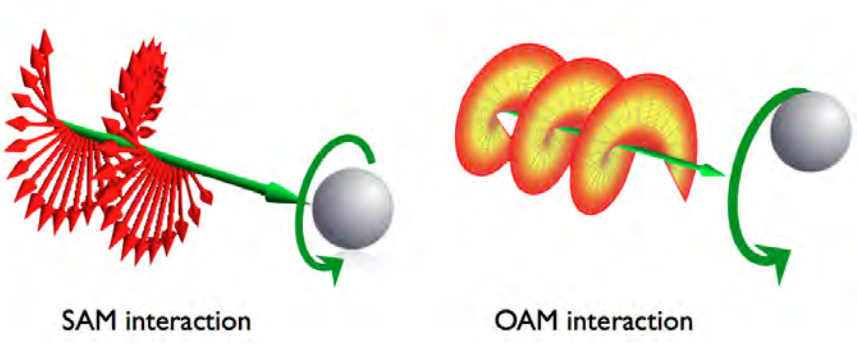

Figure 2.7: Interaction angular momentum of light with matter. SAM is related to the circular polarization of a light beam and makes an object rotate around its own axis, while OAM, related to the phase distribution of the light beam makes the same object rotate about the central axis of the beam.

A particular characteristic of the solutions found in section **2.2** is that certain superpositions of LG, HG and IG modes give place to the called *helical modes*, which at localized parts of their phase profiles have polar phase indeterminations characterized by discontinuities with value $\pm 2\pi l'$, $l' \in Z$, which give place to local zeros of intensity in the beam profile and an OAM value of $l'\hbar$ per photon at said discontinuity. This value is called the *topological charge* of the beam.

The normalized Laguerre Gaussian helical modes of radial and azimuthal numbers n and l are given by:

$$HLG^{\pm}_{n,l}(r,\theta,z) = \frac{1}{\sqrt{2}}\left[LG^{e}_{n,l}(r,\theta,z) \pm iLG^{o}_{n,l}(r,\theta,z)\right]. \tag{2.41}$$

The respective Hermite-Gaussian helical modes are given by [41]:

$$HHG^{\pm}_{p,m}(x,y,z) = \frac{1}{\sqrt{2}}\left[HG_{l,2n}(x,y) \pm iHG_{l-1,2n+1}(x,y)\right], \tag{2.42}$$

with $p = 2n + l$ and $m = l$. In the case of the Helical Ince-Gaussian modes, these are produced through a superposition of modes as:

$$HIG^{\pm,\varepsilon}_{p,m}(\xi,\eta,\varepsilon) = \frac{1}{\sqrt{2}}\left[IG^{e,\varepsilon}_{p,m}(\xi,\eta,\varepsilon) \pm iIG^{o,\varepsilon}_{p,m}(\xi,\eta,\varepsilon)\right]. \tag{2.43}$$

It is important to note that on performing the superposition shown in (2.41), the resulting mathematical expression that can be explicitly derived from (2.23) has a term of the form $e^{-il\theta}$ which in the optical axis of the beam ($r = 0$) is responsible for a phase discontinuity of value $\pm 2\pi l$ as well as of a topological charge of l per photon. In contrast, equations (2.42) and (2.43) yield localized phase discontinuities, at various points of the beam profile, each with a value of $\pm 2\pi$ (or OAM $\hbar$ per photon) *at* the position of the vortices. A comparison of the different helical modes is presented in Figure 2.8.

Figure 2.8 illustrates several special characteristics of OAM carrying beams, for each of the three families of modes that have been described above. In the case of HLG modes, the $2\pi l$ indeterminations in the phase profile are contained exactly at the optical axis of the beam and are given by the azimuthal number l, having $OAM = l\hbar$ per photon, while other non-π ring-shaped phase discontinuities arise from the radial number n. The intensity beam profile is ring-shaped as well, with a zero intensity point at the optical axis. As for the HHG modes, the phase profiles exhibit 2π phase indeterminations as well, but these are distributed all around the beam profile in a rectangular way, with the number phase indeterminations and distribution determined by n_x and n_x. Finally, the intensity shape of HIG modes also shows zero-intensity points (and thus 2π phase indeterminations) at varying points of the beam, whose number and distribution strongly depends on the values of order p and degree m, as well as the ellipticity parameter ε and, as in HLG, the ring-shaped regions are present as well, but bended due to the elliptical symmetry of the beam. For all these helical modes, the positive and negative signs indicate the direction in which all phase vortices are directed: clockwise, or anti-clockwise. All individual vortices for these beams carry OAM $\pm\hbar$ at their position, but the beam as a whole, referred to its optical axis, does not necessarily carry the sum OAM of all its phase discontinuities as will be seen later.

A very important and intriguing property of this kind of helical beam profiles is that they have a well known quantum representation. In particular, the creation operator Laguerre-Gauss-Fock states or Laguerre-Gauss-number states, or states describing individual photons projected in a LG mode can be written as [42]:

$$\hat{a}^{\dagger}_{snl}(k_0) = \int_{-\infty}^{\infty} LG_{n,l}(\vec{q})\hat{a}^{\dagger}_{s}(\vec{q},k_0), \tag{2.44}$$

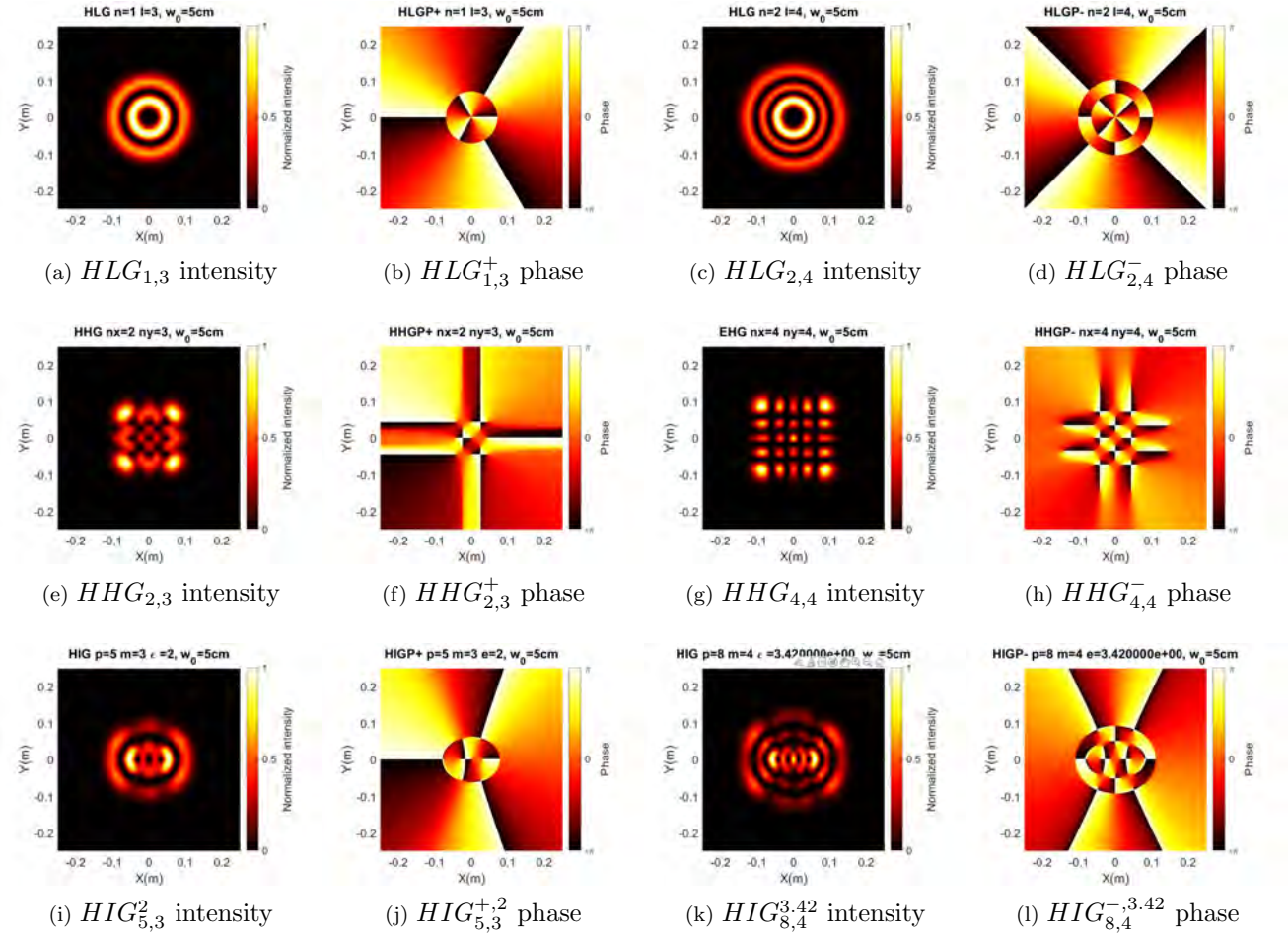

(a) $HLG_{1,3}$ intensity (b) $HLG^{+}_{1,3}$ phase (c) $HLG_{2,4}$ intensity (d) $HLG^{-}_{2,4}$ phase

(e) $HHG_{2,3}$ intensity (f) $HHG^{+}_{2,3}$ phase (g) $HHG_{4,4}$ intensity (h) $HHG^{-}_{4,4}$ phase

(i) $HIG^{2}_{5,3}$ intensity (j) $HIG^{+,2}_{5,3}$ phase (k) $HIG^{3.42}_{8,4}$ intensity (l) $HIG^{-,3.42}_{8,4}$ phase

Figure 2.8: Examples of different OAM carrying beams, which result from the super-positions depicted from equations (2.41)-(2.43) using the modes shown in Figures 2.1-2.3. Each intensity profile has at its right the phase profile of the beam, which in every case shows the phase discontinuities.

with s representing a polarization state either 1 or -1, $\vec{q}$ the transverse momentum vector and $LG_{n,l}(\vec{q})$ the Fourier transform of a LG mode as function of $\vec{q}$. The annihilation operator is similarly defined and obeys the usual commutation relation:

$$[\hat{a}_{snl}(k_0), \hat{a}^{\dagger}_{s'n'l'}(k'_0)] = \delta_{s,s'}\delta_{n,n'}\delta_{l,l'}\delta(k_0 - k'_0). \tag{2.45}$$

Any paraxial photon state can be written as:

$$|\phi\rangle = \sum_{s,n,l} \int_0^{\infty} dk_0 C_{snl}(k_0) \hat{a}^{\dagger}_{snl} |0\rangle , \tag{2.46}$$

where C_{snl} is a normalized weight function of each mode. In particular, the scalar Helical-Laguerre-Gauss Fock states $\left|L^{\pm}_{nl}\right\rangle$ are defined as:

$$\left|\hat{L}^{\pm}_{nl}\right\rangle = \hat{a}^{\dagger}_{nl}(k_0) |0\rangle , \tag{2.47}$$

with $\pm$ being the sign of the topological charge. These modes happen to be eigenvectors of the OAM operator $\hat{L}_z$ defined as:

$$\hat{L}_z = \hbar \sum_{s,n,l} l \int_0^\infty \hat{a}^\dagger_{snl}(k_0)\hat{a}_{snl}(k_0). \tag{2.48}$$

Also, the even and odd LG modes can be written as a sum of helical modes of opposite sign:

$$|L^e_{nl}\rangle = \frac{1}{\sqrt{2}}\left[\left|L^+_{nl}\right\rangle + \left|L^-_{nl}\right\rangle\right], \tag{2.49}$$

$$|L^o_{nl}\rangle = \frac{1}{i\sqrt{2}}\left[\left|L^+_{nl}\right\rangle - \left|L^-_{nl}\right\rangle\right]. \tag{2.50}$$

Considering the above results and also the corresponding advantage of the correspondence principle between the PWE and quantum physics [43], a quantum description of HHG or in particular HIG modes can be made, so that the quantum HIG modes can be written as:

$$\left|I^\pm_{pm}\right\rangle = \frac{1}{\sqrt{2}} = \left[\sum_{n,l} D^e_{nl}\left|L^e_{nl}\right\rangle \pm i \sum_{n',l'} D^e_{n'l'}\left|L^o_{n'l'}\right\rangle\right], \tag{2.51}$$

with the D_{nl} terms being the same as in equation (2.40). An advantage of using this quantum description of the modes is that it is possible to determine the expectation value of $\hat{L}_z$ in non LG modes. While the value of the topological charge for HLG modes is well defined at the optical axis of the beam, in the case of HHG and HIG modes, this is not straight forward, because of the existence of phase discontinuities outside of the optical axis. A solution of the determination of OAM value can be solved by obtaining the expectation value of $\hat{L}_z$ for $\left|I^\pm_{pm}\right\rangle$ states. By doing so, the result yields then [36]:

$$\langle \hat{L}_z \rangle = \pm \sum_{n,l} \hbar l D^e_{n,l} D^o_{n,l}. \tag{2.52}$$

It can be seen that the OAM expectation value of non azimuthally symmetric modes is not necessarily an integer number, and is also not a direct average of the modes comprising the LG decomposition. This is caused by the fact that OAM arises from the gradient of the transverse phase structure of the beam. As the argument (phase of a mode) is not a linear function, an OAM value for HIG modes (HHG modes when $\varepsilon = \infty$) can not be reconstructed from weighted averages of well known HLG modes OAM values. Also, as the decomposition values of the transformation $D^\sigma_{n,l}$ are a function of the ellipticity of the modes, $\langle \hat{L}_z \rangle$ is also a function of ellipticity, as shown in Figure 2.9.

From the graphs it is evident that both the order and the degree of the evolving HIG mode have an important impact on the expectation value of OAM. In the case of modes having the same degree m, at $\varepsilon = 0$ all have the same OAM value, which is $OAM = m\hbar$, these results makes sense as the zero ellipticity mode corresponds to a HLG with azimuthal number $m = l$, which is known to be directly related to the OAM value [44], however as the ellipticity increases, modes with bigger difference $p-m$ tend to increase their initial OAM, contrasting with decrease of this value for lower $p - m$. A bigger difference in $p - m$, at zero ellipticity is related to an increase in the radial mode n of the HLG mode, so it could be said that for bigger

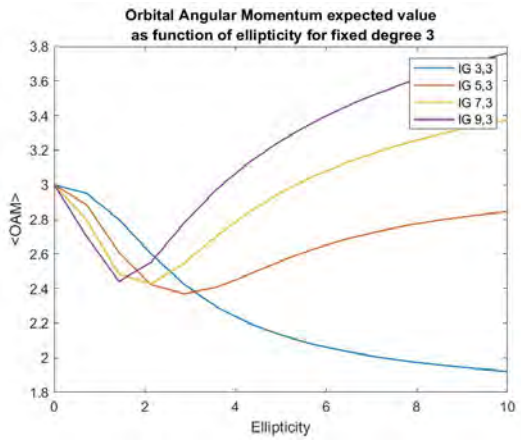

(a) OAM vs ellipticity for fixed m= 3

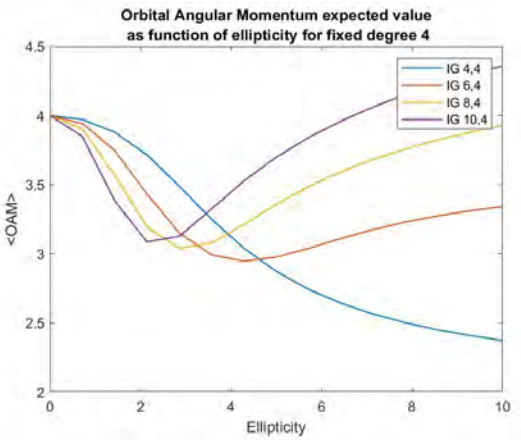

(b) OAM vs ellipticity for fixed m= 3

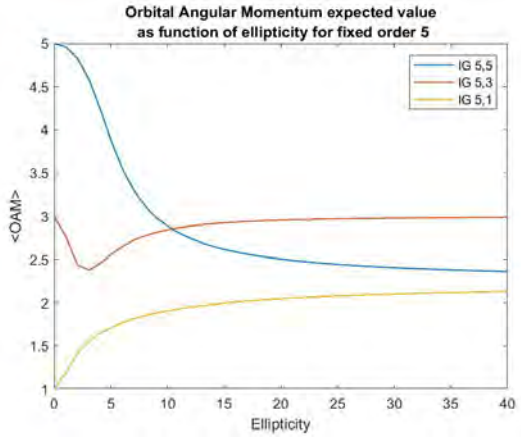

(c) OAM vs ellipticity for fixed p= 5

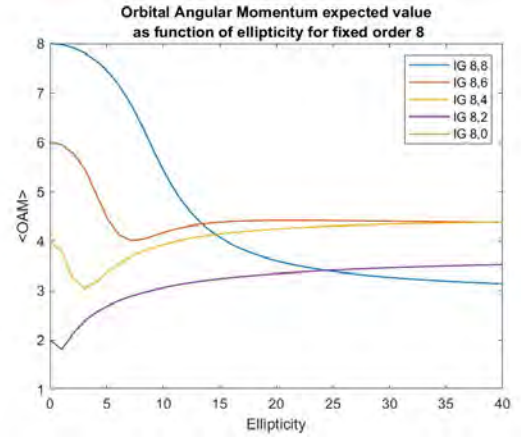

(d) OAM vs ellipticity for fixed p= 8

Figure 2.9: Expectation value of OAM as a function of ellipticity for different modes. a) and b) for a fixed value of m. c) and d) for fixed p. .

initial radial modes of HLG, by varying the ellipticity the total expected value of OAM can be increased. As for the graphs showing OAM for fixed order p, they also show this behaviour related to $p - m$, with the modes having a tinier difference presenting a more abrupt decay of OAM value referring to the initial mode as ellipticity increases. The decay or increase of OAM with the ellipticity however reaches an almost constant value at a certain ε value, as if it is signaling that the mode behaves almost as a HHG mode would do.

A very interesting result that is present in all graphs is that there are intersections between the graphs, meaning that there can be two modes with different values of ellipticity (and thus projected into a different basis) with the same value of OAM. This kind of result can be helpful, for example, in a OAM of light preservation experiment in which one could project the values of the generated photons to a certain value of

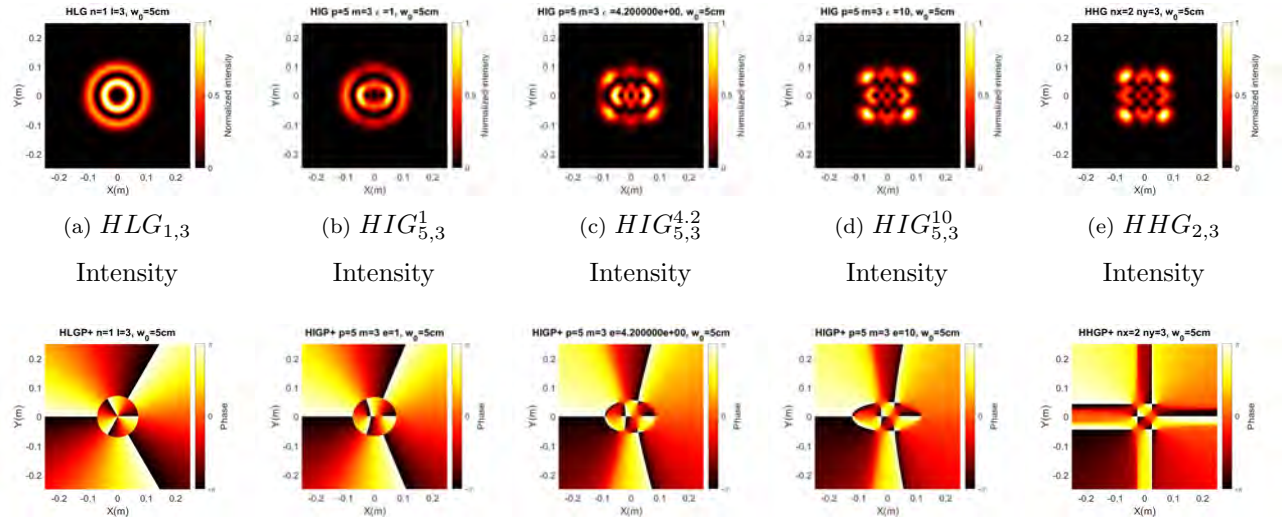

(a) $HLG_{1,3}$ Intensity (b) $HIG^{1}_{5,3}$ Intensity (c) $HIG^{4.2}_{5,3}$ Intensity (d) $HIG^{10}_{5,3}$ Intensity (e) $HHG_{2,3}$ Intensity

(f) $HLG_{1,3}$ Phase (g) $HIG^{1}_{5,3}$ Phase (h) $HIG^{4.2}_{5,3}$ Phase (i) $HIG^{10}_{5,3}$ Phase (j) $HHG_{2,3}$ Phase

Figure 2.10: Evolution of the ellipticity parameter for $HIG_{5,3}$, intensity (a) - e)) and phase (f) - j)) profiles. The chosen values of ellipticity are $\varepsilon = 0$, $\varepsilon = 1$, $\varepsilon = 4.2$, $\varepsilon = 10$ and $\varepsilon = 0$ from left to right for a) - e) and f) - j). The waist of the beams is $w_0 = 5cm$.

OAM, by using different basis. This could as well be used as an extra degree of freedom for communication schemes, in the case of having control of the ellipticity and the OAM value of a beam.

Finally, in order to make clear how the change of the OAM of a certain beam is related to the ellipticity parameter, the ellipticity evolution of the HIG beams presented in Figure 2.9 is shown in Figures 2.10-2.13.

The evolution of the OAM with the ellipticity can be observed from Figures 2.10-2.13. The initial OAM value of the HLG which is contained in the optical axis phase indetermination, breaks down into individual 2π discontinuities along the horizontal axis, all giving place to zero-intensity regions. Depending on the value of the order p, other 2π indeterminations appear outside the propagation axis as ε increases. The number of phase indeterminations, which is maximum for HHG modes, strongly depends on the difference $p - m$, resulting in more zero-intensity points for bigger value of $p - m$. As was seen from 2.9, bigger values of $p - m$ also lead to higher values OAM for increasing ellipticity, that may be attributed to these generated extra phase discontinuities. In the particular case of $p = m$, which translates to $n = 0$ for the HLG modes, the initial $2\pi l$ OAM phase discontinuity is distributed into l $2pi$ ones, outside the optical axis, which explains the abrupt decay in OAM value as ellipticity increases for this particular kind of modes.

The fact that Helical beams carry OAM make them great candidates for optical communications channels, as the OAM degree of freedom is infinitely dimensional in theory. In particular, their use in free space

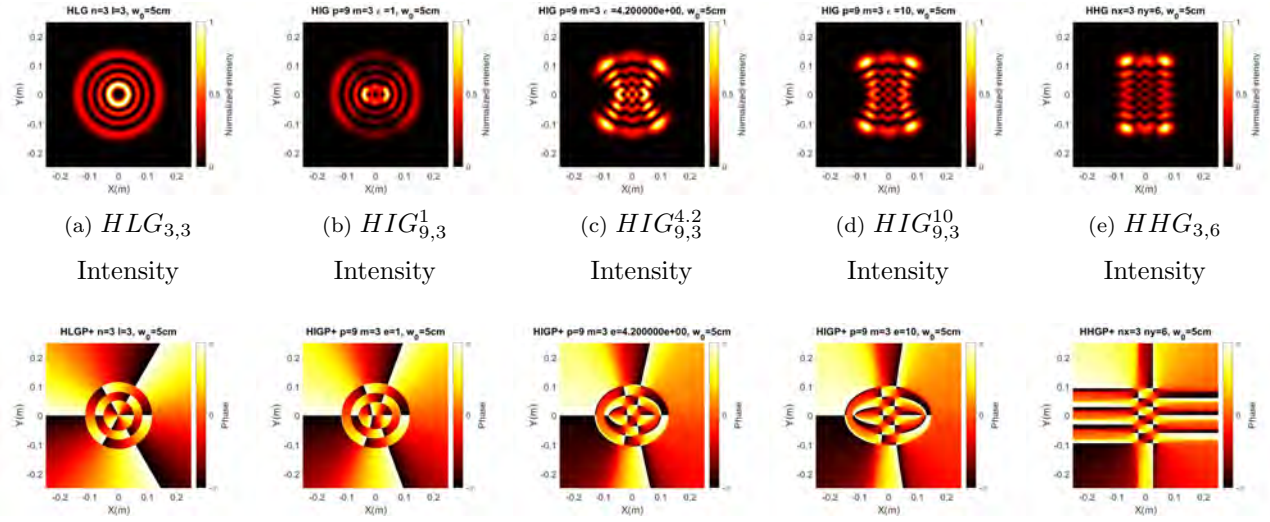

(a) $HLG_{3,3}$ Intensity (b) $HIG^{1}_{9,3}$ Intensity (c) $HIG^{4.2}_{9,3}$ Intensity (d) $HIG^{10}_{9,3}$ Intensity (e) $HHG_{3,6}$ Intensity

(f) $HLG_{3,3}$ Phase (g) $HIG^{1}_{9,3}$ Phase (h) $HIG^{4.2}_{9,3}$ Phase (i) $HIG^{10}_{9,3}$ Phase (j) $HHG_{3,6}$ Phase

Figure 2.11: Evolution of the ellipticity parameter for $HIG_{9,3}$, intensity (a) - e)) and phase (f) - j)) profiles. The chosen values of ellipticity are $\varepsilon = 0$, $\varepsilon = 1$, $\varepsilon = 4.2$, $\varepsilon = 10$ and $\varepsilon = 0$ from left to right for a) - e) and f) - j). The waist of the beams is $w_0 = 5cm$.

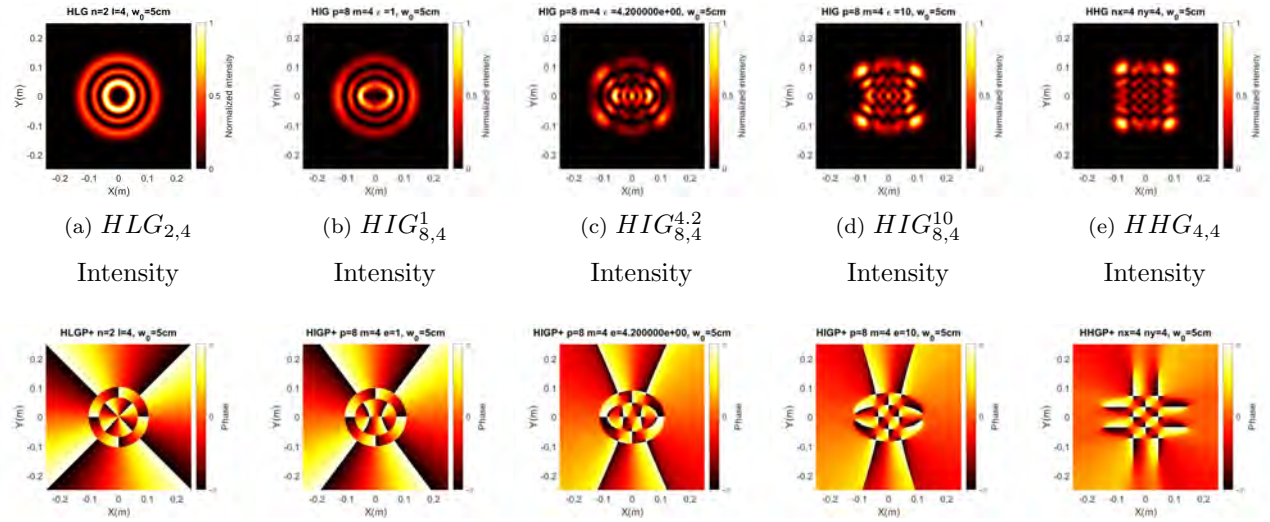

(a) $HLG_{2,4}$ Intensity (b) $HIG^{1}_{8,4}$ Intensity (c) $HIG^{4.2}_{8,4}$ Intensity (d) $HIG^{10}_{8,4}$ Intensity (e) $HHG_{4,4}$ Intensity

(f) $HLG_{2,4}$ Phase (g) $HIG^{1}_{8,4}$ Phase (h) $HIG^{4.2}_{8,4}$ Phase (i) $HIG^{10}_{8,4}$ Phase (j) $HHG_{4,4}$ Phase

Figure 2.12: Evolution of the ellipticity parameter for $HIG_{8,4}$, intensity (a) - e)) and phase (f) - j)) profiles. The chosen values of ellipticity are $\varepsilon = 0$, $\varepsilon = 1$, $\varepsilon = 4.2$, $\varepsilon = 10$ and $\varepsilon = 0$ from left to right for a) - e) and f) - j). The waist of the beams is $w_0 = 5cm$.

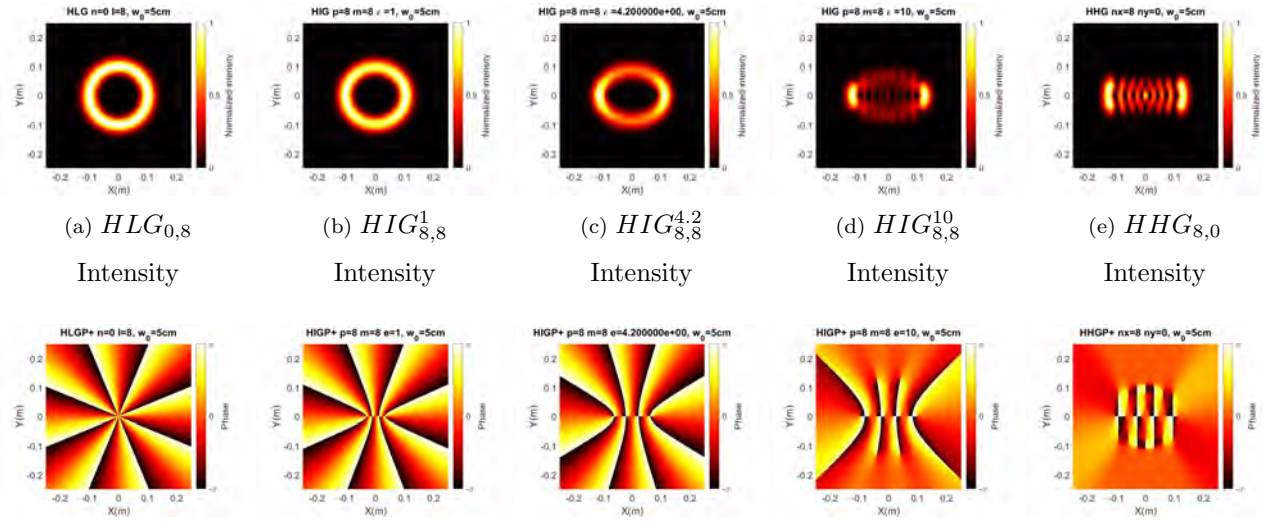

(a) $HLG_{0,8}$ Intensity (b) $HIG^{1}_{8,8}$ Intensity (c) $HIG^{4.2}_{8,8}$ Intensity (d) $HIG^{10}_{8,8}$ Intensity (e) $HHG_{8,0}$ Intensity

(f) $HLG_{0,8}$ Phase (g) $HIG^{1}_{8,8}$ Phase (h) $HIG^{4.2}_{8,8}$ Phase (i) $HIG^{10}_{8,8}$ Phase (j) $HHG_{8,0}$ Phase

Figure 2.13: Evolution of the ellipticity parameter for $HIG_{8,8}$, intensity (a) - e)) and phase (f) - j)) profiles. The chosen values of ellipticity are $\varepsilon = 0$, $\varepsilon = 1$, $\varepsilon = 4.2$, $\varepsilon = 10$ and $\varepsilon = 0$ from left to right for a) - e) and f) - j). The waist of the beams is $w_0 = 5cm$.

communications is of interest because of their structural sturdiness, which is given by the fact of being solutions of the Helmholtz equation. However, this sturdiness is only perfect for a completely isotropic medium. The atmosphere, in which these light beams are intended to propagate is, however, not and isotropic medium. For this, the introduction of atmospheric turbulence models is necessary in order to comprehend and estimate the effectiveness of Helical beams as information carriers. These atmospheric turbulence models are explored in section **2.4**.

2.4 Atmospheric turbulence modeling for light propagation

When light travels through the atmosphere, it travels though a medium where the refractive index is not continuous, but rather varies both spatially and temporally, due mainly to temperature variations on the atmosphere but also to other factors like pressure and the wavelength of light itself. This behavior of the propagation media randomly aberrates the wavefronts of light, say, a laser beam, a light source that is usually used for free space optical communications. This aberration of the wavefront gives place to an aberration of the initial mode, and therefore loss of the information the beam is carrying. So, in order to clearly understand how this change in beam structure is made, it is necessary to build models to represent the fluctuations of the refractive index in the atmosphere [45].

The refractive index of the atmosphere, due to this fluctuations of temperature and pressure can be expressed as:

$$n(\vec{r}) = n_{air} + \delta n(\vec{r}), \tag{2.53}$$

where $\delta n(\vec{r})$ represents the fluctuations of the refractive index and has a mean value $\langle \delta n(\vec{r}) \rangle = 0$.

With this in mind, while a beam is propagating, the effect of the turbulence on the beam can be viewed as a local change on the *phase* of the wavefront, due to the little changes of the refractive index. This phase change depends on the coordinates in which the phase is measured and acts on the beam traveling a distance Δz. Assuming a beam propagating in the z-direction through the air, it will experience a phase variation from point to point given by:

$$\delta\theta(\vec{r}) = k_0 \int_0^{\Delta z} \delta n(\vec{r}) dz. \tag{2.54}$$

If the turbulence is considered to be locally homogeneous and isotropic, the covariance function of $\delta n(\vec{r})$ only depends on the distance between points measured ($r = |\vec{r_1} - \vec{r_2}|$) instead of their respective coordinates as depicted in Figure 2.14 [46].

Using this consideration, the covariance function of the refractive index can be written as:

$$B_n(r) = \langle \delta n(\vec{r_1}) \delta n(\vec{r_2}) \rangle = \langle \delta n(0) \delta n(r) \rangle, \tag{2.55}$$

so that the covariance function for the phase can be written as

$$B_\theta(r) = \langle \delta\theta(\vec{r_1}) \delta\theta(\vec{r_2}) \rangle = k_0^2 \int \int_0^{\Delta z} \langle \delta n(0) \delta n(r) \rangle dz_1 dz_2. \tag{2.56}$$

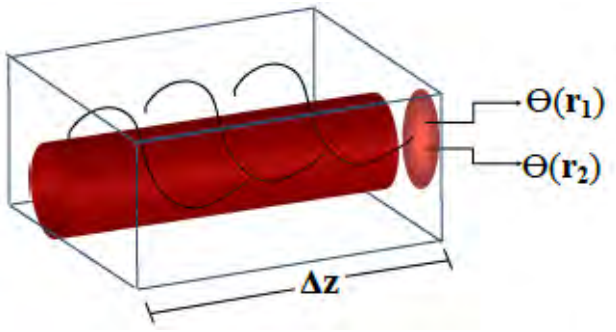

Figure 2.14: Measurement of the covariance function of phase considering a length differential Δz and the relative distance between transverse points.

From the covariance function, the so called *Power Spectrum* (Φ_n) can be derived by doing a three dimensional Fourier transform:

$$B_\theta(r) = \frac{1}{(2\pi)^3} \int \int \int_{-\infty}^{\infty} \Phi_n \vec{k} e^{-i\vec{k}\cdot\vec{r}} d^3 r. \tag{2.57}$$

The power spectrum represents a function that measures the phase fluctuation differences in the Fourier space, and therefore can be used to characterize the shape and strength of atmospheric turbulence in the Fourier space. Based on this, the phase change of a beam induced by atmospheric turbulence can be characterized by the inverse Fourier transform of a certain power spectrum function. [47]

In general, turbulence of a media is characterized by two kinds of turbulent cells: First, the outer scale cells, with square side size L_0 in the order of meters, which are the one that cause a beam to be randomly deflected from its path, causing fluctuations in the direction and position of the beam at the receiver aperture and are the biggest cell size possible of the turbulence. On the other hand, the inner scale cells, of square side size l_0, in the order of millimeters are responsible of the small scale effects that distort the wavefront resulting in a randomly aberrated phase (and intensity distribution) at the receiver end.

While turbulence models using this characteristic cells typically provide only statistical averages for variations of atmosphere, they are sufficiently effective to describe the effects of turbulence. The first model of these approaches is the Kolmogorov model of turbulence, that assumes $l_0 = 0$ and $L_0 = \infty$, which yields a power spectral density of the refractive index fluctuations $\Phi_n^K(\kappa)$ given by [48]:

$$\Phi_n^K(\kappa) = 0.033 C_n^2 \kappa^{-11/3} \text{ for } 1/L_0 \ll \kappa \ll 1/l_0. \tag{2.58}$$

Here, κ is on the angular spatial frequency vector and C_n^2 the refractive index structure parameter, which is an indicative of how *strong* the turbulence is as an average and in general is a function of both wavelength of signal and height at the atmosphere, and thus can be considered a constant for horizontal propagation. However, a more precise turbulence model power spectrum, that considers non-zero finite size of the turbulence cells can be obtained as an extension of the Kolmogorov model: The von-Karman power spectrum [47]. For this model, the power spectral density is given by:

$$\Phi_n^{vK}(\kappa) = 0.033 C_n^2 \kappa^{-11/3} \frac{\exp(-\kappa^2/k_m^2)}{(\kappa^2 + k_0^2)^{11/6}} \text{ for } 0 \leq \kappa < \infty, \tag{2.59}$$

with $k_m = 5.92/l_0$ and $k_0 = 2\pi/L_0$. This model has the main advantage of considering quantities smaller than l_0 and bigger L_0 and some easier numeric calculations. This is the power spectrum that is used in calculations for this work.

By using these, or any other kind power spectrum depending on the used model, it is possible to generate individual snapshots of turbulence in the form of phase screens, that if are applied to a certain electric field profile and then propagated by using either an impulse response or a transfer function, give as a result a beam profile function with the effects of atmospheric turbulence in it. An example of these phase screens and the results of applying them to a certain field is shown in Figure 2.15. In this figure, a comparison on the effects of propagation of an $HIG_{5,3}^2$ initial mode a) are shown. A comparison is made between the beam

propagated $4km$ with b) and without c) turbulence, finally, an example of random turbulence phase-screen is depicted in d).

When measuring the effectiveness and robustness of a light beam profile for its usage in optical communications, there are plenty of parameters to be considered, but for the results in this particular work, there are three main measurements that ware taken into account: the scintillation index, the strehl ratio and the overlap.

The scintillation index σ^2 is a number representing the intensity variance of a light beam, meaning, it is a number that measures how much the brightness of the beam changes during propagation at a certain point or how much the beam scintillates, hence the name. The scintillation index is given by [49]:

$$\sigma^2(z') = \frac{\langle I^2(z')\rangle - \langle I(z')\rangle^2}{\langle I(z')\rangle^2} = \frac{\langle I^2(z')\rangle}{\langle I(z')\rangle^2} - 1, \tag{2.60}$$

where $I(z')$ is the intensity of the beam profile at a certain distance of propagation z'. The smaller the value of σ^2 the more *stable* the beam is.

The strehl ratio SR is defined, in the case of this work as:

$$SR(z') = \frac{I(z')}{I_0(z')}, \tag{2.61}$$

where I_0 is the total intensity of the beam while propagating with no turbulence. This quantity gives a measure of how much of the turbulence propagated beam intensity goes out of a window defined by the size of the beam without turbulence. The closer the value of the strehl ratio is to 1, the less the beam is distorted or deviated by atmospheric turbulence. It is important to notice that this quantity in some other works regarding atmospheric turbulence [45] takes mean values of intensity instead of total intensity, while the original description of strehl ratio actually comes from optical design, were it describes the ratio of peak focal spot intensity of a manufactured optical system to the diffraction-limited peak intensity. In general, it is a measure of how much the intensity of a beam is *well directed* in a system.

Finally, the overlap **OV** (also refered as fidelity) of a light beam refers to how much the initial beam power is kept in the original selected mode after propagation, and is defined by a ratio of inner products of the original beam and the propagated one [45]:

$$OV(z') = \frac{\int\int_{-\infty}^{\infty} E(x,y,z')\bar{E}(x,y,z')dxdy}{\int\int_{-\infty}^{\infty} E(x,y,z')\bar{E}'(x,y,z')dxdy}, \tag{2.62}$$

where $E(x,y,z')$ refers to the transverse electrical field of the mode propagated a distance z' *without* turbulence and $E'(x,y,z')$ the mode after propagation through turbulent media, $\bar{E}(x,y,z')$ and $\bar{E}'(x,y,z')$ are

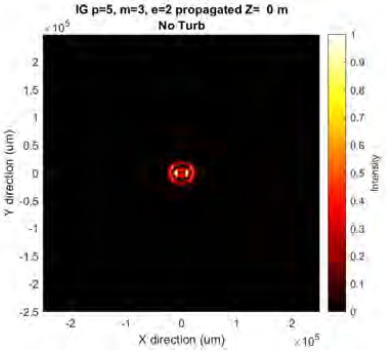

(a) Initial $HIG^2_{5,3}$ beam profile

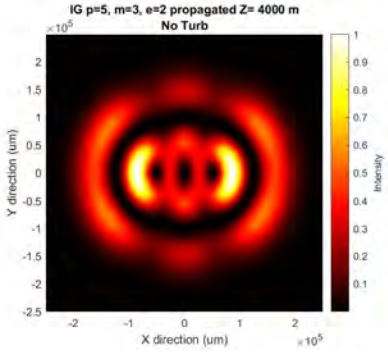

(b) $HIG^2_{5,3}$ beam propagated 4000m without turbulence

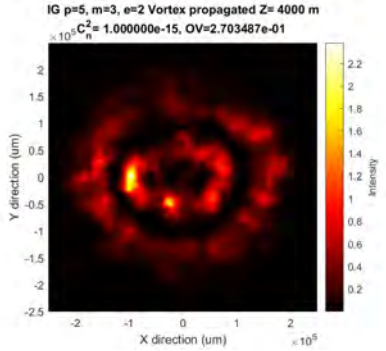

(c) $HIG^2_{5,3}$ beam propagated 4000m with simulated turbulence

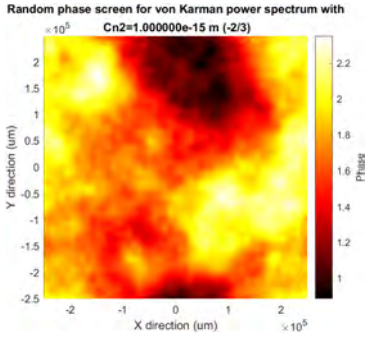

(d) Example of multiple random turbulence phase screens applied to the propagated beam

Figure 2.15: Results of applying a series of random phase screen to a beam profile. a) Corresponds to the initial $HIG^2_{5,3}$, $w_0 = 1cm$ intensity profile. b) and c) depict the beam after propagatin $4km$ with and without turbulence and d) is an example of a turbulence random phase-screen.

the respective complex conjugates of the fields. Assuming normalized electric fields, OV can take values between 0 and 1, meaning total lost or total conservation of the original beam transverse profile. This loss of intensity on the initial beam mode is due to the changes experimented by the propagated beam through turbulent media, which changes its phase, and thus its intensity distribution randomly, making the photons *leak* into other spatial modes. The description of this leakage of modes can be done in any basis. This value is particularly important in the real of communication systems as it directly measures the *robustness* of a certain mode to keep the same beam profile through atmosphere, meaning that if information is encoded in that particular mode, the bigger the overlap value, the less loss of information is perceived at the receiver's end.

Another quantity to measure the robustness, and usually more used in the literature is the crosstalk (**CT**) of a mode, simply defined for normalized modes as:

$$CT = 1 - \frac{\int\int_{-\infty}^{\infty} E(x,y,z')\bar{E}(x,y,z')dxdy}{\int\int_{-\infty}^{\infty} E(x,y,z')\bar{E}'(x,y,z')dxdy} = 1 - OV, \tag{2.63}$$

which measures how much leakage of modes there is in a propagation. For the presentation of this work the quantity OV is used for practicality and presentation.

Chapter 3

Generation of OAM carrying beams using Spatial Light Modulators

In this chapter, the generation of Helical Ince-Gauss in laboratory was explored, doing this using Spatial Light Modulators, devices capable of generating localized gradients of refractive index, that result in phase shifts applied to light beams incident on them. By generating special phase masks in MATLAB from the superposition of several weighted Laguerre-Gaussian modes, applying these into SLMs and using an imaging system, Helical Ince-Gaussian modes were produced.

3.1 Spatial Light Modulators

In order to engineer complex optical fields many devices had been developed for the manipulation of typical beam transverse profiles, such as Gaussian beams, that change the characteristics of the electrical fields in order to engineer complex optical fields *ad hoc*. Some of these devices include microelectromechanical systems (MEMS) and digital micromirror devices (DMDS), but the ones specifically used in this work are liquid crystal based spatial light modulators (SLM).

Liquid crystal is a phase of matter, reachable in certain materials, in which the properties of the molecular order of said materials lay between liquid and those of a crystal, as they present certain kinds of anisotropy only seen in crystals but also show flow behavior of liquids, with random position and orientation of molecules. This orientation of the molecules can be manipulated by applying an external electric field (voltage) into the material, which rotates it, and therefore rotates the optical axis of the material. Because of the before mentioned anisotropy trait, liquid crystals exhibit a voltage-dependent birefringence, being the angle of rotation of the crystal θ_c a function of applied voltage. [50]

These properties of liquid crystals are used in liquid crystal spatial light modulators: Arrays of cells with liquid crystal inside, each of them with an individual external voltage control. This makes that the system has a localized retardation modulation, that translates to a phase or polarization imprinting into a light beam incident in the device, whether the beam is reflected or transmitted. Spatial light modulators, with a prior adequate system calibration, can be used then for the purpose of implanting a phase pattern into an incident light beam, thus changing their spatial structure an making possible the engineering of complex beams, in particular for this work, elliptical vortex beams.

3.2 Building of IG profiles as decomposition of LG modes

In order to define an adequate phase pattern to be put in an SLM for the production of Ince-Gauss modes, the mathematical expressions of the beams need to be implemented, however, an analytical expression for Ince-Gaussian modes of varying ellipticity is rather complicated to get. Because of this, it was necessary to do a decomposition of the desired elliptical beam profiles into an easier to implement basis: The Laguerre Gaussian modes. As was demonstrated in section **2.2**, any Ince-Gauss mode can be decomposed into the family of Laguerre-Gauss modes, by means of equation (2.40). Based on this, a decomposition of Ince-Gauss profiles into the family of Laguerre-Gauss modes was implemented. The decomposition algorithm was developed by Dr. William N. Plick of the University of Dayton, while the implementation of this algorithm in MATLAB was done by the author of this text. The aforementioned procedure was as follows:

The main idea of the algorithm is first to obtain a representative matrix of the IG mode to be transformed. Then, using the correct eigenvalues of the obtained matrix, which depend on the m and p parameters, and applying the inner product expression in (2.2), a decomposition into LG modes can be derived.

As shown in equation (2.37), the number of modes that form a complete sub-basis of the orthogonal modes, as well as the possible decomposition of a certain mode into another depends entirely on the value of the order p, and as such the size of the representative matrix depends on that value. So, given the values for the desired IG modes to be decomposed (order p, degree m, ellipticity ε and helicity h, the dimentionanility of the representative matrix was determined depending on the parity and order p. Then, the elements of the matrix were found using the harmonic decomposition of the Ince-Polynomials and their respective recurrence relations, initially developed by Bandres et al. [35]. The eigenvectors of the resulting representative matrix were obtained, and the specific eigenvector for the desired mode chosen and normalized. After that, using the transformation rules brought up in **section 2.2**, the LG modes available for the decomposition were determined, and using the inner product relation of equation (2.2) directly applied to the determined eigenvector,

the weight of each of these modes was calculated and normalized.

This whole procedure was done twice, to get the weighted LG decomposition of both even and odd parity IG modes and the results were retained in matrices for both even and odd modes decomposition. The used code is shown in **Appendix A**.

3.3 Phasemask patterns for OAM carrying beams

In order to create engineered complex optical fields using SLM's, the information of these beams needs to be *imprinted* into an incident light field, typically a Gaussian beam, as is the kind of spatial profile that comes out from most LASERs. Because of this, knowing the actual electric field distribution of the desired profile is crucial. In the case of making scalar IG modes, the only thing that is necessary to engrave the desired mode into the incident Gaussian beam is the *phase profile* of the desired mode, as this information directly makes the mode *mold* into a Gaussian profile modulated by the specific parameters of the IG mode.

The phase profile of a desired mode was obtained from the resulted electric field matrix, that was calculated from the decomposition of the desired IG mode into LG modes. Each of the weighted LG modes obtained from the decomposition described in **section 3.2** was built into a NxN matrix with physical element size u by implementing a transformation of Cartesian coordinates to Cylindrical ones and using the equation (2.23) to fill the value of each element. All of the resulting matrices were then added together, obtaining a NxN complex matrix with the electric field for the desired IG mode. The NxN phase matrix of the whole mode was then obtained simply by calculating the argument of the electric field at each matrix element.

Finally, in order to get a correct modulation of phase using an SLM, a calibration curve for the device must be made. Once having an adequate calibration curve, it is applied to the phase matrix and the resulting calibrated phase matrix is embedded into the SLM. An example of these phase profiles is given in Figure 3.1

In some experimental arrangements, the complex field coming out of the SLM (either transmissive or reflective) is required to be redirected at a certain angle. This is done by inserting a diffraction grating expression into the phase profile, especifically a blazed diffraction grating [51], that makes most of the power of the transmitted or reflected beam reside into the first diffraction order. The addition of this grating gives place to a *OAM fork* for phase patterns deriving from an OAM mode. These are shown in Figure 3.2.

In the case of this work, the different calibration curves were given but the process of calibration involves measuring the retardation given by the SLM cell as a function of the applied voltage as is well explained in [46].

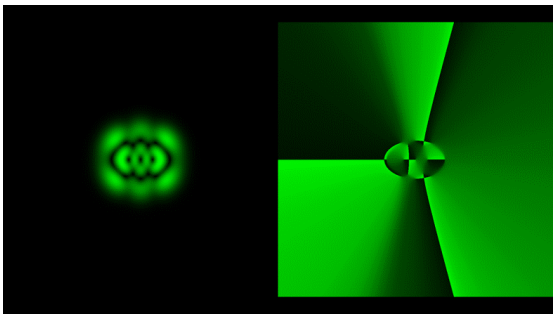

Figure 3.1: Example of SLM phase profile used to generate an $HIG_{5,3}^{4.2}$ mode out of a Gaussian beam. At the right lays the desired mode and at the right the phase mask to be put in the SLM, already calibrated in order to generate the desired optical field.

3.4 Modes generated and considerations

To generate helical Ince-Gaussian beam profiles, the experimental arrangement design by Qiwen et al. [52] shown in Figure 3.3 was used [52]. This optical system is capable of generating custom complex beam profiles, with full control on the phase, amplitude, polarization and retardation parameters on the desired electric field profile, doing this by using a combination of spatial filters, polarizers, quarter-wave plates, beam splitters and reflective SLM's implemented in a series of 4F imaging systems with magnification $M = 1$. The three channel (RGB) capability of the two SLM was put into use in this setup by applying two different phase patterns in each half of each SLM, one in the R channel and the other in the G one. These implemented phase channels in both SLMs, in combination with the calibration of the other optical elements, gave the desired modulation of the four mentioned parameters (two per SLM) and thus, by applying a certain optical field (Gaussian beam laser profile), the target complex optical beam could be obtained at the output.

In the case of generation of scalar vortex beams, such as different HIG beams, the only parameter that was necessary to modulate was the phase, because of the Gaussian beam profile already coming out of the laser source. As such, only modulation on the SLM1 was used, in the G channel especifically. An example of these designed phase patterns on an SLM is shown in Figure 3.4 . These phase patterns were inserted into a Holoeye HEO 1080p SLM using a HE-NE Laser light source at 632.8 nm emission.

3.4.1 Imaging of Helical Ince-Gauss modes in the far field

Examples of some generated modes of the previously discussed families of Helical beams that were imaged into an Spiricon CCD camera using the system in Figure 3.3 are presented in Figure 3.5.

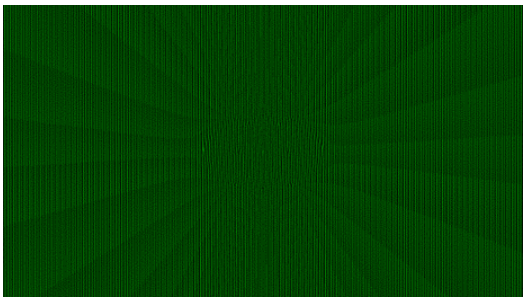

(a) Example of OAM fork for $HIG_{5,3}^{+,5}$ mode

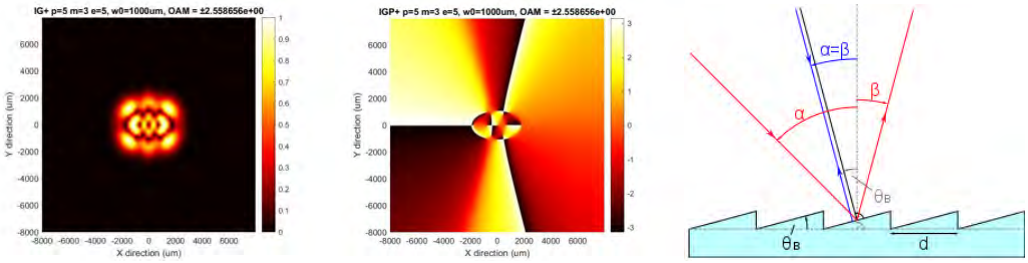

(b) Desired mode intensity (c) Phase of the desired mode (d) Blazed diffraction grating

Figure 3.2: Example of an OAM fork used to generate a $HIG_{5,3}^{5}$ mode for $\lambda = 405nm$ at a 3. Using a blazed diffractive grating ensures that most of the original power that arrives at the modulating SLM is reflected (or transmitted) at the desired angle. Notice that the the diffraction grating is embedded into the phase of the desired beam, making a *fork-like* figure.

It is demonstrated in Figure 3.5 that the method used for the imaging of the Helical beams was effective, as characteristic features of OAM carrying beams can be observed: It is shown that the physical size of the beam is modulated by the values of order p and degree m used for each beam, all of which transformed into the IG basis would correspond to: a) $HIG_{1,1}^{0}$, b) $HIG_{4,4}^{0}$, c) $HIG_{8,2}^{2}$ and d) $HIG_{7,3}^{\infty}$. More *complex* beams (with higher order and degree) tend to be bigger in size but with maximum point intensity lower than that of *simpler* profiles. This size relation agrees with the fact that HLG modes exhibit bigger physical size when the OAM value of the beam increases. Additionally, the distinctive zero-intensity points of Helical beams derived from phase indeterminations are observed at the expected positions of the beam profile, to a certain extent.

The fact that the beams could be imaged with good degree of fidelity gave the opportunity to image the evolution of a certain transverse mode varying its ellipticity (and thus its symmetry), as was depicted in Figures 2.10- 2.13. In particular, the imaging of the evolution of the ellipticity parameter for a $HIG_{5,3}$ mode is displayed in Figure 3.6.

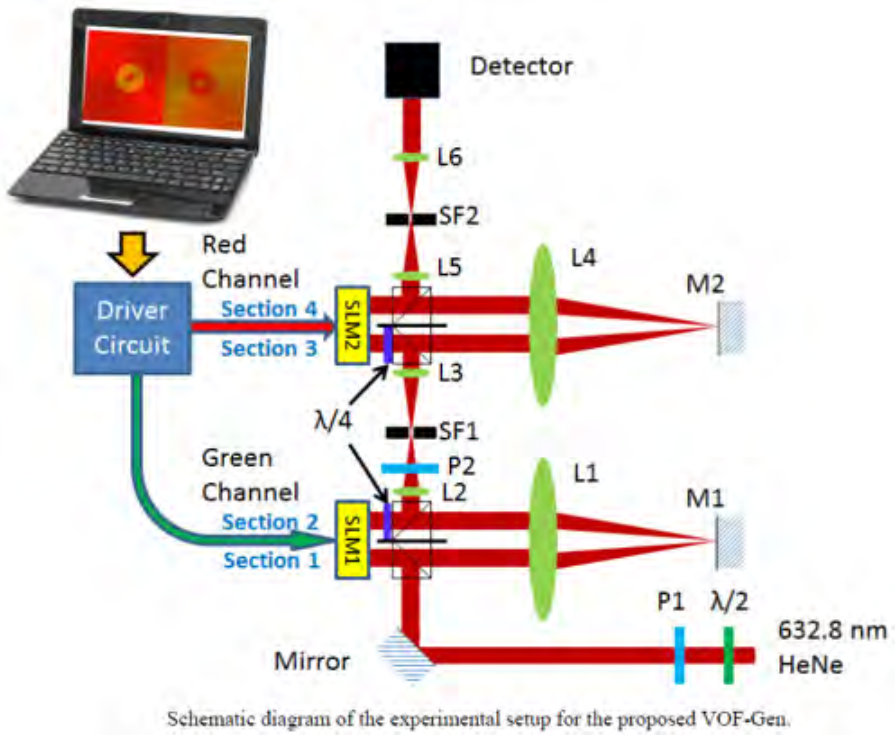

Figure 3.3: Experimental setup used for the generation of custom complex optical beams. 2 SLMs configure the phase, amplitude, polarization and retardation parameters using a combination of phase patterns and four imaging systems.

As expected from the previous result, the resulting modes present a similar physical size due to having the same order and degree. They also show the characteristic zero-intensity phase discontinuity points in the beam transverse profile.

However, even with the main characteristics of the transverse profiles Helical modes portrayed in Figures 3.5 and 3.6, the obtained intensity profiles were not equal as the ones expected to get. This was especially the case in modes with greater p and m values, as some of the the smaller vortexes were heavily distorted or not detected. This issue can be attributed to an small misalignment in the optical systems due to its high sensitivity distance changes of the elements. In particular, a misalignment in the image plane (camera) plane was the main reason of these issues, that could not be solved due to time constrains and difficulties to the access to the optical system. However, this situation is easily solvable by adjusting the optical elements to the correct distances and relative tilt.

As an alternative to the imaging of the mode was to let the beam profile propagate until the far-field intensity pattern was visible. In order to do this, the collimating lens $L6$ on Figure 3.3 was removed, as well

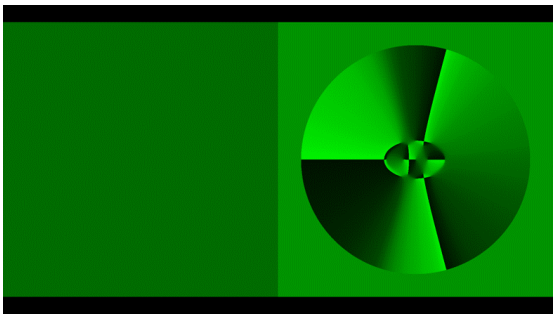

Figure 3.4: Example of SLM pattern displayed in $SLM1$ of Figure 3.3 for the generation of a $HIG_{5,3}^{+,4.2}$ mode. The right part of the image would correspond to Section one, controlling the phase of the input Gaussian beam. The left part would be left at a value in which the reflectivity was maximum for the chosen wavelenght. The circular pattern shown in the phase patter was made to collect only the light at the center of the beam.

as the detector, and the beam was let propagate freely for a distance of approximately one meter, in which the far field intensity(that was brought up to the camera by the $L6$ lens) pattern was visible. The results of doing this for some beams is presented in Figure 3.7.

While the intensity profiles are recognizable in Figure 3.7, from b) it is clear that there was a slight misalignment in the elements of the optical system, due to the distorted shape with which the beam ended up propagating. This misalignment is however easily fixed as mentioned before.

Nonetheless, this procedure further demonstrated that this kind of Helical beams can be produced for any desired applications, using adequate equipment and experimental setups.

3.4.2 Imaging of Helical Ince-Gauss modes in the near field

A characteristic of Helical beams that is usually ignored is the intensity profile in the near-field, since these beams are usually propagated to a distance that allows the far-field detection. However, the near-field patterns of these beams may be useful in beam detection schemes, as these patterns are strongly related to the 2D-Fourier transformation of the desired beam profile. In order to view the near-field intensity pattern of the beam, the detection camera was positioned between the spatial filter $SF2$ and imaging lens $L6$ in Figure 3.3, and the results of some of the modes observed are presented in Figure 3.8.

It is a very interesting (while expected) result that the near-field intensity patterns of the observed modes retain zero-intensity points in the expected position from the far-field profile, with the important difference that these zero intensity points are very clearly defined. Especially the one that is observed in the $HLG_{0,4}$

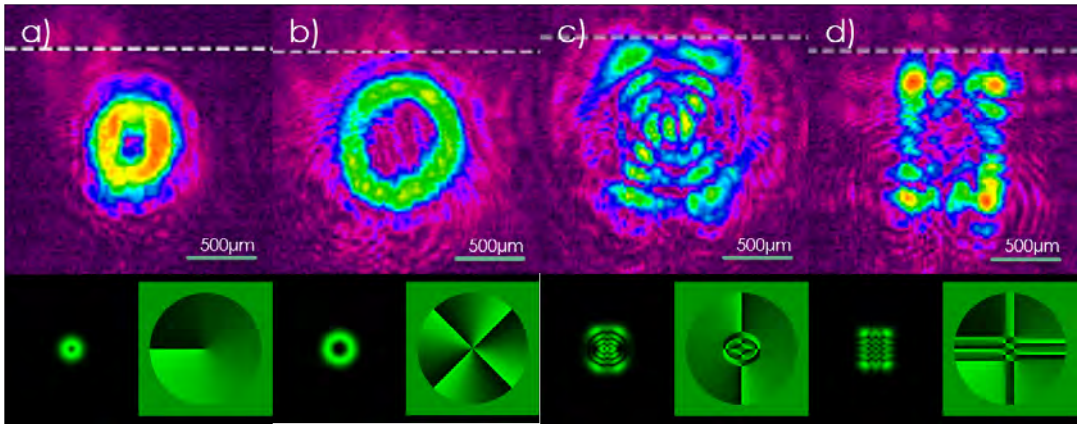

Figure 3.5: Generation of various Helical beams: a) $HLG_{0,1}$, b) $HLG_{0,4}$, c) $HIG^{4}_{8,2}$ and d) $HHG_{3,4}$. Below every mode lays the desired transverse intensity profile, as well as the phase profile put in the SLM in order to generate said beam.

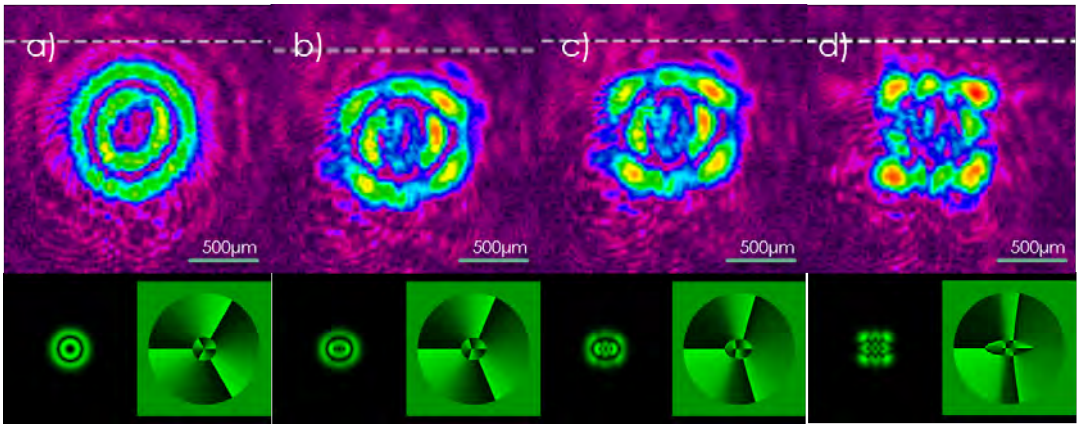

Figure 3.6: Evolution of $HIG_{5,3}$ mode transverse intensity profile with the ellipticity parameter. a) $\varepsilon = 0$, b) $\varepsilon = 1$, c) $\varepsilon = 4.2$, d) $\varepsilon = 15$, each with the expected intensity profile and the used SLM phase pattern.

mode, in which the size of the optical vortex is considerably bigger than in other modes. This is related to the value of the phase discontinuity (and thus OAM) of each phase indetermination, as the $HLG_{0,4}$ mode has an indetermination of $2 * 2\pi$ while the other modes have individual 2π ones. Due to this characteristic of the phase discontinuities at the near field, the idea of using the zero-intensity points patterns to *determine* the characteristics of Helical beams in a detection scheme arises, as the optical vortex position seems to be easier to detect in the near-field than in the far-field.

For the HIG mode, it is also possible to obtain the evolution of this mode as a function of the ellipticity. This is shown in 3.9.

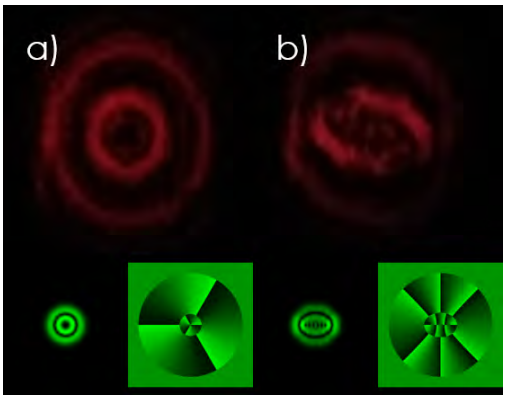

Figure 3.7: Examples of far-field intensity patterns of Helical beams without using a detector. a) $HLG_{1,3}$, b) $HIG^{4}_{8,6}$, both modes with the expected intensity profile and SLM phase profile. The size of the beam profiles is in the order of centimeters.

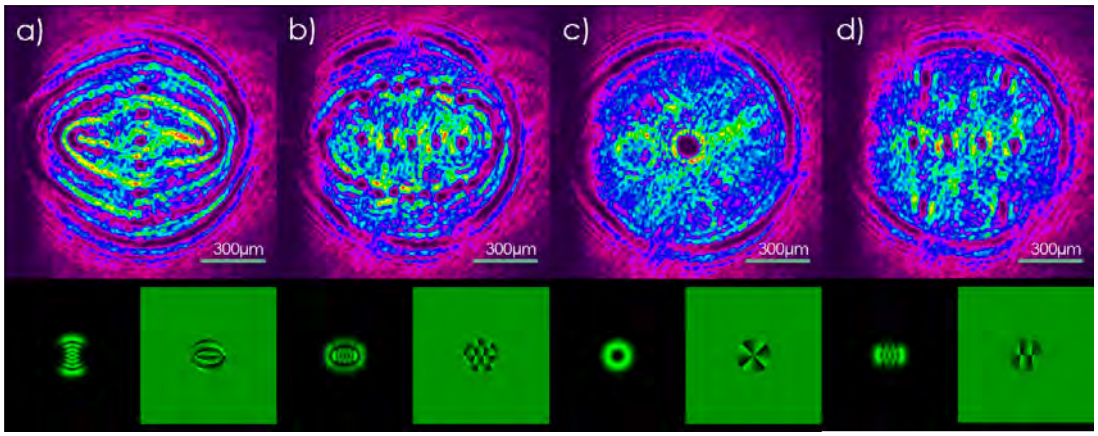

Figure 3.8: Generation of various Helical beams intensity profiles in the near field: a) $HIG^{5}_{7,1}$, b) $HIG^{5}_{7,7}$, c) $HLG_{0,4}$ and d) $HHG_{4,0}$. Below every mode lays the far-field intensity profile, as well as the phase profile put in the SLM in order to generate the beam.

It's clearly seen from 3.9 the change that occured to the OAM vortices of a beam with the change of ellipticity. The mode $HLG_{1,3}$ (a), initially had central indetermination $3 * 2\pi$ at the optical axis of the beam. When the ellipticity of the mode is increased, the central indetermination was split into three 2π indeterminations that remained as the beam changed. The bigger the ellipticity was, the more off-axis 2π indeterminations appeared, changing the general mode OAM value and having a certain distribution pattern for each mode *and* ellipticity.

Regarding the quality of the modes detected, a ring-like low intensity region can be appreciated surrounding the optical vortexes. This region appeared due to the window size in which the input beam was incident

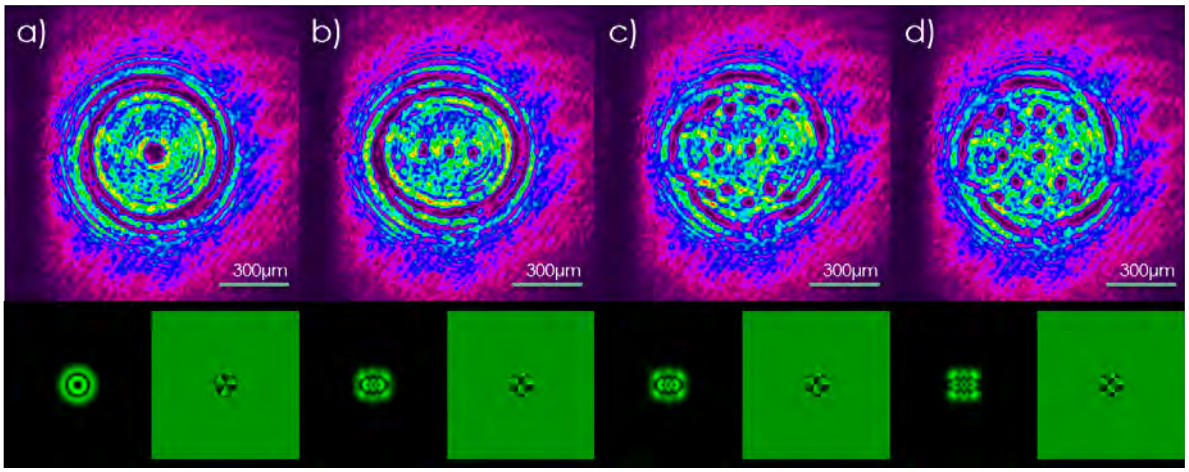

Figure 3.9: Evolution of $HIG_{5,3}$ mode transverse near-field intensity profile with the ellipticity parameter. a) $\varepsilon = 0$, b) $\varepsilon = 1$, c) $\varepsilon = 4.2$, d) $\varepsilon = 15$, each with the near-field intensity profile and the used SLM phase pattern.

in the phase pattern put in the SLM. The central region of the beam appeared to be distorted as well, due to the fact that the input beam used in these cases was unfiltered. These issues can be easily fixed by using a bigger radii input beam acceptance region for the phase patterns, as well as a low-pass filter to clean the input signal. Unfortunately, due to time constraints, these actions were not performed.

3.5 Partial conclusions on Generation of OAM beams using Spatial Light Modulators

In this section, the possibility of generating OAM-carrying helical beams with adecuate optical devices was demonstrated even with the technical difficulties and consideration that the process of generation of the beams may convey. The evolution of these helical beams with the ellipticity parameter was observed, verifying as well the retention and splitting of the OAM phase initial phase indetermination, as well as the creation of new zero-intensity points. This characteristics of OAM beams and their evolution with the ellipticity parameter were again recognized using the near-field intensity patterns, in which the indeterminations are more easily recognizable and well defined. As such, the possibility of using this characteristics of the near-field intensity pattern for the detection of different Helical beams is given.

Chapter 4

Atmospheric propagation of helical Ince-Gaussian modes

In this section it is explained how several MATLAB®scripts were made in order to simulate propagation of elliptical scalar vortex beams through the atmosphere, the parameters that were used for the simulations and the different considerations to be taken into account. Parameters such as the ellipticity ε of the beams, the choose of modes with varying order p and degree m and the values of the refractive index structure parameter C_n^2 were the main focus these simulations. The results of these simulations were then analyzed and general conclusions on how these modes would behave under atmospheric turbulence were made.

4.1 Propagation of modes through atmospheric turbulence procedure and considerations

The general idea of the atmospheric turbulence propagation codes was to determine a matrix method in which a complex matrix of dimensions NxN could contain the transverse electric field profile of a desired HIG mode. In order to do this, the initial parameters of the beam matrix, such as the matrix size N and the matrix physical size L(in microns) were selected. After that, the initial beam parameters, such as the wavelength λ, beam waist w_0, order p, degree m and ellipticity were chosen and the resulting expression of the HIG mode was implemented into the NxN matrix, taking this expression by decomposing the desired HIG mode into a superposition of LG modes, as was done in section **3.2**. This was due to the easier implementation of Laguerre polynomials compared to Ince polynomials. Next, the total distance of propagation ZT as well as the total number of distance divisions n_{div} was selected, in order to evaluate the dynamics of the modes at selected different distances. Then, the atmospheric turbulence parameters, such as C_n^2, the power spectral density Φ_n and the distance between random phase screens d_{scr}, representing the atmospheric

turbulence, was chosen. Finally, an adequate number of times to propagate the mode n_{prop} was implemented, in order to get a reliable average result of measured quantities. This was done due to the random nature of refractive index fluctuations in the atmosphere, resulting in no beam propagation being the same and thus having to rely on average results.

Once the initial conditions were defined, as well as the initial beam profile matrix was obtained, the following algorithm was used: A random phase screen of the same size and dimension as that of the beam, representing the atmospheric turbulence, was generated and multiplied by the beam profile matrix. The result of this was then Fourier transformed and that propagated a distance d_{screen} using a transfer function, to eventually apply an inverse Fourier transform and by doing that get a new beam profile matrix. This process was repeated until a distance corresponding to a multiple of ZT/n_{div} was reached and at that point, the measurement of the scintillation index, overlap and strehl ratio was performed, comparing the turbulence propagated beam profile to one with the same initial conditions, but propagated the same distance without atmospheric turbulence ($C_n^2 = 0$). The results were stored and the process repeated until the total distance ZT was reached, at which point, a check on the number of propagations was performed and if it was not equal to n_{prop}, the whole process was repeated. Until reaching the propagation number n_{prop}, at each distance multiple of ZT/n_{div} the beam profile was stored, as well as its phase profile and at the end of the cycle, an average for each of the measurements over all propagations n_{prop} was made.

The generation of the random phase screens, based on works such as [53] was as follows: A pseudorandom NxN array of complex numbers was generated, and then multiplied by $2\pi/(N\Delta_k)\sqrt{2\pi k^2 d_{scr}\Phi_n}$, having Δ_k the spatial sampling interval in the Fourier space. The result was then inverse Fourier transformed, getting a real space complex random phase field, choosing in this case the imaginary part of said phase field as a random phase screen. Is as well noteworthy to indicate that the turbulent atmospheric beam propagation algorithm here presented is heavily based on previous work by Qiwen et al. [54] and Sevilla [46], by using modified versions of their turbulence propagation algorithms even thought the mentioned works were only focused in HLG modes, both in the scalar and vector cases.

As for the way in which the values of scintillation index, overlap and strehl ratio were calculated, some points have to be addressed. In the case of the overlap integral, the expression of equation (2.62) was used, having the beam profile matrix affected by turbulence as $E'(x, y, z')$ and the one propagated without turbulence as $E(x, y, z')$, straining the limits of the integrals to the size of the matrices.

The scintillation index as well as the strehl ratio are very shape-dependent measurements. For the scintillation index this is because the mean value of intensity varies heavily from point to point depending on the geometrical shape of the transverse profile. For the strehl ratio, it is because the size of the complete beam

profile matrices is in general bigger than that of the transverse profile itself. Therefore, a reference region for the evaluation of these values was delimited. The limit of said region was defined by the last elements of the no-turbulence propagated beam profile to have an intensity greater than or equal to $1/e^2$ the maximum intensity value of the whole beam profile. This limit region for measurements is pictured in Figure 4.1, where a $HIG^2_{5,3}$ mode, propagated with and without turbulence is shown. The no-turbulence propagated profiles defines the strehl ratio and scintillation index measurement region for the turbulence propagated beam characterization.

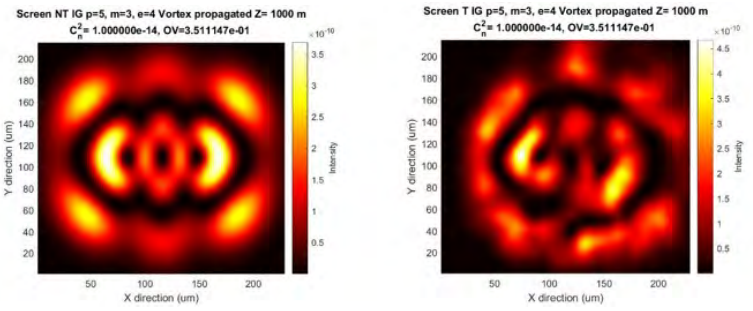

(a) Reference window (b) Turbulence beam window

Figure 4.1: Example of a) reference window a) and b) measurement window for $HIG^4_{5,3}$. As can be graphically seen, some of the power from the turbulence propagated beam escapes from the measurement window, heavily affecting the value of the Strehl ratio, the Scintillation index is affected by the distortion on the intensity profile of the beam, caused by the turbulence.

4.2 Beam propagation simulation: results and analysis

Using the described method of simulation of beam propagation through atmospheric turbulence, different Helical Ince-Gauss modes were chosen to be propagated, varying their ellipticity values, order, degree and the strength of the turbulence, indicated by the value of C_n^2. For the realized simulations, some initial beam parameters remained the same, in order to keep consistency in the obtained results. These rigid parameters were: The size of the matrix $N = 1024$, the physical size of the matrix $L = 50cm$, the wavelength $\lambda = 632.8nm$, the initial beam waist size $w_0 = 10000\mu m$, the inner scale $l_0 = 1cm$, the outer scale $L_0 = 3m$ and the number of propagation per simulation $n_{prop} = 200$. The combination of these values proved to be adequate both for feasible beam propagation experiments and the simulation algorithm here presented. For the case of the refractive index structure parameter, its value varied from $C_n^2 = 10^{-14}m^{2/3}$ to $C_n^2 = 10^{-16}m^{2/3}$, representing strong to weak turbulence values for the chosen wavelength [47]. Finally, the chosen power spectrum was the von-Karman power spectrum from equation (2.59), as it brought accurate results and an

easy computational implementation.

4.2.1 Propagation of a single Helical Ince-Gaussian mode

The first simulation performed was the propagation of a $HIG^2_{5,3}$ mode through $4000m$, with $C_n^2 = 10^{-15}m^{2/3}$. The initial mode intensity and phase profiles are shown in Figure 4.2, while the results of these propagations for the intensity profile and the corresponding phase profiles with a comparison to non-turbulence propagation profiles are shown in Table 4.1. As a side note, the different tables presented in this chapter will be positioned at the end of it for better aesthetics of the text.

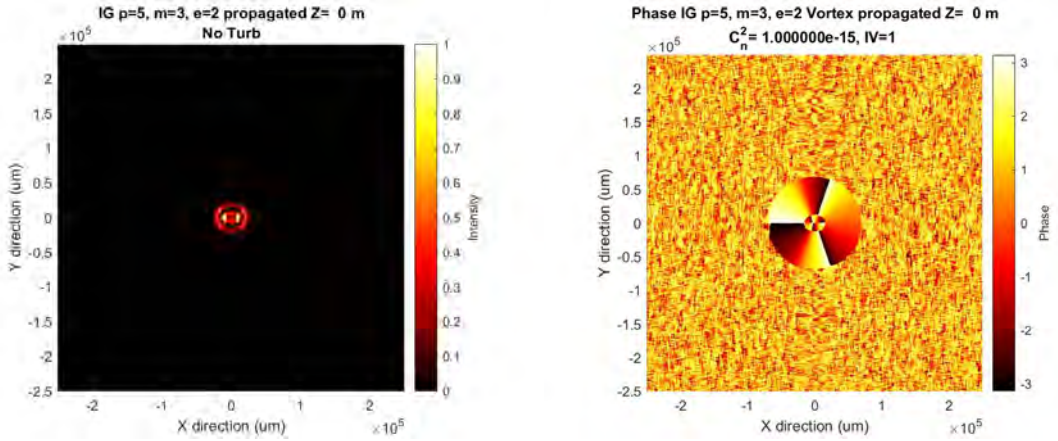

(a) Original mode intensity

(b) Original mode phase

Figure 4.2: Initial beam intensity and phase profiles of $HIG^2_{5,3}$ beam.

From the visual results shown in Table 4.1 it can be seen that for the chosen conditions of propagation, the intensity distribution is kept almost the same for most of the propagation, except further away than 3000 meters, where the intensity profiles zero intensity regions can not be individually distinguished. However, by looking at the phase distribution of the beam it can be clearly detected that the three characteristic 2π phase discontinuities of the beam, while dislocated from their initial positions relative to each other, remain intact throughout the whole propagation inside the beam. This behavior could imply that for long distance propagation, the HIG beam retains most of its *general* structure, in particular its vortex structure that keeps well defined, even thought the intensity one may not be as clearly identified. The preserving of the phase vortexes is exemplified in Figure 4.3.

It is worthy to note as well that the phase patterns obtained, specially for the relatively short distance cases (500m and 1000m) present a speckle-like pattern of random phases, that is due to the random phase

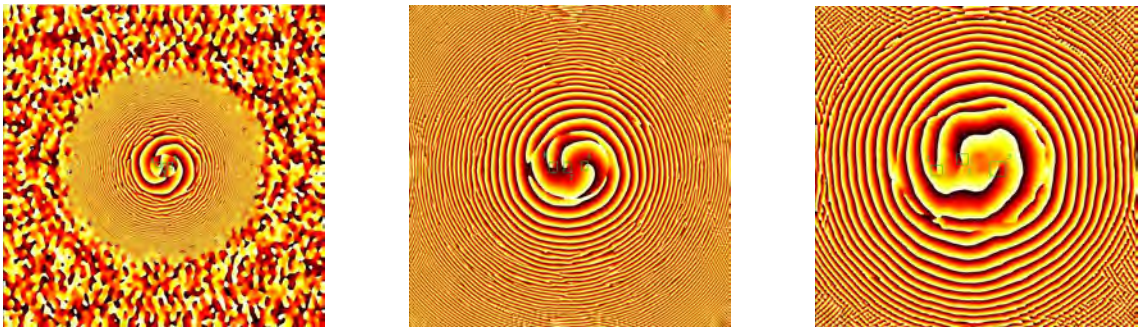

(a) 500 m (b) 2000 m (c) 4000 m

Figure 4.3: Retention of characteristic phase discontinuation of $HIG^2_{5,3}$ beam at different distances. The relative position of each phase discontinuation changes due to the turbulence effects but the vortexes remain in the beam profile picture, even if they are not distinguishable in the intensity profile.

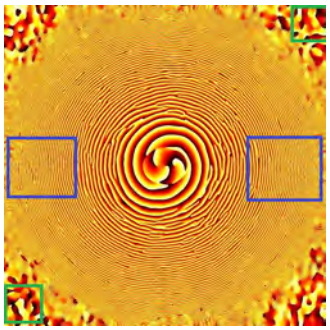

Figure 4.4: Random phase regions on the beam propagated $1000m$. In green are the regions resulting from the random propagation phase masks used, in blue the phase regions arising from the low intensity regions of the beam profile and the FFT method.

masks applied to the whole beam matrix and not just the matrix region where the mode is visibly at. At the same time, symmetric-esque phase regions outside the main beam phase profile can be identified and are a result of the FFT method used to get the phase. These regions in the phase profiles are signalized in Figure 4.4.

In any case, a better understating on the sturdiness of the mode can be achieved by getting the measurements of SR, σ^2 and OV described in section **2.4** as a function of propagation distance. These are shown in Figure 4.5.

It can be seen from Figure 4.5 that, as expected, for longer distances the measurements of overlap, scintillation index and strehl ratio were gradually getting worse. The most notable of these results was the overlap value for the mode dropping to near 29% after $4000m$ of propagation, meaning that around 71% of the mode *leaked* into other modes. Even for distances below $2500m$ this leakage of intensity from the original mode is

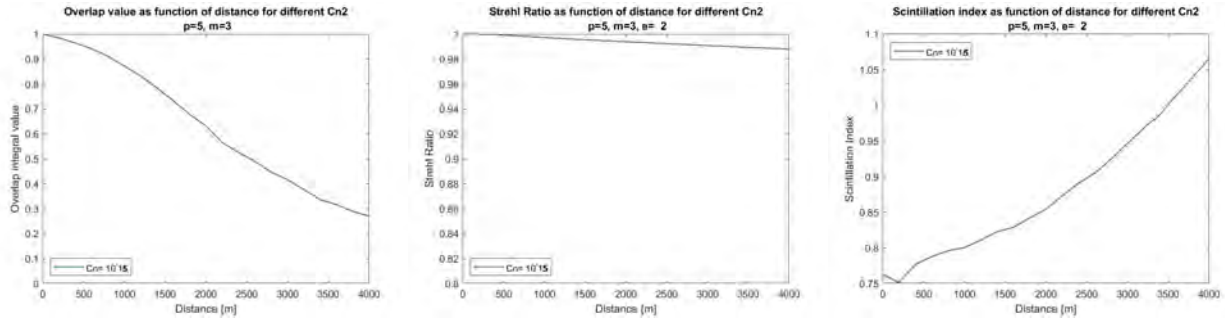

(a) Overlap value (b) Strehl Ratio (c) Scintillation index

Figure 4.5: Propagation characterization of $HIG^2_{5,3}$ mode with $C_n^2 = 10^{-15}m^{2/3}$.

above 50% of the intensity. In the case of the scintillation index there is a clear increase in its value with the distance, showing clearly that due to turbulece effects, the propagated profile becomes less coherent. Finally, the Strehl Ratio decays significantly more slowly than the other parameter, not dropping below 0.98 for the whole $4000m$ propagation, which means that almost all of the intensity of the beam remains in the same region as the beam propagated with no turbulence.

A lot information about propagated beam can be obtained from these measurements. The overlap value gives a clear parameter of how much of the intensity of the beam is kept in the selected initial mode. In a communication scheme this is equivalent to how much the information in a channel is kept while transmitting said information for a certain distance. The scintillation index, as the name indicates, shows how much the beam scintillates (varies in local intensity) and thus can be understood as a measure of the beam intensity stability. Finally, the strehl ratio defines how much of the total power of the beam is *deviated* from the original. In a communication system this could be translated to how much of the initial intensity is kept at the receivers end compared to the intensity with no turbulence effects. Higher values for the overlap and strehl ratio and lower scintillation index values are preferred.

4.2.2 Propagation of a single Helical Ince-Gaussian mode varying the turbulence strength

Although the simulation of propagation of a HIG beam was sucessfully performed, the main objective of this work was to investigate how different parameters affect the propagation performance of HIG modes. The first of these parameters to be studied was the turbulence strength, characterized by the refractive index structure parameter C_n^2. In order to do so, the propagation of a $HIG^2_{5,3}$ mode shown in Figure 4.2 was performed for three values of C_n^2: $C_n^2 = 10^{-14}m^{2/3}$ (strong turbulence), $C_n^2 = 10^{-15}m^{2/3}$ (medium turbulence) and $C_n^2 = 10^{-16}m^{2/3}$ (weak turbulence). The propagation of the modes was performed over a distance of $2000m$,

following the same algorithm explained before and having this distance as the standard for several propagations due to computation time and the chosen size of the window. The results of the propagation simulation are shown graphically in Tables 4.1, 4.2 and 4.3, each of which has the propagation of the same beam for a different value of the refractive index structure parameter which represent low, medium and strong turbulence regimes. As the mode without turbulence is known to be structurally stable, the transverse profiles of the mode without turbulence profiles will no longer be shown and only the initial beam of Figure 4.2 will be kept as a reference.

The effect of the value of the refractive index structure constant is critical in the sturdiness of the intensity profile of the initial beam, as can be seen from Tables 4.1-4.3. While the apparent effects on the intensity profile for the weak turbulence case are barely noticeable to the eye, even at 2km, the distortion of the transverse profile is evident for medium turbulence and very apparent for the strong one that loses great part of its structure at around 1500 meters of propagation, where the characteristic zero-intensity points are barely recognizable. This seems to be the case as well for the phase profile, with the exception that the phase discontinuities are still kept in their totality, just heavily moved away from their initial relative position inside the beam. This result is important, as it exemplifies that even for strong turbulence the vortex nature of the helical beam, and thus at least part of the OAM of the original beam is kept. To exactly see what the effects of the turbulence strength on the nature of the mode were, the sturdiness parameters of the beam were calculated and are shown in Figure 4.6, where the characterization parameters results for the propagation a $HIG^2_{5,3}$ in different turbulence parameters are shown.

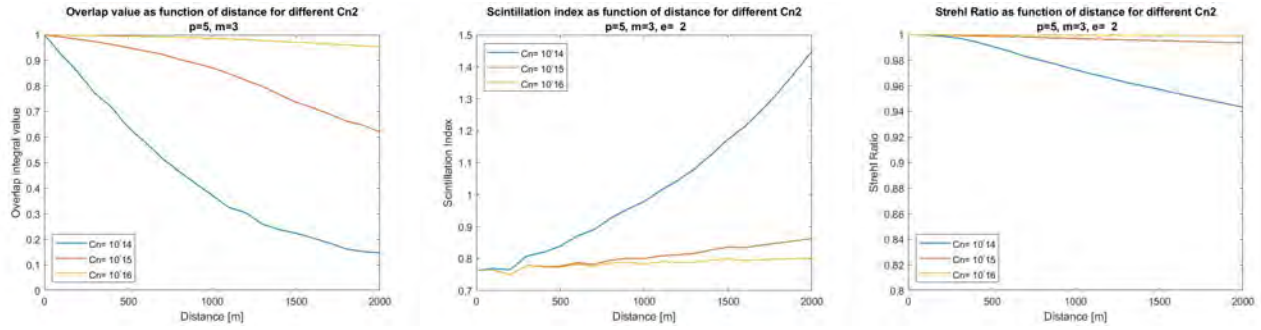

(a) Overlap value (b) Scintillation index (c) Strehl Ratio

Figure 4.6: Propagation characterization of $HIG^2_{5,3}$ mode with varying turbulence strength.

As expected from the intensity profiles, the turbulence strength seems to play a determining role in the sturdiness of the beam, more importantly in the leakage of modes. This is more noticeable for strong turbulence even for short distances because for long distances, like 2km only 20% of the original beam structure was kept. This effect is important but not at the same degree with medium turbulence, while for weak one,

it seems that the beam can propagate through a much more significant distance without losing too much information. As for the scintillation index, the increase for strong turbulence is much worse than the other cases, which can be explained by the fact that the intensity transverse profile is strongly distorted, and thus not as structurally stable as in the beginning. A similar case happens with the Strehl Ratio, because for a stronger turbulence, the bigger the angle in which the beam can be partially deflected, thus making more probable the leaking of power from the measurement window. Although even for strong turbulence and long distance, the intensity at the receptor plane does not drop to less than 90%. This can be attributed to the fact that a paraxial propagation is considered and that the size of the beam *as such* is not as heavily affected by the turbulence due to the nature of propagation of Gaussian beams.

As the effects of turbulence were measured and described, it was a good idea to assess the effects of the *nature* of the beam itself, meaning the choose of mode numbers on the beam. As a first approximation and following the tendency of the work to look into this parameter, the effects on the variation of the ellipticity value of a beam were studied under atmospheric turbulence effects.

4.2.3 Propagation of Helical Ince-Gaussian modes varying the ellipticity parameter

For the variation on the ellipticity parameter of HIG modes through atmosphere, the chosen mode to propagate was the $HIG_{5,3}$, as the evolution of the transverse intensity and phase profile patterns with the change of ellipticity parameter was already studied both theoretically in **section 2.3** and experimentally in **section 3.4.1**. For the propagation of these modes, a refractive index structure parameter of $C_n^2 = 10^{-15} m^{2/3}$ was used in the $2km$ propagation and the ellipticity parameter values were chosen so that a change of the beam from HLG to HHG modes could be seen. Due to quantity of beam profiles that were handled in this simulation (as in future ones) only the initial intensity and phase profiles are shown for each mode involved, as well of an intermediate and a final distance point intensity and phase profile for each mode. This modes are shown in Table 4.4 and 4.5.

The different intensity and phase profiles on the aforementioned tables exhibit similar characteristics to those found for the propagation of a single mode in **section 4.2.1**, from distortion of the intensity profiles to the movement of the phase discontinuities in the phase profiles. Because of this, much better information of these beams was obtained by the comparison of the propagation measurements, which is presented in Figure 4.7. In particular and beginning from this point of the work, the overlap value of the modes is presented in the form of tables (with some exceptions for the sake of not being redundant), for better reading of the results obtained in this regard. For the case of the aforementioned mode, these results are shown in Table 4.6. This is done only for the overlap values due to it being the most important characterization measurement regarding the performance of modes as information carriers.

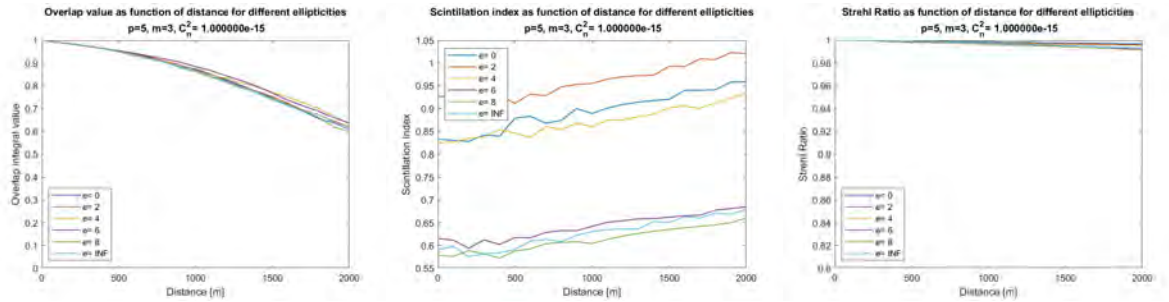

(a) Overlap value (b) Scintillation index (c) Strehl Ratio

Figure 4.7: Propagation characterization of several $HIG_{5,3}$ modes with varying ellipticity values at $C_n^2 = 10^{-15}m^{-2/3}$.

The ellipticity parameter seems to have heavy impact in the scintillation index of the modes, with certain ellipticity values having a considerably bigger value than others. This is due to the geometrical structure nature of the measurement, that takes into account the intensity mean values for all points of the mode. By having a mode in which the intensity of the beam is mainly concentrated at a certain region of the transverse profile, as happens for $HIG_{5,3}$ with low ellipticity, the difference in intensity between the outer parts of the mode and the inner parts, that are almost zero, make the scintillation index much bigger. In contrast, higher values on the ellipticity make the intensity of the beam to be more evenly distributed, and thus, seem to help diminish the scintillation index value. As for the Strehl ratio value, the ellipticity of the beam seems to have a very subtle effect that is not very appreciable with a $C_n^2 = 10^{-15}m^{-2/3}$ refractive index structure parameter. As was seen before, the Strehl ratio of these beams is more heavily affected by the strength of the turbulence, rather than the nature of the beam itself.

However, the most important result of this simulation relates to the fact that the overlap of the modes as a function of distance is almost the same for all values of ellipticity at all distances, with no particular preference for a value of this parameter that would make the beam profile more resilient to mode leakage by turbulence effects. This result would mean that for a certain mode, defined by the order p and degree m, any family of modes that is chosen to propagate this mode through the atmosphere would have around, if not the same effectiveness. In other words, **the robustness of a beam through the atmosphere can be consider to be very little dependent on the chosen symmetry or family of modes chosen to propagate it**. In order to corroborate this result, more simulations were made. First, the same selected ellipticity modes (minus $\varepsilon = 8$, for computation time) were propagated through weak and strong turbulence and a comparison of the measurement of the overlap value for these conditions is presented in Figure 4.8. As well, a $HIG_{8,2}$ propagation simulation for varying ellipticities was performed, to see if the observed characteristics of the propagated beams with the ellipticity are consistent for other sub-basis of modes. The

results of these propagations are shown in Table 4.7, Figure 4.9 and Table 4.8.

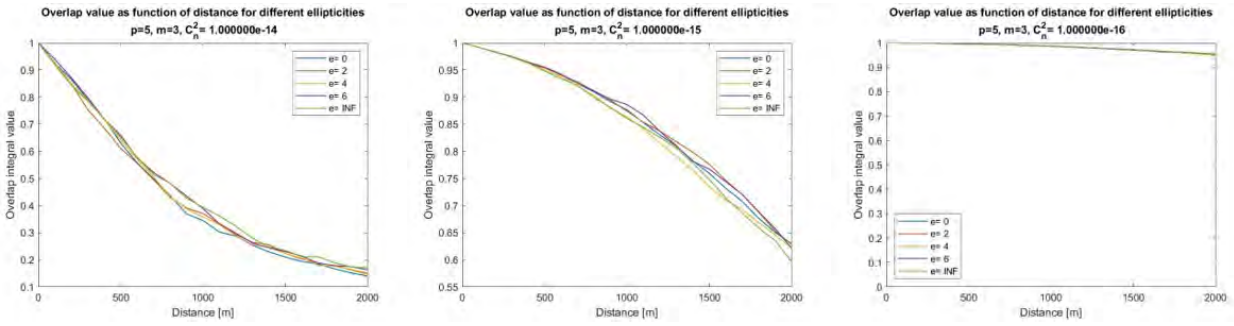

(a) Overlap for strong turbulence (b) Overlap for medium turbulence (c) Overlap for weak turbulence

Figure 4.8: Comparison of overlap value obtained for $HIG_{5,3}$ modes with varying ellipticity for different turbulence strength

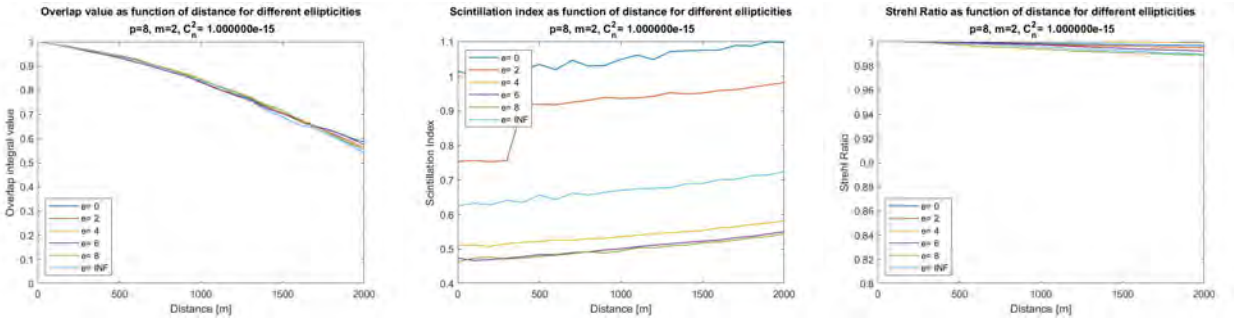

(a) Overlap value (b) Scintillation index (c) Strehl Ratio

Figure 4.9: Propagation characterization several $HIG_{8,2}$ with varying ellipticity values at $C_n^2 = 10^{-15}m^{-2/3}$

The results from Figures 4.8 and 4.9 as well of Table 4.7 and 4.8 show that the general characteristics of the beam propagation discussed for $HIG_{5,3}$ for varying ellipticities hold for both different turbulence strengths and different modes. In particular, the relation of the overlap value of the propagated beam with its ellipticity holds for all cases, which raises the question: What is it, if not the family or symmetry of the mode, that influences the performance of helical OAM-carrying beams?

As a first approximation to this question, the propagation of the well studied HLG mode was performed, as is seen in the next section.

4.2.4 Propagation of Helical Laguerre-Gaussian modes

A comparison on the propagation of different HLG with varying topological charges was performed. The chose on this specific family of modes was made because these are the more broadly studied vortex beams, due to their mathematical and geometrical relative simplicity, and to the fact that because of their azimuthal symmetry, they have a topological charge per photon of $2\pi l$, where l is the azimuthal index of the mode. Studies have been made that the topological charge of these beams (meaning the azimuthal mode) directly affects their performance in turbulent media [55]. As it is known from **section 2.3**, the topological charge of these beams and the radial mode are directly linked to the order and degree of a IG modes when $\varepsilon = 0$ and because of that the results of the simulation of these particular *integer* OAM beams could give insight on the parameters of HIG beam that affect their performance through turbulent media.

The simulation of these modes was made for the geometrically simpler cases, with radial index $n = 0$ and varying l values, which resulted in single ring-like beam profiles with size increasing with the value of the azimuthal number. The propagation of these transverse profile was made for a value of $C_n^2 = 10^{-14}m^{-2/3}$, in order to see more clearly the differences on the performance of the modes caused by the turbulence effects. The results of this procedure are shown in Table 4.9, with the initial and final intensity and phase profiles of each mode, and in Figure 4.10 and Table 4.10, where the results for the distinctive measurements of turbulent propagation are presented.

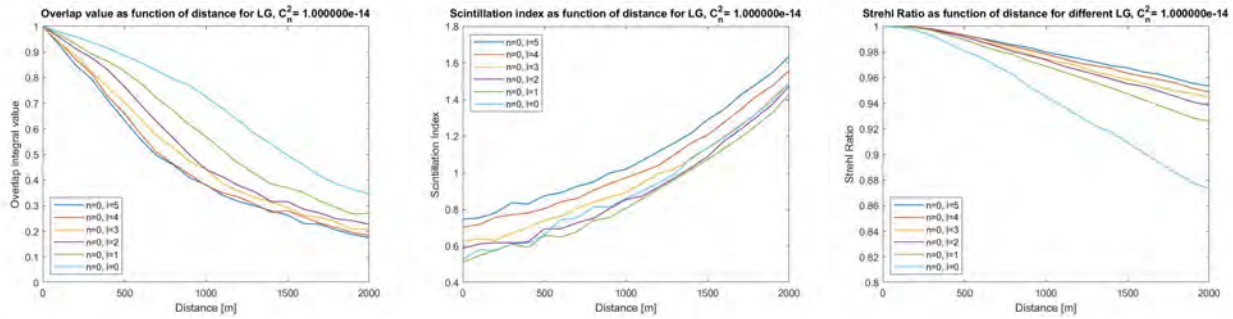

(a) Overlap value (b) Scintillation index (c) Strehl Ratio

Figure 4.10: Propagation characterization of several $HLG_{0,l}$ with varying l at $C_n^2 = 10^{-14}m^{-2/3}$.

In the case of the Laguerre-Gaussian modes, the scintillation index and the strehl ratio are more dependent on the actual size of the beam. For the scintillation index, it seems to have better values for lower values of OAM, even thought all of the modes have the same tendency. The Strehl ratio is actually more strongly impacted by the size and shape of the beams, with better results for higher l modes, a situation that can be comprehended because of the larger transverse area that higher l modes fill compared to lower modes, especially Gaussian modes, that are physically smaller, and as such, a smaller window for the measurement

means that is more probable for some of the intensity to go out of the measurement window, especially for high turbulence. However and more importantly, the effect on the overlap of the modes with the OAM of the beam shows that with a lower l value, modes become much more resilient to turbulence effects. This can be explained using the *complexity* of the beam structure and in particular, the phase structure of the beam. A regular Gaussian beam does not have a phase indetermination (and thus no OAM), so when propagating through the atmosphere there is not a rigorous spatial phase structure to be maintained. Meanwhile, as can be seen from Table 4.9, for higher l values like 5, the in-propagation axis initial $2\pi l$ phase indetermination is split into individual 2π indeterminations because of the effects of the random phase screens. Losing this spatial phase structure, that is more complex for higher l, can be seen as the leakage of these modes into other ones, losing some of the overlap value. The splitting of the axis phase indetermination for HLG is exemplified in Figure 4.11.

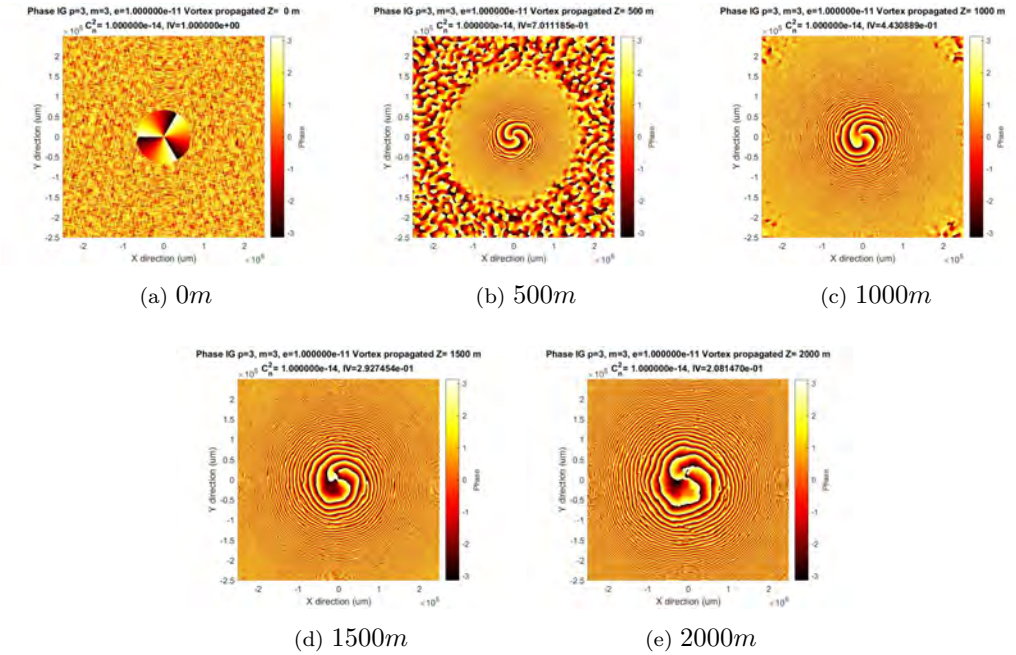

(a) $0m$ (b) $500m$ (c) $1000m$

(d) $1500m$ (e) $2000m$

Figure 4.11: Splitting of central phase in determination of $HLG_{0,3}$ mode at varying distances of propagation for $C_n^2 = 10^{-14}m^{-2/3}$.

As showcased in Figure 4.11, the initial OAM vortex in a HLG mode as it propagates through the atmosphere begins to split into individual 2π phase vortexes, that while at small distances of propagation are easily identified, for longer distances not as well, due to the effects of turbulence. As a matter of fact, one could think that instead of the axis vortex *splitting* into individual ones, the individual vortexes are at the beginning *overlapping* and they individually move away from the axis due to the turbulence effects, changing the overall structure of the vortex beam by doing so.

Now, having checked that indeed, the OAM of HLG modes influences their robustness in turbulence propagation, a relation of this OAM value for these modes can be made to the order p and degree m of HIG modes, as OAM is heavily dependent on these to indexes as seen before. Because of this, the effects of the change in this to parameters on the robustness of Helical beams is studied in the next two subsections.

4.2.5 Propagation of Helical Ince-Gaussian modes, varying the degree m parameter

The next propagation simulation to be done involved the the performance of the beam depending on the degree parameter m for HIG modes, recalling that this parameter is closely related to the OAM of helical beams, specially when the ellipticity of the mode is $\varepsilon = 0$, where the $HIG^0_{p,m}$ transforms into a $HLG_{n,l}$ mode with $l = m$ and $OAM = l\hbar$ per photon. The change in the value of the azimuthal number l was studied in the previous section, showing that lower values of l behave better in turbulence. A similar behaviour is thus expected for the elliptical azimuthal number m of HIG modes with $\varepsilon \neq 0$. The simulation performed in this section involved HIG modes with fixed order $p = 5$ and a turbulence strength of $C_n^2 = 10^{-14}m^{-2/3}$ was implemented in the propagation. The results for the transverse intensity and phase profiles of the propagated beams are present in Table 4.11, while the results on the characterization of the propagation are showed in Figure 4.12 and Table 4.12.

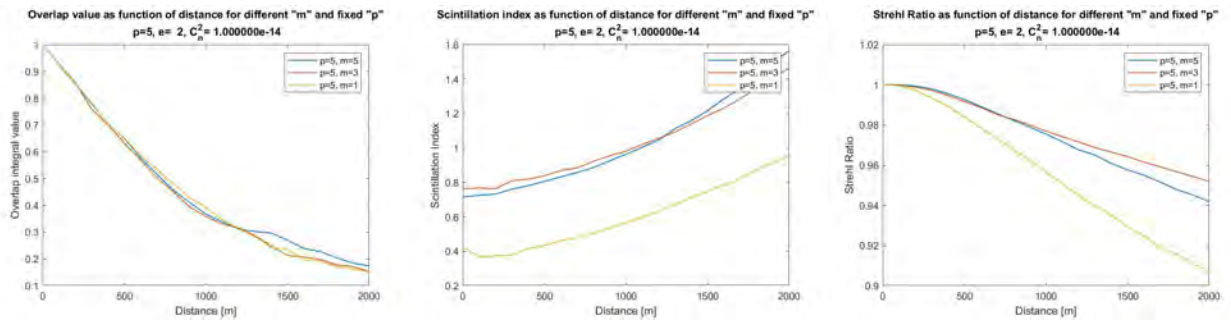

(a) Overlap value (b) Scintillation index (c) Strehl Ratio

Figure 4.12: Propagation characterization of several $HIG^2_{5,m}$ with at $C_n^2 = 10^{-14}m^{-2/3}$ by varying the degree of the mode.

The remarks that could be done regarding the phase and intensity transverse profiles of the propagated beams are very similar to the ones already explored in previous sections. However, is in the characterization measurements of the beam were the important results appear. As for the the scintillation index and the strehl ratio of the beams, while there were already defined as mode-geometry dependent measurements, it is interesting to note that at some points of the propagation the preferred m changes, but in general higher

values of m behave better. This could be explained by noticing that lower values of m, or rather, bigger differences in $p - m$ generate more elongated modes than those with lower $p - m$ value, as such, the window in which these quantities are initially checked is more elongated in the x (or y) axis and the turbulence effects on the beams tend to distort it and deviate beam intensity from the measurement window. Regarding the overlap value, it can be seen that for longer propagations the turbulence strength has a bigger effect on the leakage of power into other modes from the initial beam, the bigger values of m performed better, which is contrary to the initial assumption on the performance of the beam with the m parameter. Because of this, it is congruent to assume that not only the m parameter, but the order p parameter takes part in the effectiveness of these beams. Therefore, the variation of this mode parameter was investigated in the next section.

4.2.6 Propagation of Helical Ince-Gaussian modes, varying the order parameter

In this section, the effects of the order p parameter on HIG beams are studied in order to, in conjunction with the results obtained from varying the degree m parameter, obtain information about how the physical structure of the HIG beams affects their performance in turbulent media. The simulation of propagation was done for $HIG^2_{p,3}$ mode with a refractive index structure constant of $C_n^2 = 10^{-14}m^{-2/3}$. The results of the simulation are shown in Table 4.13, for the intensity and phase transverse profiles and in Figure 4.13 and Table 4.14 for the characterization of the propagations.

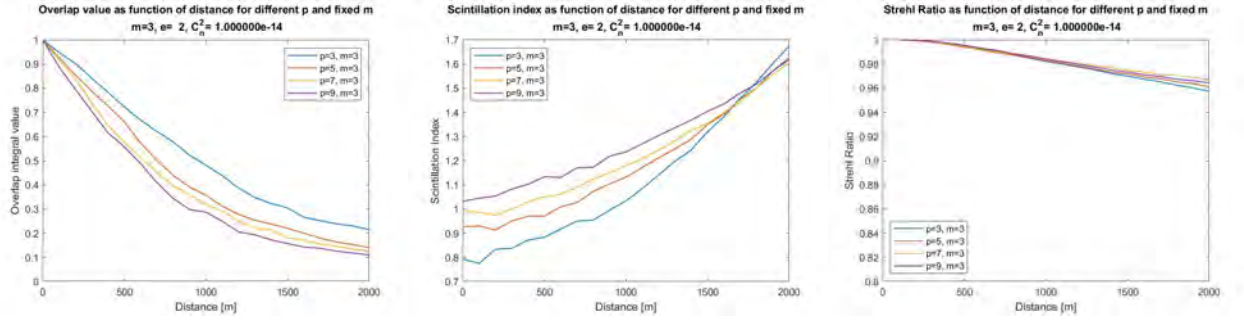

(a) Overlap value (b) Scintillation index (c) Strehl Ratio

Figure 4.13: Propagation characterization of several $HIG^2_{p,3}$ with at $C_n^2 = 10^{-14}m^{-2/3}$ by varying the order of the mode.

A similar result to the one obtained for propagation of modes with a fixed m parameter is obtained, since both the scintillation index and strehl ratio have a strong dependency on the geometry of the initial transverse beam profile. In the cases of the modes used, a smaller p value is preferred for the scintillation index up to a certain distance, where most of the modes seem to converge to a very similar value except for the lower $p = 3$ mode. As for the Strehl Ratio, there is no clear mode with radically better performance.

This can be then attributed to the geometrical form of the modes, that as seen in Table 4.13 is not that elongated in any mode. As a general rule then, a bigger impact on these two measurements (and thus to the transverse geometry) can be attributed to the degree m of a mode, rather than to the order p.

However, for the overlap measurement, there is a clear preference in performance for lower p modes, that is even more marked than the preference for higher values of m, having the $HIG^2_{3,3}$ around double the overlap value compared to the worst performing mode $HIG^2_{9,3}$.

Having the results for the overlap for both fixed p and m parameters a remarkable condition can be defined. Rather than just looking at these values separately, one could look at the results for modes with different $p - m$. In both Figures 4.12 and 4.13, the modes with an smaller difference between these two values perform better than the others. To make a better understanding of this result one could look at the relation of this parameter with the radial parameter n in HLG modes, where $n = (p - m)/2$, so that for the increase of the radial mode, the worst that the performance is of the beam in turbulence, or at any ellipticity, it could be seen as the number of phase regions defined by the beam, as discussed in **section 2.3**. Another way to see this result would be that, as the p value has more impact on the robustness of the mode than m, and p, represents a family of modes that share the same Gouy phase and form a complete sub-basis of orthogonal modes , as seen in **section 2.2**, lower p modes perform better, as there are less modes within the same sub-basis of orthogonal modes in which the mode can leak to, with the different possible values of m being the most probable modes to leak to. However, there is also leakage into other modes due to loss of coherence.

4.3 General results on propagation of Helical Ince-Gauss beams

The results reported in this work show several remarkable properties regarding helical modes propagating through turbulent media. First, there was special attention put into the effects that the turbulence has into the modes, showing that the performance of all modes is highly dependent with the strength of the turbulence, however, for modes that propagate in normal turbulence conditions (around $C_n^2 = 10^{-15} m^{-2/3}$) the losses on intensity and structure are low, while the leakage of modes is not very critical. Also, the effects the phase vortexes, the actual carriers of OAM on these beams, were shown to move around their initial relative position inside the beam in an amount and randomness according to the strength of turbulence, showing that the turbulence can change, to a certain degree, the average value of the mode OAM.

Remarkable is the shown property that the ellipticity parameter of the modes themselves ε does not strongly impact the overlap performance of the modes, and rather is the combination of order p and degree

m and their difference $p - m$ the parameters that do. This could be explained due to the fact that p and m define the complexity of a mode and the ε defines the basis in which the mode is projected, each basis having its own symmetry. Also, p in particular defines a sub-family of coherent modes with different Gouy phase. This means that in a free space optical communication system whatever chosen basis (ellipticity) to put a mode into, the mode will keep the information with barely the same fidelity, at least without considering a particular measurement system and for the used turbulence model, as other studies, with different parameters give differing results [56–58]. These discordance is discussed in the general conclusions. The overlap value can be as well optimized with the correct p and m values depending on the system. All of p, m, ε had an impact on the scintillation index and strehl ratio measurements, by giving the beam its geometrical shape and axial symmetry, with less *elongated* modes being preferred. Although the way in which these two parameters were measured in this work was by taking the original beam without propagation as basis for the detection window, in an actual free space communication system these measurements are heavily dependent on the characteristics of the receivers end.

However, the results obtained show the nature of the beam profile itself and thus could be used as a reference when designing a specific free space communication system based on OAM carrying beams.

Distance	Mode without turbulence	Mode with turbulence	Phase profile
500 m	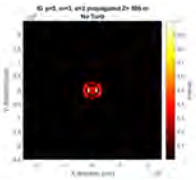	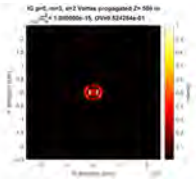	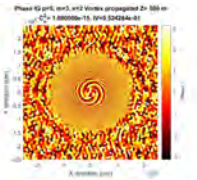
1000 m	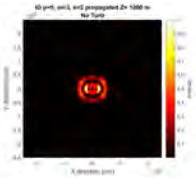	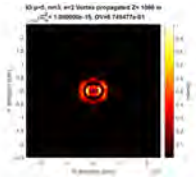	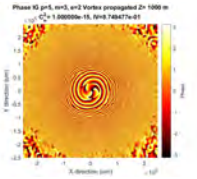
1500 m	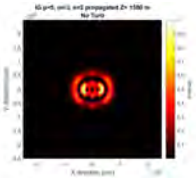	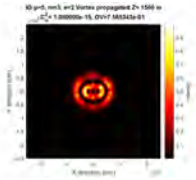	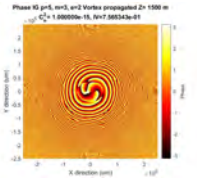
2000 m	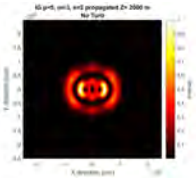	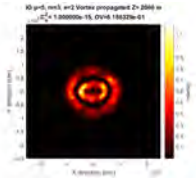	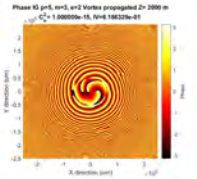
2500 m	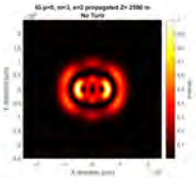	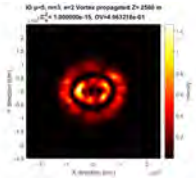	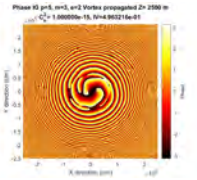
3000 m	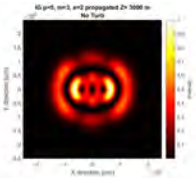	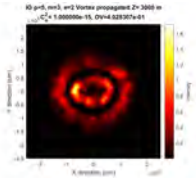	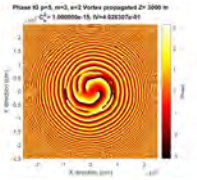
3500 m	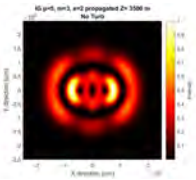	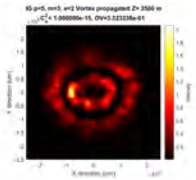	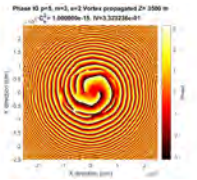
4000 m	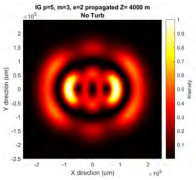	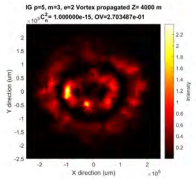	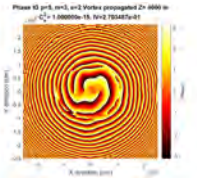

Table 4.1: Propagation of a $HIG^2_{5,2}$ mode through 4km. of turbulent atmosphere with $C_n^2 = 10^{-15} m^{2/3}$ (medium turbulence)

Distance	Mode with turbulence	Phase profile
300 m	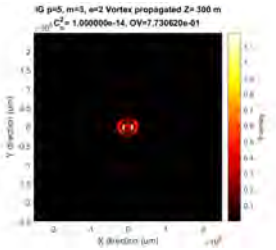	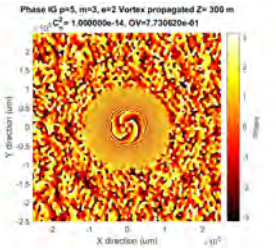
600 m	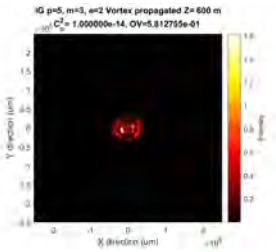	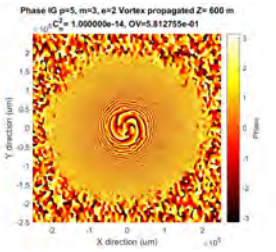
900 m	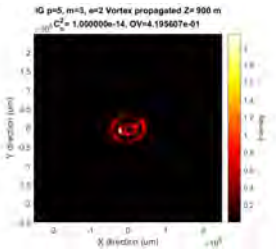	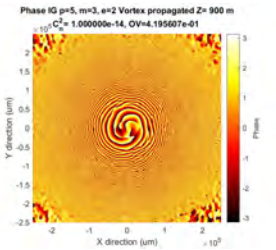
1200 m	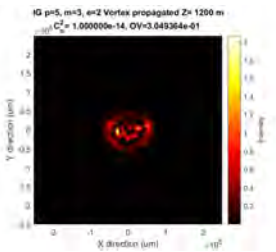	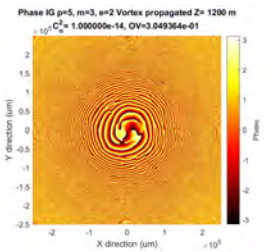
1500 m	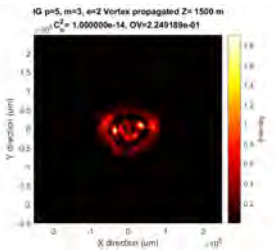	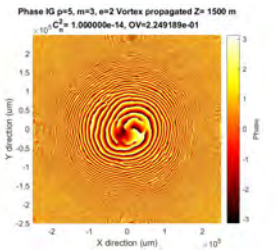
2000 m	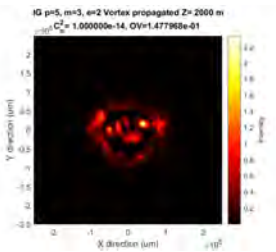	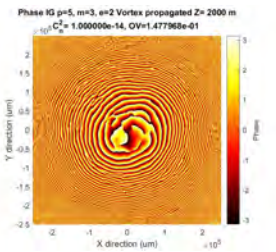

Table 4.2: Propagation of a $HIG^2_{5,3}$ mode through 4km. of turbulent atmosphere with $C_n^2 = 10^{-14}m^{2/3}$ (strong turbulence).

Distance	Mode with turbulence	Phase profile
300 m	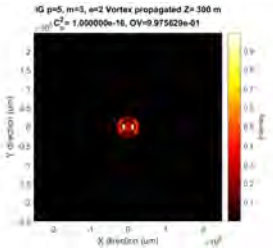	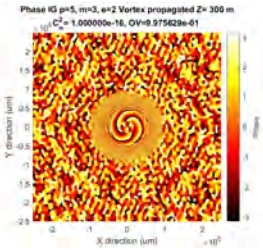
600 m	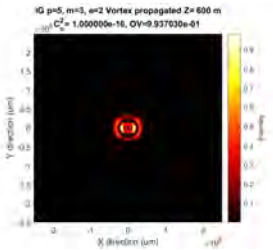	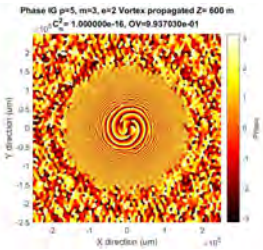
900 m	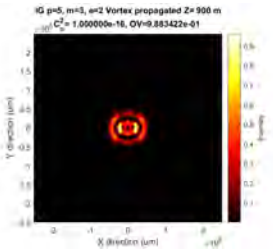	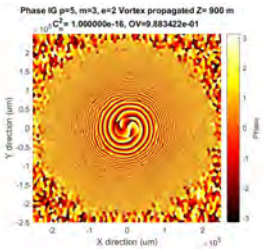
1200 m	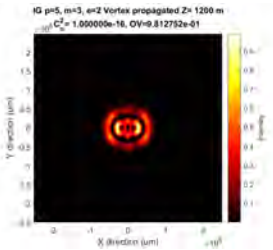	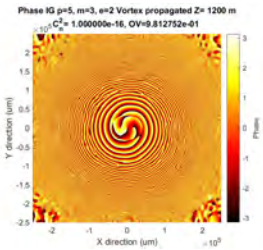
1500 m	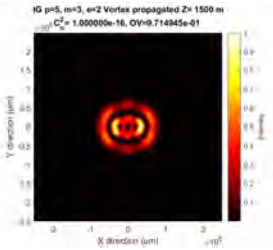	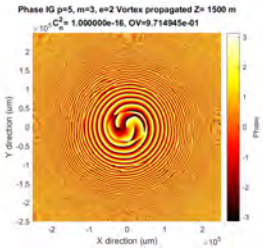
2000 m	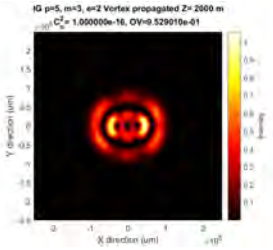	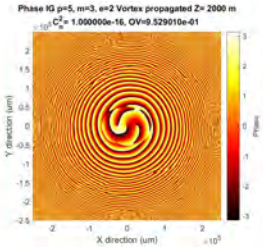

Table 4.3: Propagation of a $HIG^2_{5,3}$ mode through 4km. of turbulent atmosphere with $C_n^2 = 10^{-16}m^{2/3}$ (weak turbulence).

Ellipticity	Intensity at 0m	Intensity at 1000m	Intensity at 2000m
$\varepsilon = 0$	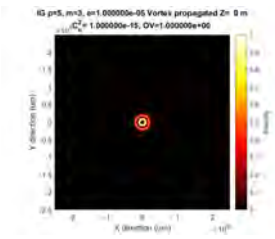	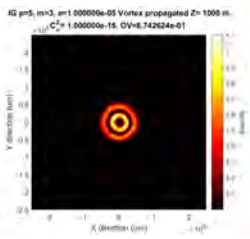	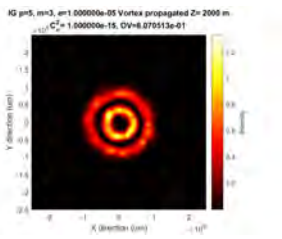
$\varepsilon = 2$	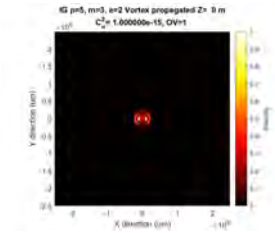	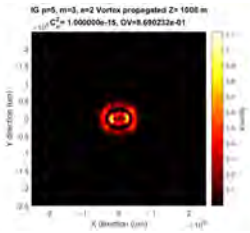	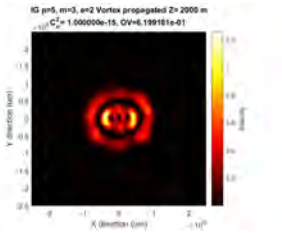
$\varepsilon = 4$	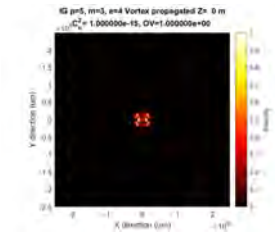	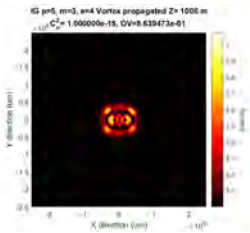	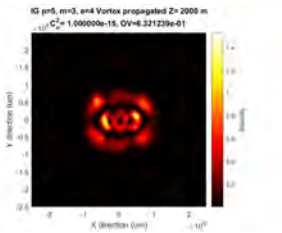
$\varepsilon = 6$	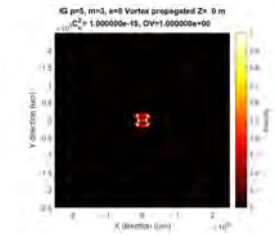	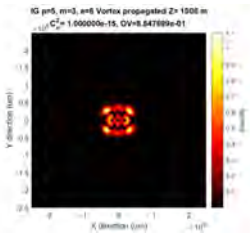	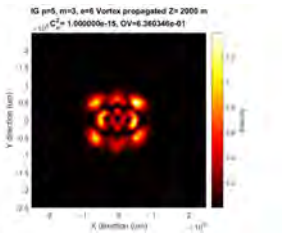
$\varepsilon = 8$	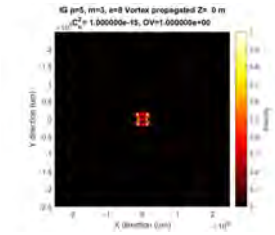	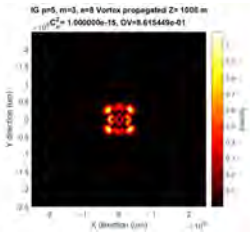	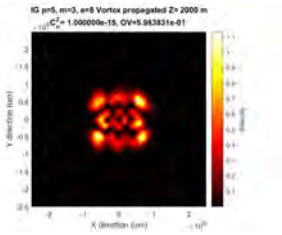
$\varepsilon = \infty$	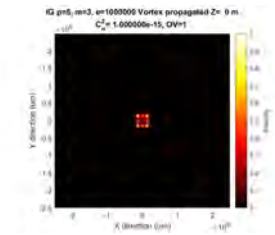	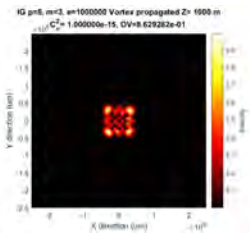	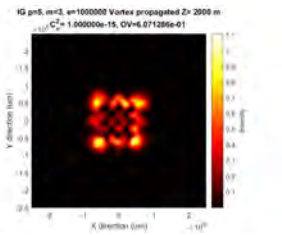

Table 4.4: Comparison of propagation of varying $HIG_{5,3}$ modes transverse intensity profile through 2km of turbulent atmosphere with $C_n^2 = 10^{-15} m^{2/3}$ and varying ellipticity value.

Ellipticity	Intensity at 0m	Intensity at 1000m	Intensity at 2000m
$\varepsilon = 0$	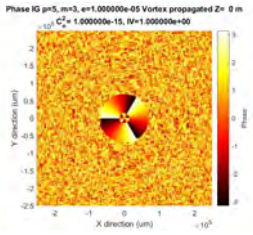	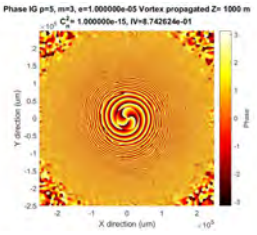	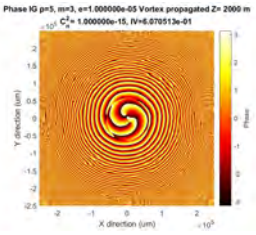
$\varepsilon = 2$	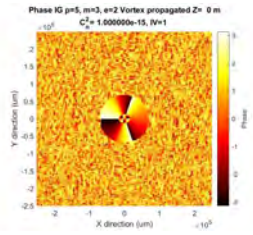	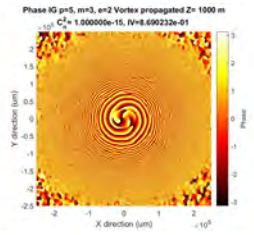	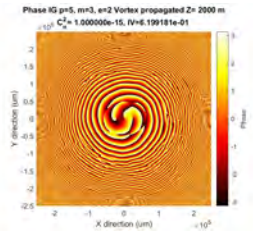
$\varepsilon = 4$	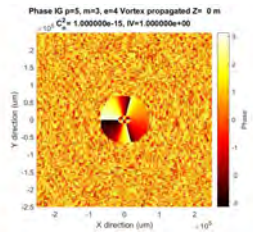	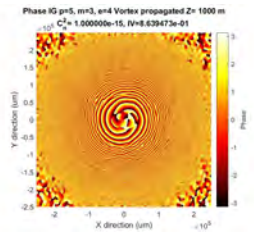	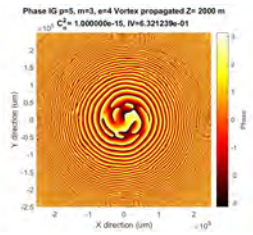
$\varepsilon = 6$	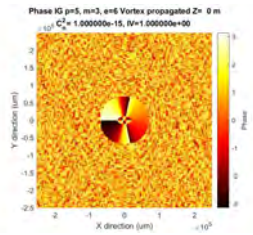	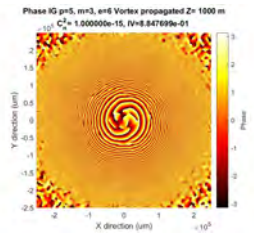	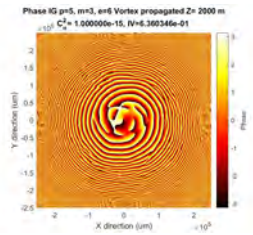
$\varepsilon = 8$	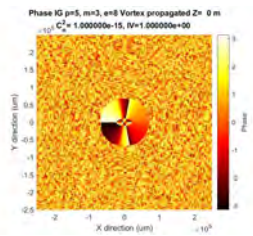	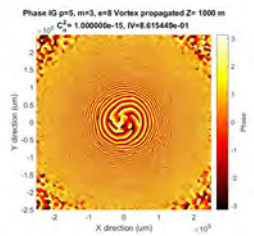	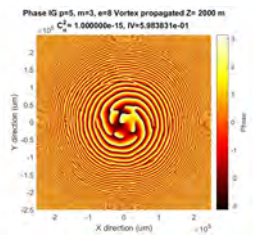
$\varepsilon = \infty$	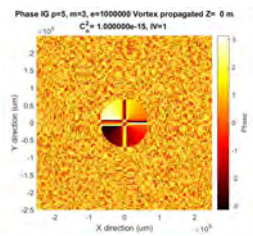	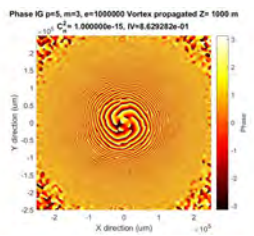	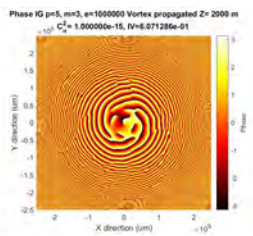

Table 4.5: Comparison of propagation of varying $HIG_{5,3}$ modes phase profile through 2km of turbulent atmosphere with $C_n^2 = 10^{-15} m^{2/3}$ and varying ellipticity value.

Distance (m)	$\varepsilon = 0$	$\varepsilon = 2$	$\varepsilon = 4$	$\varepsilon = 6$	$\varepsilon = 8$	$\varepsilon = \infty$
0	1	1	1	1	1	1
100	0.9919	0.991	0.9925	0.9914	0.9922	0.9932
200	0.9824	0.9824	0.9844	0.9833	0.983	0.9855
300	0.9727	0.9748	0.9753	0.9763	0.9734	0.9756
400	0.9635	0.9659	0.9635	0.9646	0.9637	0.965
500	0.9532	0.9535	0.9488	0.9546	0.9503	0.9509
600	0.9386	0.9399	0.9325	0.9438	0.9363	0.9377
700	0.9245	0.9268	0.9189	0.9306	0.922	0.9192
800	0.9068	0.9094	0.9078	0.9185	0.9047	0.9031
900	0.8859	0.8924	0.8861	0.9043	0.8792	0.8845
1000	0.8743	0.869	0.8639	0.8848	0.8615	0.8629
1100	0.8511	0.85	0.8478	0.8672	0.8385	0.8421
1200	0.8278	0.8231	0.8338	0.8436	0.8152	0.8194
1300	0.8014	0.7963	0.8121	0.8229	0.7903	0.7915
1400	0.7741	0.7759	0.7951	0.7975	0.7674	0.7671
1500	0.7469	0.7525	0.7725	0.7688	0.7441	0.7371
1600	0.7137	0.7238	0.7495	0.737	0.7192	0.7157
1700	0.6879	0.6928	0.7259	0.7113	0.6901	0.687
1800	0.6552	0.672	0.6999	0.6883	0.6602	0.6742
1900	0.6369	0.6445	0.6672	0.6595	0.6175	0.6406
2000	0.6071	0.6199	0.6321	0.636	0.5984	0.6071

Table 4.6: Results of overlap value for $HIG_{5,3}$ mode at varying propagation distances with $C_n^2 = 10^{-15} m^{-2/3}$ for varying ellipticity value.

Ellipticity	Initial Intensity	Final Intensity	Initial Phase	Final Phase
$\varepsilon = 0$	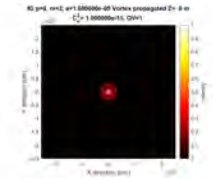	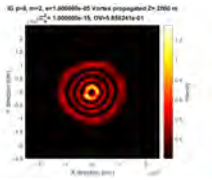	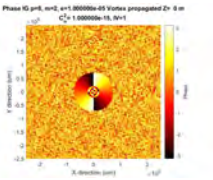	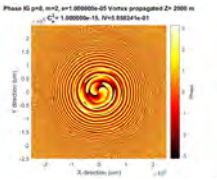
$\varepsilon = 2$	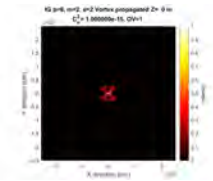	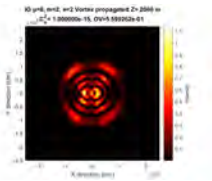	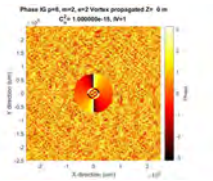	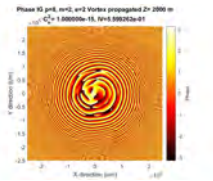
$\varepsilon = 4$	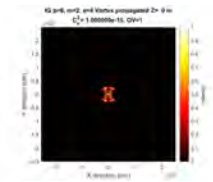	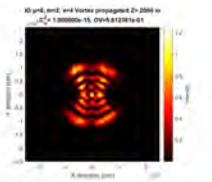	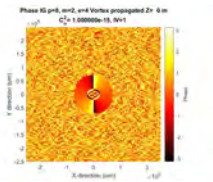	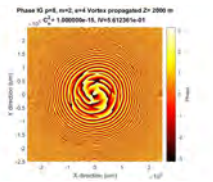
$\varepsilon = 6$	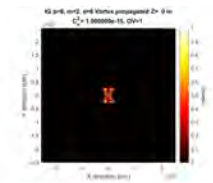	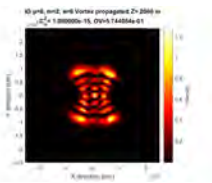	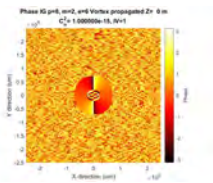	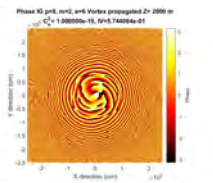
$\varepsilon = 8$	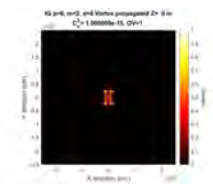	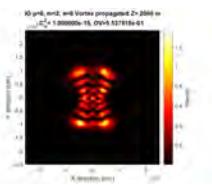	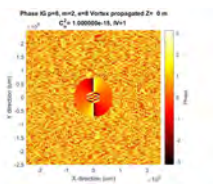	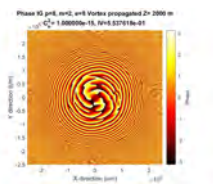
$\varepsilon = \infty$	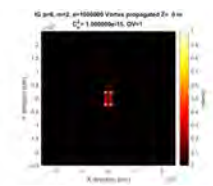	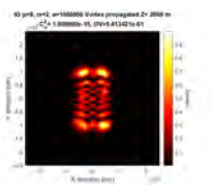	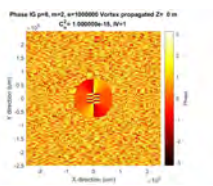	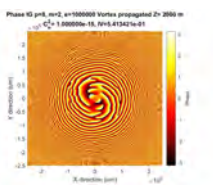

Table 4.7: Comparison of propagation of varying $HIG_{8,2}$ modes transverse intensity profile through 2km of turbulent atmosphere with $C_n^2 = 10^{-15} m^{-2/3}$ and varying ellipticity values.

Distance (m)	$\varepsilon = 0$	$\varepsilon = 2$	$\varepsilon = 4$	$\varepsilon = 6$	$\varepsilon = 8$	$\varepsilon = \infty$
0	1	1	1	1	1	1
100	0.9895	0.9901	0.9895	0.9896	0.9896	0.99
200	0.9785	0.98	0.979	0.9767	0.9778	0.9791
300	0.9663	0.9679	0.9681	0.9615	0.9652	0.9686
400	0.9546	0.9555	0.9533	0.9486	0.9551	0.957
500	0.9429	0.9403	0.9393	0.9339	0.9388	0.9417
600	0.9274	0.9294	0.9242	0.9153	0.9261	0.9224
700	0.9062	0.9066	0.9059	0.8994	0.9071	0.9053
800	0.8876	0.8841	0.8907	0.8771	0.8869	0.8842
900	0.8677	0.8631	0.8691	0.8588	0.8669	0.8602
1000	0.846	0.8312	0.8475	0.8337	0.8379	0.8398
1100	0.8153	0.8057	0.8158	0.8067	0.8186	0.8182
1200	0.795	0.7849	0.7934	0.7797	0.7963	0.7877
1300	0.764	0.7559	0.7722	0.7602	0.7677	0.7596
1400	0.7316	0.7351	0.7368	0.725	0.7409	0.7159
1500	0.7083	0.7059	0.706	0.7028	0.7163	0.6907
1600	0.6715	0.6803	0.6714	0.6758	0.6767	0.6563
1700	0.6514	0.6513	0.6405	0.6478	0.651	0.6413
1800	0.6323	0.6218	0.6129	0.6339	0.6185	0.6102
1900	0.6062	0.5943	0.5848	0.6066	0.5839	0.5787
2000	0.5858	0.5599	0.5612	0.5744	0.5538	0.5413

Table 4.8: Results of overlap value for $HIG_{8,2}$ mode at varying propagation distances with $C_n^2 = 10^{-15} m^{-2/3}$ for varying ellipticity values.

Mode	Initial Intensity	Final Intensity	Initial Phase	Final Phase
Gaussian beam	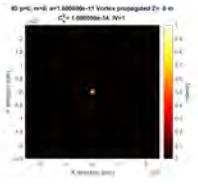	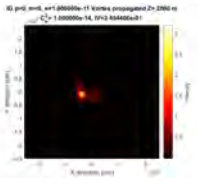	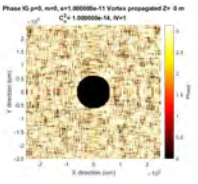	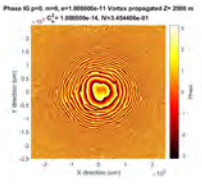
$HLG_{0,1}$	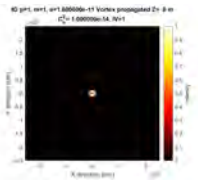	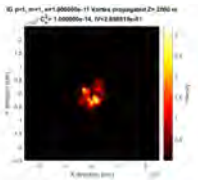	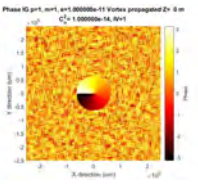	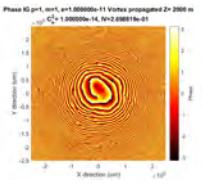
$HLG_{0,2}$	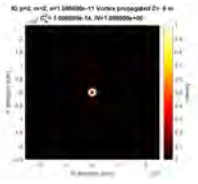	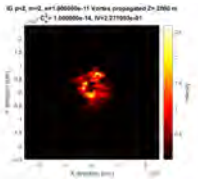	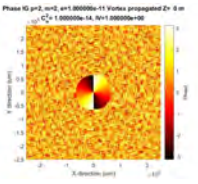	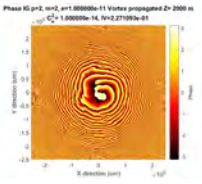
$HLG_{0,3}$	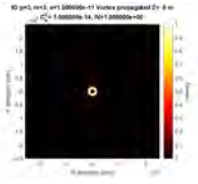	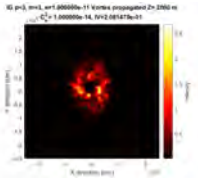	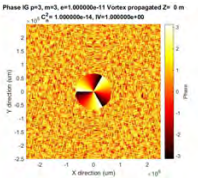	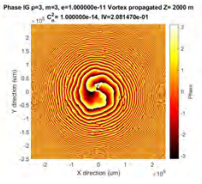
$HLG_{0,4}$	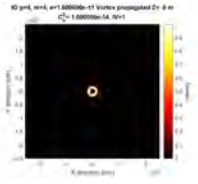	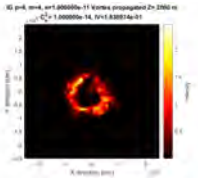	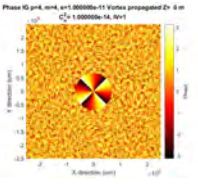	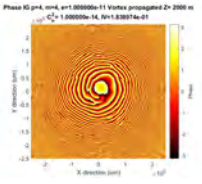
$HLG_{0,5}$	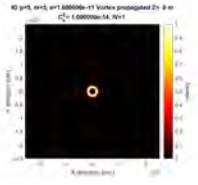	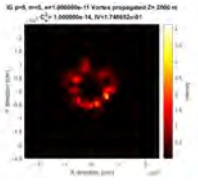	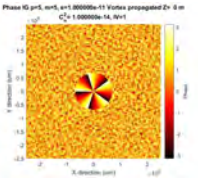	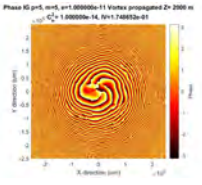

Table 4.9: Comparison of propagation of varying $HLG_{0,l}$ modes transverse intensity profile through 2km of turbulent atmosphere with $C_n^2 = 10^{-14} m^{-2/3}$.

Distance (m)	Gaussian Beam	$HLG_{0,1}$	$HLG_{0,2}$	$HLG_{0,3}$	$HLG_{0,4}$	$HLG_{0,5}$
0	1	1	1	1	1	1
100	0.9791	0.9684	0.9583	0.936	0.9384	0.9282
200	0.9604	0.9317	0.9137	0.8893	0.8733	0.8498
300	0.9371	0.8914	0.8769	0.8225	0.8151	0.7928
400	0.9154	0.8634	0.8291	0.761	0.7244	0.7107
500	0.8854	0.8256	0.765	0.7011	0.6608	0.6339
600	0.8588	0.7765	0.6942	0.6372	0.5799	0.5584
700	0.8271	0.72	0.6261	0.5717	0.5071	0.495
800	0.7958	0.6709	0.5633	0.5257	0.4625	0.4597
900	0.7702	0.6155	0.499	0.4734	0.4225	0.4093
1000	0.7248	0.5702	0.4419	0.4431	0.3791	0.3823
1100	0.6802	0.5176	0.4134	0.3885	0.351	0.3415
1200	0.6321	0.4659	0.379	0.3579	0.3333	0.3166
1300	0.5808	0.4243	0.3541	0.3319	0.307	0.2995
1400	0.5408	0.3846	0.3162	0.315	0.2743	0.2803
1500	0.4965	0.3706	0.3163	0.2927	0.2811	0.2638
1600	0.4601	0.351	0.2863	0.2622	0.2558	0.2306
1700	0.4156	0.3183	0.2718	0.2545	0.2319	0.2274
1800	0.3845	0.2927	0.2489	0.2363	0.2143	0.2049
1900	0.3648	0.2677	0.2417	0.2086	0.1951	0.1874
2000	0.3454	0.2699	0.2271	0.2081	0.1839	0.1749

Table 4.10: Results of overlap value for different $HLG_{0,l}$ modes at varying propagation distances with $C_n^2 = 10^{-14} m^{-2/3}$.

Mode	Initial Intensity	Final Intensity	Initial Phase	Final Phase
$HIG^2_{5,1}$	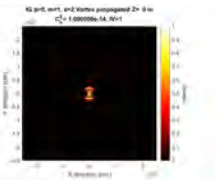	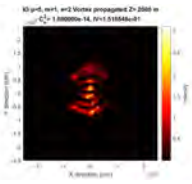	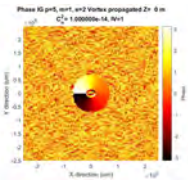	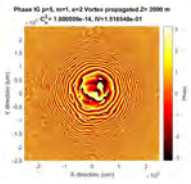
$HIG^2_{5,3}$	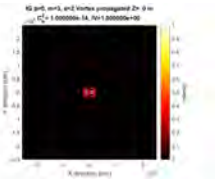	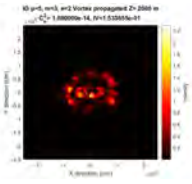	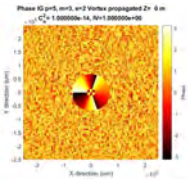	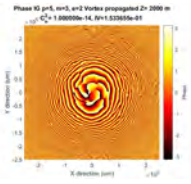
$HIG^2_{5,5}$	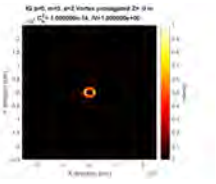	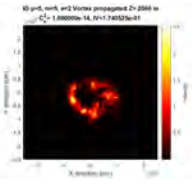	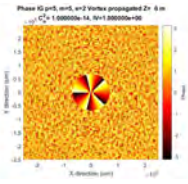	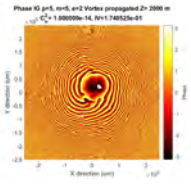

Table 4.11: Comparison of propagation of $HIG^2_{5,m}$ modes transverse intensity profile through 2km of turbulent atmosphere with $C_n^2 = 10^{-14}m^{-2/3}$ and varying degree m values.

Distance (m)	$HIG^2_{5,1}$	$HIG^2_{5,3}$	$HIG^2_{5,5}$
0	1	1	1
100	0.927	0.9281	0.9254
200	0.8564	0.8576	0.8532
300	0.7818	0.7582	0.7784
400	0.7048	0.7019	0.7058
500	0.6538	0.6322	0.6511
600	0.5828	0.5676	0.5747
700	0.5346	0.5024	0.5153
800	0.4807	0.4512	0.4572
900	0.4276	0.3935	0.411
1000	0.3929	0.3592	0.3676
1100	0.3458	0.3302	0.3388
1200	0.3144	0.3162	0.3115
1300	0.2833	0.2879	0.3023
1400	0.2446	0.2479	0.2973
1500	0.2356	0.2131	0.2697
1600	0.1962	0.2072	0.2391
1700	0.1921	0.1979	0.2276
1800	0.1714	0.1781	0.2045
1900	0.1628	0.1713	0.1851
2000	0.1517	0.1534	0.1741

Table 4.12: Results of overlap value for different $HIG^2_{5,m}$ modes at varying propagation distances with $C_n^2 = 10^{-14} m^{-2/3}$.

Mode	Initial Intensity	Final Intensity	Initial Phase	Final Phase
$HIG^2_{3,3}$	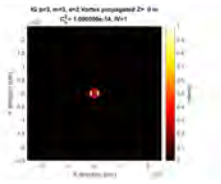	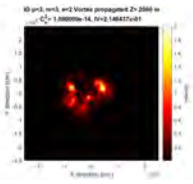	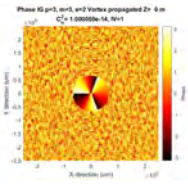	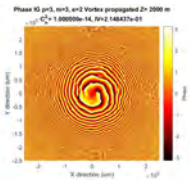
$HIG^2_{5,3}$	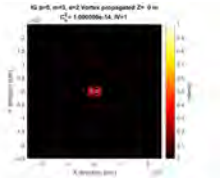	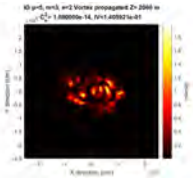	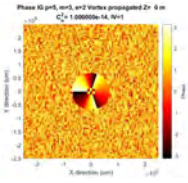	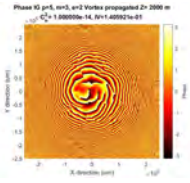
$HIG^2_{7,3}$	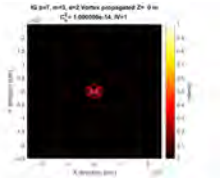	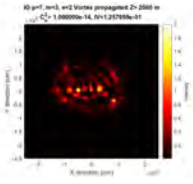	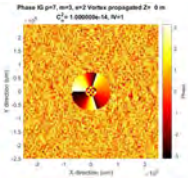	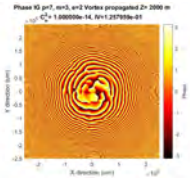
$HIG^2_{9,3}$	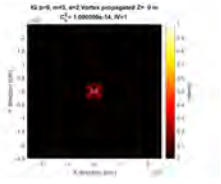	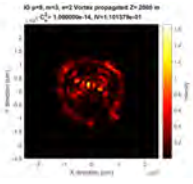	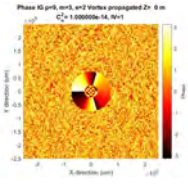	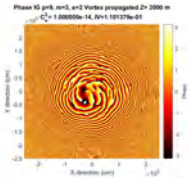

Table 4.13: Comparison of propagation of $HIG^2_{p,3}$ modes transverse intensity profile through 2km of turbulent atmosphere with $C_n^2 = 10^{-14} m^{-2/3}$ and varying order p values.

Distance (m)	$HIG^2_{3,3}$	$HIG^2_{5,3}$	$HIG^2_{7,3}$	$HIG^2_{9,3}$
0	1	1	1	1
100	0.9471	0.9265	0.9147	0.8869
200	0.9019	0.8547	0.8382	0.7953
300	0.841	0.7886	0.7401	0.7046
400	0.7827	0.7257	0.6449	0.6146
500	0.7225	0.6598	0.5777	0.558
600	0.6674	0.5724	0.5145	0.4868
700	0.6211	0.4992	0.4514	0.4094
800	0.5775	0.4388	0.3961	0.3434
900	0.5224	0.3914	0.3592	0.2978
1000	0.4817	0.3573	0.3195	0.2871
1100	0.4381	0.3121	0.2917	0.2497
1200	0.3872	0.278	0.2502	0.2056
1300	0.3479	0.2541	0.2215	0.1937
1400	0.3233	0.2383	0.2137	0.1722
1500	0.305	0.2201	0.1814	0.1577
1600	0.266	0.2007	0.1707	0.143
1700	0.2521	0.1801	0.1547	0.1378
1800	0.239	0.1638	0.1471	0.1264
1900	0.2305	0.1537	0.1343	0.1185
2000	0.2148	0.1406	0.1258	0.1101

Table 4.14: Results of overlap value for different $HIG^2_{p,3}$ modes at varying propagation distances with $C_n^2 = 10^{-14} m^{-2/3}$.

Chapter 5

Conclusions and future work

In this work, different and remarkable properties of orbital angular momentum carrying beams were explored both theoretically and experimentally, making big use of simulations in order to obtain a general perspective on the behavior of these beams while propagating through turbulent atmosphere.

The physical generation of orbital angular momentum beams using spatial light modulators was performed, proving the feasibility of these methods and also opening opportunities for the use of these generated intensity profiles in several applications. In particular, the possibility of using the generated vortex beams in the scheme of quantum optics are to be explored, as the tuning of them can be used to generate *ad hoc* states, for example, by projecting these modes into the pump or signal and idler beams in a Spontaneous Parametric Down Conversion crystal. This kind of procedure is then meant to be used for the generation of tunable bell states and to observe the evolution of a certain helical Ince-Gauss mode with the ellipticity parameter at the single photon count rate, using the OAM conservation property of the SPDC process. Also, the option of using the near-field intensity profile of helical Ince-Gauss modes for beam detection processes is proposed, as the optical vortexes of these beams seem to be more easily detected and characterized in these conditions.

As for the propagation of helical beams through the atmosphere, several properties of the beams in these conditions were observed and measured. The effects on the strength of the turbulence in these modes were observed both in the intensity and phase transverse profile, noticing the movement, but not the loss of the phase indeterminations of the beams. The properties of the order, degree and ellipticity parameters were studied as well, concluding that the performance of these vortex beams while carrying and maintaining information is more influenced by the order p and degree m of the modes, than by the chosen ellipticity ε of the mode, that had no practical impact in the overlap of a mode. This means that the chose of basis in which a mode with given order and degree is propagated has no effect on its robustness to keep information in the initial mode.

As general rules, the effects on the robustness of the beam lay instead in the chose of p, the difference $p - m$ and the value of m in that order. As a matter of fact, a similar work to the done in this thesis was recently published by Gu et al [57]. In this work, simulation of Helical Ince-Gauss beams was done, paying special analysis on the robustness of the modes as information carriers according to the ellipticity parameter, finally concluding that this parameter plays a big role on the performance of the modes, as well as the degree m parameter. Also, another study by Zhu et al was done [58] in which the robustness of entangled modes in turbulent atmosphere can be modified by the ε parameter. Comparing their results to the ones presented in this work, considering both the simulation and methods used, there was a good agreement on the obtained values. However, there was not such agreement on the interpretation of the results. While for them the effect of ellipticity can be considered significant, for us it is in fact practically negligible compared to the choose of order p, based on the overlap values presented in the several Tables. As such, we have demonstrated that the actual choose of modes rather than the basis in which they are described affects more heavily the performance of these modes of light as information carriers.

As an extension of these results, performance of polarized helical beams propagating through turbulent atmosphere can be studied using simulations as well, hoping that an additional degree of freedom of the propagated beams could provide other means to optimize the robustness of the modes. Another interesting thing to study more deeply could be the dynamics of the phase vortexes for helical beams: how their distribution changes with atmospheric effects and how this distribution change modifies the orbital angular momentum and information carrying efficiency of the modes. However, the most important steps to take would be to design and perform experiments in free space communication systems to test the simulations results and check the feasibility to use these modes to carry information in free space.

Appendix A

Code for decomposition of Ince-Gauss modes into the Laguerre-Gauss basis

Here I present the MATLAB code used for the decomposition of IG, necessary for the generation of IG intensity profiles for the simulations of atmospheric propagation and the respective phase profiles used in the generation of said modes Spatial Light Modulator phase patterns. As mentioned before, the original algorithm for this code was done by Dr. William Plick and based on the work by Bandres et. al. [29]. The version here presented is a translation of said algorithm to *MATLAB*.

```
% Credit to Dr. William Plick (University of Dayton) for original Mathematica code, translation
% and adjustments by Emmanuel Narvez.
% For more information: Miguel A. Bandres and Julio C. Gutirrez-Vega, "Ince Gaussian
% modes of the paraxial wave equation and stable resonators," J. Opt. Soc.
% Am. A 21, 873-880 (2004)

%Calculation of the p,m Ince-Gauss modes in the even (LGE) and odd (LGO) Laguerre-Gauss basis

%Choice of p, m, elipticity "e" and helicity "h" and get the parity of p and m on "ParP"
%and %ParM
%enter choice of m, must be same parity and less than or equal to p,
%equal to or greater than zero if p is odd, greater or equal to 1 if p
%is even functions
%The output gives two matrixes, each row of said matrixes has three
%elements, the first is the coefficient of the LG mode, the second the "n"
%value and the third the "l" value

function [LGE, LGO] = IGLG(p,m,h,e)
```

```
ParP = mod(p,2);
ParM = mod(m,2);

%Calculation of the even (Cosine based) LG modes
% We define the expansion of the IG polynomial and dimensionality of the representative matrix

if ParP == 0
    A = zeros(1,(p/2)+1);
    mxE = (m/2)+1;
    MdimE = (p/2)+1;
    MEe = zeros((p/2)+1, (p/2)+1);

    MEe(1,1) = 0;
    MEe(1,2) = e*((p/2)+1);

if MdimE > 2
    MEe(2,1) = e*p;
    MEe(2,2) = 4;
    MEe(2,3) = e*((p/2)+2);
end

if MdimE > 3
        r = 3;
        while r <= MdimE-1
            MEe(r,r-1) = ((p/2)-(r-2))*e;
            MEe(r,r) = 4*(((r-2)+1)^2);
            MEe(r,r+1) = ((p/2)+(r-2)+2)*e;
            r = r+1;
        end
end

if MdimE > 2
    MEe(MdimE, MdimE-1)= e;
    MEe(MdimE,MdimE)= 4*(((p/2))^2);
end

if MdimE == 2
            MEe(MdimE,MdimE-1)=2*e;
            MEe(MdimE, MdimE)= 4;
end

else
    A = zeros(1,((p-1)/2)+1);
    mxE = ((m-1)/2)+1;
    MdimE = ((p-1)/2)+1;
```

```
    MEe = zeros(((p-1)/2)+1, ((p-1)/2)+1);

    MEe(1,1) = ((e/2)*(p+1))+1;
    MEe(1,2) = (e/2)*(p+3);

    if MdimE > 2
        r = 1;
        while r <= MdimE-2
            MEe(r+1,r) = -(e/2)*((2*r)-p-1);
            MEe(r+1,r+1) = ((2*r)+1)^2;
            MEe(r+1,r+2) = (e/2)*(p+(2*r)+3);
            r = r+1;
        end
    end

    if MdimE > 1
        MEe(MdimE,MdimE-1) = e;
        MEe(MdimE,MdimE) = p^2;
     else
        MEe = zeros(((p-1)/2)+1, ((p-1)/2)+1);
        MEe(MdimE,MdimE) = p^2;
     end
end

%The size of A is the number of Cosine harmonic terms. If the size of A is 3,
%the terms would be A[1] + A[2] Cos[2 \[Eta]] + A[3] Cos[4 \[Eta]]

%Eigenvalues and Eigenvectors of the representative matrix, giving the las
%element of the Eigenvector value of 1

if p > 0
[VEigen,DEigen] = eig(MEe);
[DEigenOr,EOrd] = sort(diag(DEigen));
VEigen = VEigen(:,EOrd);
EigenV= zeros(MdimE,MdimE);

for i = 1:MdimE
    for j = 1:MdimE
        EigenV(j,i) = VEigen(j,i)/VEigen(MdimE,i);
    end
end

%Choice of the correct eigenvector
EigenV;
NC=size(A);
NC(2);
```

```
for h = 1:NC(2);
    A(1,h)=EigenV(h,mxE);
end

A;

%Calculate which laguerre-gauss even modes (LG[n,l]) will be needed to expand
%the Ince-gauss mode (need to have same Gouy phase).
modesE=0;
countE=0;
ModesE = zeros(10,3);
if ParP==0
    for l = 0:p
        l;
        for n = 0:p/2
            n;
            b = (2*n)+l;
            if b == p
                countE = countE+1;
                ModesE(countE,1)= countE;
                ModesE(countE,2)= n;
                ModesE(countE,3)= l;
            end
        end
    end
else
    for l = 1:p
        l;
        for n = 0:(p/2)+1
            n;
            b = (2*n)+l;
            if b == p
                countE = countE+1;
                ModesE(countE,1)= countE;
                ModesE(countE,2)= n;
                ModesE(countE,3)= l;
            end
        end
    end
end

countE;
ModesE;
ModE = zeros(countE,2);
```

```
%Fill the used modes
for k = 1:countE
    ModE(k,1) = ModesE(k,2);
    ModE(k,2) = ModesE(k,3);
end


%First column are n, second are l
ModE;
coefE = zeros(1,countE);

%Coefficients of each even LGE mode
for u = 1:countE
         coefE(u) = ((-1)^(ModE(u,1)+ModE(u,2)+((p+m)/2)))*sqrt((1+KDelta(ModE(u,2),0))*
         factorial(ModE(u,1))*factorial(ModE(u,1)+ModE(u,2)))*A(u);
end

coefE;
NcofE=coefE/(norm(coefE));


%Calculation of the odd (Sine based) LG modes
% We define the expansion of the IG polynomial and dimensionality of the representative matrix
if ParP == 0
    B = zeros(1,(p/2));
    mxO = (m/2);
    MdimO = (p/2);
    MOe = zeros((p/2), (p/2));

MOe(1,1) = 4;
MOe(1,2) = e*((p/2)+2);

if MdimO > 2
    r = 1;
    while  r <= (MdimO-2)
    MOe(r+1,r) = e*((p/2)-(r));
    MOe(r+1,r+1) = 4*((r+1)^2);
    MOe(r+1,r+2) = e*((p/2)+2+r);
    r=r+1;
    end
end

    if MdimO > 1
        MOe(MdimO,MdimO-1)=e;
        MOe(MdimO,MdimO)=4*((p/2)^2);
    else
```

```
        MOe = zeros((p/2), (p/2));
        MOe(MdimO,MdimO)=4*((p/2)^2);
    end

else
    B = zeros(1,(p+1)/2);
    mxO = ((m-1)/2)+1;
    MdimO = ((p-1)/2)+1;
    MOe = zeros(((p-1)/2)+1, ((p-1)/2)+1);

    MOe(1,1) = 1-((e/2)*(p+1));
    MOe(1,2) = (e/2)*(p+3);

    if MdimO > 2
        r = 1;
        while r <= MdimO-2
            MOe(r+1,r) = -(e/2)*((2*r)-p-1);
            MOe(r+1,r+1) = ((2*r)+1)^2;
            MOe(r+1,r+2) = (e/2)*(p+(2*r)+3);
            r = r+1;
        end
    end

     if MdimO > 1
        MOe(MdimO,MdimO-1) = e;
        MOe(MdimO,MdimO) = p^2;
     else
        MOe = zeros(((p-1)/2)+1, ((p-1)/2)+1);
        MOe(MdimO,MdimO) = p^2;
     end
end

MOe;

%The size of B is the number of Sine harmonic terms. If the size of A is 3,
%the terms would be A[1] + A[2] Sin[2 \[Eta]] + A[3] Sin[4 \[Eta]]

%Eigenvalues and Eigenvectors of the representative matrix, giving the last
%element of the Eigenvector value of 1

[VEigenO,DEigenO] = eig(MOe);
[DEigenOO,OOrd] = sort(diag(DEigenO));
VEigenO = VEigenO(:,OOrd);
EigenVO= zeros(MdimO,MdimO);

%Getting the same as mathematica (last element of Eigenvector = 1)
```

```
for i = 1:MdimO
    for j = 1:MdimO
        EigenVO(j,i) = VEigenO(j,i)/VEigenO(MdimO,i);
    end
end

EigenVO;
NCO=size(B);
NCO(2);

for h = 1:NCO(2)
    %Case m = 0
    if mxO == 0
    B(1,h)=EigenVO(h,1);
    else
    B(1,h)=EigenVO(h,mxO);
    end
end

B;

%Calculate which laguerre-gauss even modes (LG[n,l]) will be needed to expand
%the Ince-gauss mode
modesO=0;
countO=0;
ModesO = zeros(10,3);
if ParP==0
    for l = 1:p
        l;
        for n = 0:p/2
            n;
            b = (2*n)+l;
            if b == p
                countO = countO+1;
                ModesO(countO,1)= countO;
                ModesO(countO,2)= n;
                ModesO(countO,3)= l;
            end
        end
    end
else
    for l = 1:p
        l;
        for n = 0:((p-1)/2)
            n;
            b = (2*n)+l;
```

```
            if b == p
                countO = countO+1;
                ModesO(countO,1)= countO;
                ModesO(countO,2)= n;
                ModesO(countO,3)= l;
            end
        end
    end
end

ModO = zeros(countO,2);
countO;
ModesO;

%Fill the used modes
for k = 1:countO
    ModO(k,1) = ModesO(k,2);
    ModO(k,2) = ModesO(k,3);
end


%First column are n, second are l
ModO;

%Coefficients of each odd LGO mode
coefO = zeros(1,countO);
for u = 1:countO
    %Case m = 0
         if mxO == 0
             coefO(u) = 0;
         else
            coefO(u) = ((-1)^(ModO(u,1)+ModO(u,2)+((p+m)/2)))*sqrt((1+KDelta(ModO(u,2),0))*
            factorial(ModO(u,1))*factorial(ModO(u,1)+ModO(u,2)))*B(u);
         end
end

coefO;
NcofO=coefO/(norm(coefO));

LGE = zeros(countE,3);
LGO = zeros(countO,3);

for u=1:countE
    LGE(u,2) = ModE(u,1);
    LGE(u,3) = ModE(u,2);
    LGE(u,1) = NcofE(u);
```

```
end

for u=1:countO
    LGO(u,2) = ModO(u,1);
    LGO(u,3) = ModO(u,2);
    LGO(u,1) = NcofO(u);
end
else
      LGE = zeros(1,3);
   LGO = zeros(1,3);
    LGE(1,2) = 0;
    LGE(1,3) = 0;
    LGE(1,1) = 1;
    LGO(1,2) = 0;
    LGO(1,3) = 0;
    LGO(1,1) = 1;
end
end
```

Appendix B

Codes used for propagation of Helical Beams through atmospheric turbulence

In this appendix the codes used for the simulation of propagation of different scalar vortex beams are presented, the first of these covers the propagation of any electrical field using the properties of the transfer function of the air. The second, shows the construction of the random phase screens used to simulate turbulence in the atmosphere. The last code shows the complete propagation simulation of Helical beams through the atmosphere, in particular, the code used for the comparison of different ellipticities of a same beam is shown, but all the codes used for different propagation parameters show the same structure. As mentioned in the main text, the core of the algorithms is attributed to Qiwen Zhan of UD and Carlos Sevilla Gutierrez, graduate of UD and CIO. However, very significant changes to said algorithms were made.

B.1 Code for the propagation of a beam through a medium using the transfer function

```
 %scalar2d(in,N,d,Lembda,n,lembda) is 2D scalar diffraction propagation
% in is the starting field
% N is sampling points
% d is propagation distance
% Lembda is spatial dimension in x and y direction
% n is index of refraction
```

```
% lembda is wavelength
% out is the result of the propagation

function out=scalar2d(in,N,d,Lembda,n,lembda)

k=2*pi*n/lembda;
% Generate x and y coordinates
Deltax=Lembda/N;
Deltay=Lembda/N;

Nmid=N/2;
for i=1:N
   x(i)=(i-Nmid-1)*Deltax;
   y(i)=(i-Nmid-1)*Deltay;
end

[x,y]=meshgrid(fftshift(x),fftshift(y));

% Generate k-space
Deltakx=2*pi/Lembda;
Deltaky=2*pi/Lembda;
for i=1:N
   kx(i)=(i-Nmid-1)*Deltakx;
   ky(i)=(i-Nmid-1)*Deltaky;
end
[kx,ky]=meshgrid(fftshift(kx),fftshift(ky));
kz=sqrt(k^2-kx.^2-ky.^2);
%kz=-(kx.^2+ky.^2)/2/k; % Fresnel propagator
% Calculate the angular spectrum of input
spectrum=fft2(in);
% Multiply transfer function, this transfer function only
% subject to scalar theory
temp=exp(j*d*kz).*spectrum;
% Claculate the resulted field
out=fftshift(ifft2(temp));
```

B.2 Code for the creation of random turbulence phase mask

```
%Propagation of  Scalar Vortex Beams

function [E,x,y]=scalarprop1(Lambda,L,Z,N,Cn2,E0)

%RETURN TO l0 = 10*10^3 and L0=3*10^6
%b=zeros(1,10);
```

```
w0=70*10^3;
l0=10*10^3;
L0=3*10^6;

% Grid in space
Deltax=L/N;
Deltay=L/N;
Nmid=N/2;
for i=1:N
   x(i)=(i-Nmid-1)*Deltax;
   y(i)=(i-Nmid-1)*Deltay;
end


[x,y]=meshgrid(x,y);


% Generate k spcae coordinator
Deltakx=2*pi/L;
Deltaky=2*pi/L;
for i=1:N
   kx(i)=(i-Nmid-1)*Deltakx;
   ky(i)=(i-Nmid-1)*Deltaky;
end
[kx,ky]=meshgrid(fftshift(kx),fftshift(ky));

k=sqrt(kx.^2+ky.^2);

% Set up the parameters for propagation

% Set up the random phase screens
% Use randn() to generate independent N(0,1) noises
% Use Kolmogorov power spectrum law 0.033*Cn2*k^-11/3
% Cn2 is the index structure constant
% For weak turnbulence Cn2~10^-17 m^-2/3 or less
% For strong turbulence Cn2~10^-13^-2/3 or more
% The phase spectrum is related to the index spectrum through
% psdofphase(k)=2*pi*k^2*Z*psdofindex, where Z is the distance propagated

%for p=1:50

% start randn with different initial state everytime


randn('state',sum(100*clock));
A=randn(size(E0));
```

```
randn('state',sum(100*clock));
B=randn(size(E0));

% Index power spectral density

%kolmogorov model
%indexpsd=0.033*Cn2*k.^(-11/3);


%Karman model

indexpsd=0.033*Cn2*exp(-(k.*l0/5.92).^2).*(k.^2+(2*pi/L0).^2).^(-11/6);

% Phase power spectral density
phasepsd=2*pi*(2*pi/Lambda)^2*Z*indexpsd;

% Random phase screen (this results two random screens)
% (N*Deltakx)^2 factor is for the normalization of inverse FFT
phi=ifft2(sqrt(phasepsd).*(A+j*B)/Deltakx)*(N*Deltakx)^2;

phi1=real(phi);
phi2=imag(phi);

% Phase screen due to turbulence, this random phase will be multipled to
% the field E for further propagation
phasescreen=exp(j*phi1);

max(max(x));
mask=zeros(size(x));
mask(find(sqrt(x.^2+y.^2)<=1.5*10^6))=1;

% Linear propagation of each orthogonal field component
E=scalar2d(fftshift(E0.*phasescreen),N,Z,L,1,Lambda);
```

B.3 Code for the simulation of propagation of helical beams

```
% This script investigates the Scalar Vortex Propagation of Ince-Gaussian
% profile beams through turbulent atmosphere

%Units are microns
clear all; clc; close all

Lambda=0.6328;%1.55;
hw=0;
```

```
% Set up the coordinates, number of pixels and size in microns of windows
% and each pixel
N=1024;
L=5*10^5;
pixs = L/N;
pixa = pixs^2;

% For IG parameters (pp "radial", m "azimuthal", e "ellipticity")
pp = 8;
m = 2;
e = 0.00001;

%Beam waist
w0 = 10000;
rang1 = ceil(w0/pixs);
z0=pi*(w0*10^-6)^2/(Lambda*10^-6);

%Total distance (2000*10^6)
ZT = 2000*10^6;
%Divide the distance by
dparts = 20;
%Number of random phase screens per each division
nscre = 5;
%Number of times to propagate
npro = 200;

% Strength of turbulence (-16 weak, -15 normal, -14 strong), according to
% von Karman model
Cn2=10^-15*10^-4;

%For several ellipticities
nue = 6;
%Cell of 5 because we need distance, value of overlap, value of
%scintillation name and Strehl Ratio
elli = cell(5,nue);
dv = zeros(dparts+1,1);
for tt = 1:(dparts+1)
    dv(tt) = (tt-1)*(ZT/dparts)*10^-6;
end

for tt = 1:nue
    elli{1,tt} = dv;
    elli{2,tt} = zeros(dparts+1,1);
    elli{3,tt} = zeros(dparts+1,1);
    name = sprintf('e= %1.1d', (tt-1)*2);
```

```
    elli{4,tt} = name;

    if tt==nue
        name = sprintf('e= INF');
        elli{4,tt} = name;
    end
    elli{5,tt} = zeros(dparts+1,1);
end

%Total number of iterations
Ni = nue*(dparts+1)*npro;

%Decomposition of IG modes into LG modes, more information in the function
%file, IGe has even LG components, IGo the odd.
%First column is weight, second is radial mode and third is azimuthal mode
[IGe,IGo] = IGtoLG2(pp,m,1,e)

%Get the matrix with the Ince Gaussian modes, the order is the Even, Odd,
%Helical+ and Helical- modes, Expectation value of OAM and grid in x,y.
%As input, one uses the 3 column matrix of LG modes with weight,
%wavelenght, number of pixels of window, physical size of window, beam
%waist and degree m of IG mode.
[EMODES,OMODES,EIG,EIG2,OAM,x,y] = IGgrid(IGe,IGo,Lambda,N,L,w0,m);

% %Initial Intensity and phase, if not wanting to see, put inside figure ""Visible", false"
% figure("Visible", false)
% surfc(x,y,abs(EIG).^2);
% colormap hot;
% shading interp
% h = colorbar;
% ylabel(h, 'Intensity')
% xlabel('X direction (um)');
% ylabel('Y direction (um)');
% axis equal
% view(0,90)
% title(sprintf('IG p=%1d, m=%1d, e=%1d \nnot propagated',pp,m,e))
% print(sprintf('0IG p=%1d, m=%1d, e=%1d not propagated.jpg',pp,m,e),'-djpeg');

%Initiation for parameters
E2 = EIG;
%Z=(ZT/dparts);
Z = 0;

% 3 for just scintillation and overlap, add 1 to add strehl ratio and 3 for
% variance of each quantity.
tab = zeros(dparts+1,7);
```

```
E0 = E2;
TD = 0;
int = 0;



% Propagation distance; Here we can change the distance to get the
% interference pattern
for t = 1: nue
    %Decomposition of IG modes into LG modes, more information in the function
    %file, IGe has even LG components, IGo the odd.
    %First column is weight, second is radial mode and third is azimuthal mode
    [IGe,IGo] = IGtoLG2(pp,m,1,e)

    %Get the matrix with the Ince Gaussian modes, the order is the Even, Odd,
    %Helical+ and Helical- modes, Expectation value of OAM and grid in x,y.
    %As input, one uses the 3 column matrix of LG modes with weight,
    %wavelenght, number of pixels of window, physical size of window, beam
    %waist and degree m of IG mode.
    [EMODES,OMODES,EIG,EIG2,OAM,x,y] = IGgrid(IGe,IGo,Lambda,N,L,w0,m);

    E2 = EIG;
    %Z=(ZT/dparts);
    Z = 0;
    tab = zeros(dparts+1,3);
    E0 = E2;
    TD = 0;

    %Initialize file to get data report in txt
    cc = char(datetime('today'))
    filename = sprintf('Report IG %d_%d_e=%d,Cn2 = %d, Distance = %d, nscre = %d, number
    prop = %d %s.txt', pp, m, e, Cn2*10^4, ZT*10^-6, nscre, npro,  cc)
    save(filename);
    tab = zeros(dparts+1,7);

    %Initialize arrays of each value to measure

    ovv = zeros(npro,1);
    siv = zeros(npro,1);
    srv = zeros(npro,1);

    %For each number of propagation
    for u = 1:npro
        %For each distance
        for q=1:dparts+1 %100
```

```
    if mod(q,1) == 0
        int = int+1;
        % Display the progression of simulation
        display('**********************************************')
        display('In progress:')
        display(sprintf('Distance No. = %2d of %2d, Number of run = %2d of %2d,
        Ellip = %2d',q,dparts+1, u,npro, e));
        display(sprintf('Iteration No. %2d of %2d', int, Ni))
    end

%Reset or not reset the original profile
 %E0=E2;

 %Here I temporary divide propagation distance into nscre parts, each with
 %random turbulence.

     M=(ZT/dparts)/nscre;
     if q == 1
         M = 0;
     end
         for p=1:nscre
              [Ep,x,y]=scalarprop1(Lambda,L,M,N,Cn2,E0);
              TD = TD+M;
              wzzz=sqrt(w0^2*(1+(TD*Lambda/pi/(w0^2))^2));
              E0=Ep;
         end

     %calculate beam waist after Z distance propagation
     wz=sqrt(w0^2*(1+(Z*Lambda/pi/(w0^2))^2));

     %Profile propagated without turbulence
     Z
     ENT =fftshift(scalar2d(EIG,N,Z,L,1,Lambda));

     %Calculate where to analize scintillation(square of 2wz size)
     %or actual size of the beam
     aENT = ENT.*conj(ENT);
     norm = max(aENT(:));
     fil= aENT((N+2)/2,:);
     col = aENT(:,(N+2)/2);

     for j = 1:N
         if fil(j)>(((1/exp(1))^2)-.08)*norm
             if fil(j)<((1/exp(1))^2)*norm
                 xcor = j;
                 break
```

```
            end
        end
    end

    for j = 1:N
        if col(j)>(((1/exp(1))^2)-.08)*norm
            if col(j)<((1/exp(1))^2)*norm
                ycor = j;
                break
            end
        end
    end

    %rang = ceil(wz/pixs);

    rangx = N/2-xcor;
    rangy = N/2-ycor;

%   reg = Ep((N/2)-rang:(N/2)+rang,(N/2)-rang:(N/2)+rang);
%   regENT = EIG((N/2)-rang:(N/2)+rang,(N/2)-rang:(N/2)+rang);

    reg = Ep((N/2)-rangy:(N/2)+rangy,(N/2)-rangx:(N/2)+rangx);
    regENT = ENT((N/2)-rangy:(N/2)+rangy,(N/2)-rangx:(N/2)+rangx);

    %Scintillation index with and without region
    SII = mean(mean(abs(reg).^4))/(mean(mean(abs(reg).^2)))^2-1;
    %SI=mean(mean(abs(Ep).^4))/(mean(mean(abs(Ep).^2)))^2-1;

    %Strehl ratio calculation IENT is intensity without turbulence
    %IEP with turbulence

    IENT = 0;
    for pixelx = 1:(2*rangy+1)
        for pixely = 1:(2*rangx+1)
            Vpixel = regENT(pixelx,pixely)*conj(regENT(pixelx,pixely));
            IENT = IENT + Vpixel;
        end
    end

    IEP = 0;
    for pixelx = 1:(2*rangy+1)
        for pixely = 1:(2*rangx+1)
            Vpixel = reg(pixelx,pixely)*conj(reg(pixelx,pixely));
            IEP = IEP + Vpixel;
        end
    end
```

```
            SRV = abs(IEP/IENT);

            %Overlap integrals without and with turbulence
            SumintNP = 0;
            for pixelx = 1:N
                for pixely = 1:N
                    Vpixel = ENT(pixelx,pixely)*conj(ENT(pixelx,pixely))*pixa;
                    SumintNP = SumintNP + Vpixel;
                end
            end

            SumintP = 0;
            for pixelx = 1:N
                for pixely = 1:N
                    Vpixel = ENT(pixelx,pixely)*conj(Ep(pixelx,pixely))*pixa;
                    SumintP = SumintP + Vpixel;
                end
            end

            %Overlap and scintillation value and fill of the columns
            MV = abs(SumintP/SumintNP);
            SII;
            tab(q,2) = tab(q,2)+MV;
            tab(q,3) = tab(q,3)+SII;
            tab(q,4) = tab(q,4)+SRV;
            ovv(u,1) = MV;
            siv(u,1) = SII;
            srv(u,1) = SRV;

        if u == npro;
%           Fill the columns
            tab(q,1) = Z*10^-6;
            tab(q,2) = tab(q,2)/npro;
            tab(q,3) = tab(q,3)/npro;
            tab(q,4) = tab(q,4)/npro;
            tab(q,5) = std(ovv);
            tab(q,6) = std(siv);
            tab(q,7) = std(srv);

            % See the transverse fields and phases, ENT is without
            % turbulence, Ep with turbulence

            aEp = Ep.*conj(Ep);
            aEp = abs(aEp);
            normE = max(aEp(:));
            figure("Visible", false)
```

```
            surfc(x,y,aEp/norm);
            colormap hot;
            shading interp
            h = colorbar;
            ylabel(h, 'Intensity')
            xlabel('X direction (um)');
            ylabel('Y direction (um)');
            axis equal
            view(0,90)
            title(sprintf('IG p=%1d, m=%1d, e=%1d Vortex propagated Z= %2d m\nC_n^2= %2d, OV=%d '
            ,pp,m,e,Z*10^-6,Cn2*10^4, tab(q,2)))
            print(sprintf('IG p=%1d, m=%1d, e=%1d Vortex propagated Z= %2d m,C_n^2= %2d, OV=%d.jpg'
            ,pp,m,e,Z*10^-6,Cn2*10^4, tab(q,2)),'-djpeg');

            figure("Visible", false)
            surfc(x,y,angle(Ep));
            colormap hot;
            shading interp
            h = colorbar;
            ylabel(h, 'Phase')
            xlabel('X direction (um)');
            ylabel('Y direction (um)');
            axis equal
            view(0,90)
            title(sprintf('Phase IG p=%1d, m=%1d, e=%1d Vortex propagated Z= %2d m\nC_n^2= %2d,
            IV=%d ',pp,m,e,Z*10^-6,Cn2*10^4, tab(q,2)))
            print(sprintf('Phase IG p=%1d, m=%1d, e=%1d Vortex propagated Z= %2d m,C_n^2= %2d,
            IV=%d.jpg',pp,m,e,Z*10^-6,Cn2*10^4, tab(q,2)),'-djpeg');
         end

         Z=Z+(ZT/dparts);

        end
%Reset to the original distance
%Z=(ZT/dparts)
    Z = 0;
    E0 = E2;
    end

    %Fill report file
fid = fopen(filename, 'w');
    fprintf(fid, "Propagation of scalar Ince-Gaussian mode, p = %d, m=%1d, e=%1d Z= %1dm.
    \nNumber of propagations=%1d\n", pp,m,e,ZT*10^-6, npro)
    fprintf(fid, "Number of screens: %1d, Wavelength = %1d nm, Initial Beam waist = %1d m,
    Turbulence = %1d\n", nscre, Lambda*1000, w0*10^-6, Cn2*10^4)
    fprintf(fid, "Distance (m)\tOverlap (mean)\tSDev OV\tScintillation (mean)\tSDev SciInd
```

```
    \tStrehl Ratio (mean)\tSDev SthRat\r");
    for i = 1:dparts+1
        fprintf(fid,'%8.4f\t%8.4f\t%8.4f\t%8.4f\t%8.4f\t%8.4f\t%8.4f\r',tab(i,1), tab(i,2)
        , tab(i,5), tab(i,3), tab(i,6), tab(i,4), tab(i,7));
    end
fclose(fid);

elli{2,t} = tab(:,2);
elli{3,t} = tab(:,3);
elli{5,t} = tab(:,4);

if t==1
  e = e-e;
end

e = e+2;

%Final ellipticity is "infinite"
if t==nue-1
    e = 1000000;
end
end

%Comparison graphing
figure()
for i=1:nue
     plot(elli{1,i}, elli{2,i},'LineWidth',1)
     if i == nue
         title(sprintf('Overlap value as function of distance for different ellipticities
         \n p=%1d
         , m=%1d, C_n^2= %2d',pp,m,Cn2*10^4));
         xlabel('Distance [m]');
         ylabel('Overlap integral value');
         ylim([0 1]);
         legend(elli(4,:),'Location','southwest');
     end
    hold on
    if i == nue
        print(sprintf('Overlap value as function of distance for different ellipticities
        p=%1d
        , m=%1d, C_n^2=%2d.jpg',pp,m,Cn2*10^4),'-djpeg')
    end
end

figure()
for i=1:nue
```

```
     plot(elli{1,i}, elli{3,i},'LineWidth',1)
     if i == nue
         title(sprintf('Scintillation index as function of distance for different ellipticities
         \n p=%1d, m=%1d, C_n^2= %2d',pp,m,Cn2*10^4));
         xlabel('Distance [m]');
         ylabel('Scintillation Index');
         legend(elli(4,:),'Location','northwest');
     end
    hold on
    if i == nue
        print(sprintf('Scintillation index as function of distance for different ellipticities
        p=%1d, m=%1d, C_n^2= %2d.jpg',pp,m,Cn2*10^4),'-djpeg');
    end
end

figure()
for i=1:nue
     plot(elli{1,i}, elli{5,i},'LineWidth',1)
     if i == nue
         title(sprintf('Strehl Ratio as function of distance for different ellipticities
         \n p=%1d, m=%1d, C_n^2= %2d',pp,m,Cn2*10^4));
         xlabel('Distance [m]');
         ylabel('Strehl Ratio');
         ylim([0.8 1]);
         legend(elli(4,:),'Location','southwest');
     end
    hold on
    if i == nue
        print(sprintf('Strehl Ratio as function of distance for different ellipticities
        p=%1d, m=%1d, C_n^2= %2d.jpg',pp,m,Cn2*10^4),'-djpeg');
    end
end
```

Bibliography

[1] M. P. Lavery, "Tackling africa's digital divide," *Nature Photonics*, vol. 12, no. 5, pp. 249–252, 2018.

[2] K. Anbarasi, C. Hemanth, and R. Sangeetha, "A review on channel models in free space optical communication systems," *Optics Laser Technology*, vol. 97, pp. 161 – 171, 2017.

[3] A. Trichili, A. B. Salem, A. Dudley, M. Zghal, and A. Forbes, "Encoding information using laguerre gaussian modes over free space turbulence media," *Opt. Lett.*, vol. 41, pp. 3086–3089, Jul 2016.

[4] Z. Guan and M. Zhao., "Demonstration of a free-space optical communication system using a solar-pumped laser as signal transmitter," *Laser Phys. Lett.*, vol. 12, Mar 2017.

[5] X. Z. Zen Cao and G. Osnabrugge, "Reconfigurable beam system for non-line-of-sight free-space optical communication," *Light Sci Appl*, vol. 12, Jul 2019.

[6] G. Gibson, J. Courtial, M. J. Padgett, M. Vasnetsov, V. Pas'ko, S. M. Barnett, and S. Franke-Arnold, "Free-space information transfer using light beams carrying orbital angular momentum," *Opt. Express*, vol. 12, pp. 5448–5456, Nov 2004.

[7] B. Shumm, *Effect of Atmospheric Turbulence on Synthetic Aperture Ladar Imaging Performance*. PhD thesis.

[8] M. Queißer, M. Burton, and L. Fiorani, "Differential absorption lidar for volcanic co2 sensing tested in an unstable atmosphere," *Opt. Express*, vol. 23, pp. 6634–6644, Mar 2015.

[9] M. A. E. A. K. R. F. M. Katja Friedrich, Julie K. Lundquist, "Stability and turbulence in the atmospheric boundary layer: A comparison of remote sensing and tower observations," *Atmospheric Science*, Feb 2012.

[10] M. Loktev, O. Soloviev, S. Savenko, and G. Vdovin, "Speckle imaging through turbulent atmosphere based on adaptable pupil segmentation," *Opt. Lett.*, vol. 36, pp. 2656–2658, Jul 2011.

[11] G. L. . J. M. K. Ningbo Zhao, Xiaoying Li, "Demonstration of a free-space optical communication system using a solar-pumped laser as signal transmitter," *Nature Photonics*, vol. 9, p. pages822–826, Dec 2015.

[12] S. M. Zhao, J. Leach, L. Y. Gong, J. Ding, and B. Y. Zheng, "Aberration corrections for free-space optical communications in atmosphere turbulence using orbital angular momentum states," *Opt. Express*, vol. 20, pp. 452–461, Jan 2012.

[13] K. Dai, C. Gao, L. Zhong, Q. Na, and Q. Wang, "Measuring oam states of light beams with gradually-changing-period gratings," *Opt. Lett.*, vol. 40, pp. 562–565, Feb 2015.

[14] L. Allen, M. W. Beijersbergen, R. J. C. Spreeuw, and J. P. Woerdman, "Orbital angular momentum of light and the transformation of laguerre-gaussian laser modes," *Phys. Rev. A*, vol. 45, pp. 8185–8189, Jun 1992.

[15] A. E. Willner, H. Huang, Y. Yan, Y. Ren, N. Ahmed, G. Xie, C. Bao, L. Li, Y. Cao, Z. Zhao, J. Wang, M. P. J. Lavery, M. Tur, S. Ramachandran, A. F. Molisch, N. Ashrafi, and S. Ashrafi, "Optical communications using orbital angular momentum beams," *Adv. Opt. Photon.*, vol. 7, pp. 66–106, Mar 2015.

[16] R. G. . H. Haken, "Laserlight — first example of a second-order phase transition far away from thermal equilibrium," *Zeitschrift für Physik*, vol. 237, pp. 31—-46, 1970.

[17] K. O. Ma.R Dennis and M. Padgett, "Singular optics: optical vortices and polarization singularities," *Progress in Optics*, vol. 55, pp. 293–363, 2009.

[18] M. Padgett and R. Bowman, "Tweezers with a twist," *Nature Photonics*, vol. 5, pp. 343–348, 2011.

[19] W. Zhang, Z. Wu, J. Wang, and L. Chen, "Experimental demonstration of twisted light's diffraction theory based on digital spiral imaging," *Chin. Opt. Lett.*, vol. 14, p. 110501, Nov 2016.

[20] P. Tan, X.-C. Yuan, G. Yuan, and Q. Wang, "High-resolution wide-field standing-wave surface plasmon resonance fluorescence microscopy with optical vortices," *Applied Physics Letters*, vol. 97, pp. 241109–241109, 12 2010.

[21] Y. Zhao, A. Askarpour, L. Sun, J. Shi, X. Li, and A. Alù, "Chirality detection of enantiomers using twisted optical metamaterials," *Nature Communications*, vol. 8, p. 14180, 01 2017.

[22] G. Xie, H. Song, Z. Zhao, G. Milione, Y. Ren, C. Liu, R. Zhang, C. Bao, L. Li, Z. Wang, K. Pang, D. Starodubov, B. Lynn, M. Tur, and A. E. Willner, "Using a complex optical orbital-angular-momentum spectrum to measure object parameters," *Opt. Lett.*, vol. 42, pp. 4482–4485, Nov 2017.

[23] G. Foo, D. M. Palacios, and G. A. Swartzlander, "Optical vortex coronagraph," *Opt. Lett.*, vol. 30, pp. 3308–3310, Dec 2005.

[24] Y. Ren, L. Li, Z. Wang, S. M. Kamali, E. Arbabi, A. Arbabi, Z. Zhao, G. Xie, Y. Cao, N. Ahmed, Y. Yan, C. Liu, A. Willner, S. Ashrafi, M. Tur, A. Faraon, and A. Willner, "Orbital angular momentum-based space division multiplexing for high-capacity underwater optical communications," *Scientific Reports*, vol. 6, 04 2016.

[25] Z. Ibarra-Borja, C. Sevilla-Gutiérrez, R. Ramírez-Alarcón, Q. Zhan, H. Cruz-Ramírez, and A. B. U'Ren, "Direct observation of oam correlations from spatially entangled bi-photon states," *Opt. Express*, vol. 27, pp. 25228–25240, Sep 2019.

[26] M. Mafu, A. Dudley, S. Goyal, D. Giovannini, M. McLaren, M. J. Padgett, T. Konrad, F. Petruccione, N. Lütkenhaus, and A. Forbes, "Higher-dimensional orbital-angular-momentum-based quantum key distribution with mutually unbiased bases," *Phys. Rev. A*, vol. 88, p. 032305, Sep 2013.

[27] G. Vallone, V. D'Ambrosio, A. Sponselli, S. Slussarenko, L. Marrucci, F. Sciarrino, and P. Villoresi, "Free-space quantum key distribution by rotation-invariant twisted photons," *Phys. Rev. Lett.*, vol. 113, p. 060503, Aug 2014.

[28] G. Vallone, V. D'Ambrosio, A. Sponselli, S. Slussarenko, L. Marrucci, F. Sciarrino, and P. Villoresi, "Free-space quantum key distribution by rotation-invariant twisted photons," *Phys. Rev. Lett.*, vol. 113, p. 060503, Aug 2014.

[29] M. A. Bandres and J. C. Gutiérrez-Vega, "Ince–gaussian beams," *Opt. Lett.*, vol. 29, pp. 144–146, Jan 2004.

[30] D. J. Griffiths, *Introduction to electrodynamics; 4th ed.* Boston, MA: Pearson, 2013. Re-published by Cambridge University Press in 2017.

[31] O. Svelto, *Principles of Lasers*. Milano, Italy: Springer Science+Business Media, 2010.

[32] P. P. B. Ting-Chung Poon, *Contemporary Optical Image Processing with MATLAB*. Oxford, UK: Elsevier Inc., 2001.

[33] F. H. George Arfken, Hans Weber, *Mathematical Methods for Physicists: A comprehensive guide*. New Delhi, India: Elsevier Inc., 2018.

[34] E. L. Ince, "A linear differential equation with periodic coefficients," *Proceedings of the London Mathematical Society*, 1925.

[35] M. A. Bandres and J. C. Gutiérrez-Vega, "Ince–gaussian modes of the paraxial wave equation and stable resonators," *J. Opt. Soc. Am. A*, vol. 21, pp. 873–880, May 2004.

[36] W. Plick, M. Krenn, R. Fickler, S. Ramelow, and A. Zeilinger, "Quantum orbital angular momentum of elliptically-symmetric light," *Physical Review A*, vol. 87, 08 2012.

[37] A. T. ab Johannes Courtiala, "Mode transformations in terms of the constituent hermite–gaussian or laguerre–gaussian modes and the variable-phase mode converters," *Optics Communications*, vol. 181, pp. 35–45, Feb 2000.

[38] A. E. Siegman, *Lasers*. Mill Valley, Calif: University Science, 1986.

[39] J. D. Jackson, *Classical Electrodynamics*. 1975.

[40] Z. X. Ya Shen, Xi Wang, "Optical vortices 30 years on: Oam manipulation from topological charge to multiple singularities.," *Light Sci Appl*, vol. 8, Oct 2019.

[41] C. López-Mariscal and J. Gutierrez Vega, "Propagation dynamics of helical hermite-gaussian beams," pp. 666307–666307, 09 2007.

[42] G. F. Calvo, A. Picón, and E. Bagan, "Quantum field theory of photons with orbital angular momentum," *Phys. Rev. A*, vol. 73, p. 013805, Jan 2006.

[43] N. Bohr, "Über die serienspektra der elemente," *Z. Physik*, no. 2, p. 423–469, 1920.

[44] A. Mourka, M. Mazilu, C. Shanor, E. M. Wright, and K. Dholakia, "Characterizing the azimuthal and radial mode indices of a laguerre-gaussian beam using diffraction from a triangular aperture," in *Frontiers in Optics 2011/Laser Science XXVII*, p. LThF2, Optical Society of America, 2011.

[45] M. A. Cox, N. Mphuthi, I. Nape, N. Mashaba, L. Cheng, and A. Forbes, "Structured light in turbulence," *IEEE Journal of Selected Topics in Quantum Electronics*, vol. 27, p. 1–21, Mar 2021.

[46] C. A. S. Gutierrez, *Direct Observation of Conservation of OAM in Type-I Collinear SPDC*. University of Dayton - Centro de Investigaciones en Optica M.Sc. Thesis, 2018.

[47] A. Andrews, *Laser Beam Propagation through Random Media*. SPIE Press, 2005.

[48] L. Andrews, "An analytical model for the refractive index power spectrum and its application to optical scintillations in the atmosphere," *Journal of Modern Optics*, vol. 39, no. 9, pp. 1849–1853, 1992.

[49] V. I. Tatarskii, *Wave Propagation in a Turbulent Medium*. McGraw-Hill, 1961.

[50] G. GW, *Molecular Structure and the Properties of Liquid Crystals*. Academic Press, 1962.

[51] A. Forbes, A. Dudley, and M. McLaren, "Creation and detection of optical modes with spatial light modulators," *Adv. Opt. Photon.*, vol. 8, pp. 200–227, Jun 2016.

[52] W. Han, Y. Yang, W. Cheng, and Q. Zhan, "Vectorial optical field generator for the creation of arbitrarily complex fields," *Opt. Express*, vol. 21, pp. 20692–20706, Sep 2013.

[53] J. M. Martin and S. M. Flatté, "Simulation of point-source scintillation through three-dimensional random media," *J. Opt. Soc. Am. A*, vol. 7, pp. 838–847, May 1990.

[54] W. Cheng, J. W. Haus, and Q. Zhan, "Propagation of vector vortex beams through a turbulent atmosphere," *Opt. Express*, vol. 17, pp. 17829–17836, Sep 2009.

[55] M. P. J. Lavery, "Vortex instability in turbulent free-space propagation," *New Journal of Physics*, vol. 20, p. 043023, apr 2018.

[56] M. A. Cox, L. Maqondo, R. Kara, G. Milione, L. Cheng, and A. Forbes, "The resilience of hermite– and laguerre–gaussian modes in turbulence," *J. Lightwave Technol.*, vol. 37, pp. 3911–3917, Aug 2019.

[57] X. Gu, L. Chen, and M. Krenn, "Phenomenology of complex structured light in turbulent air," *Opt. Express*, vol. 28, pp. 11033–11050, Apr 2020.

[58] K. Zhu, Z. Lin, L. Yin, C. Wang, and G. Long, "Entanglement protection of ince-gauss modes in atmospheric turbulence using adaptive optics," *Opt. Express*, vol. 28, pp. 38366–38375, Dec 2020.